Liu et al. *Microsystems & Nanoengineering* (2026)12:108
https://doi.org/10.1038/s41378-026-01171-x

Microsystems & Nanoengineering
www.nature.com/micronano

REVIEW ARTICLE Open Access

A comprehensive review of hydrogen sensor for thermal runaway monitoring: fundamentals, recent advancements, and challenges

Lin Liu[1]✉, Chenfei Guo[1,2], Yingyi Wang[1], Kejie Guan[1,2], Sujie Qin[3], Xiaoshuang Gou[1], Fuqin Sun[1], Cheng Zhang[4], Weifan Zhou[1,2], Zhengyang Cai[5], Jun Xu[1], Fan Liu[1], Zihua Tian[1,2], Xiaowei Wang[1]✉ and Ting Zhang[1,2,6]✉

Abstract

Thermal runaway (TR) in lithium-ion batteries (LIBs) remains an intrinsic safety issue, posing significant risks of fire and explosion. Among various technologies employed to assess LIB status- including temperature, pressure, voltage, and gas measurements-gas sensors exhibit superior response speed and stronger sensing abilities. Notably, H_2 has been identified as the first gas released during the TR process when compared to other gases such as CO_2, CO and CH_4. Furthermore, H_2 serves as an indicator for the formation of trace Li dendrites, which are inducements of LIBs safety issues. Consequently, development of high performance H_2 sensors is essential for providing timely early safety warning. Compared with other types of H_2 sensors, chemiresistive H_2 sensors have garnered significant attention owing to their good sensitivity, low cost, and easy of miniaturization and integration into LIB cells. This review presents a comprehensive overview of chemiresistive H_2 sensors through classifying them into different categories based on sensing material systems. Within each category, the inherent fundamental sensing mechanisms and current strategies aimed at enhancing sensor performance have been systematically discussed. It is believed that chemiresistive H_2 sensors would play an important role in TR monitoring. Moreover, a more accuracy prediction could be implemented when H_2 sensors are integrated with other existing warning methods.

Introduction

Global environmental challenges and the rapid growth of portable electronics and electric vehicles have heightened the demand for cleaner, more efficient energy conversion technologies and high-density lithium-ion batteries (LIBs) with sustainable electrochemical performance. LIBs typically consist of cathode, anode, and electrolyte. To enhance the energy density of LIBs, researchers have made significant efforts to develop novel cathode and anode materials[1–3]. However, the LIBs with higher energy density may reduce thermal stability and cause safety problems, e.g., thermal runaway (TR). Owing to the irreversible increase of heat caused by TR, accidents relating to battery fire or even explosion still occur frequently[4–7]. During the past few years, lots of electric products were recalled ascribing to the unsafe batteries[8]. According to the existed data, more than half of the fires are caused by electric vehicle battery failure[9]. Therefore, development of advanced technologies for providing early warning of TR are essential to minimize the safety-related problems in practical LIB applications.

The TR is generally defined as the condition in which the rate of heat generation exceeds the rate of thermal dissipation, leading to a significantly increase in LIB temperature. A commonly accepted index for TR is when the rate of battery temperature rise surpasses 1 °C/s[10,11]. During the practical applications, LIBs may be subjected to various abuse conditions that can lead to TR, including

Correspondence: Lin Liu (liulin2013@sinano.ac.cn) or
Xiaowei Wang (xwwang2022@sinano.ac.cn) or
Ting Zhang (tzhang2009@sinano.ac.cn)
[1]i-lab, Suzhou Institute of Nano-Tech and Nano-Bionics (SINANO), Chinese Academy of Sciences (CAS), Suzhou, Jiangsu, PR China
[2]School of Nano-Tech and Nano-Bionics, University of Science and Technology of China, Hefei, Anhui, PR China
Full list of author information is available at the end of the article

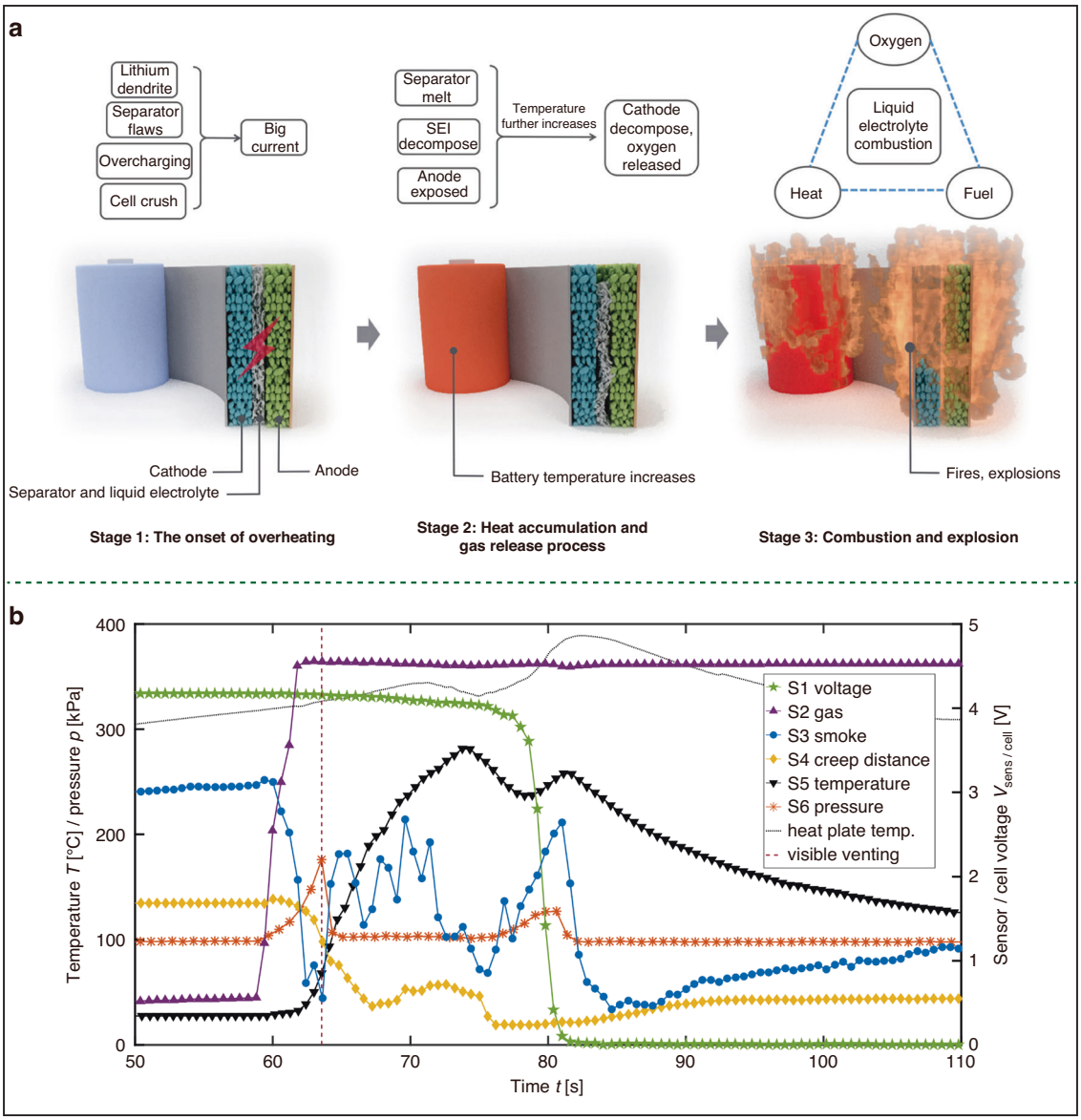

Fig. 1 The stages of TR process and the changes of relevant parameters during TR process. a Three stages for the TR process. Stage 1: The onset of overheating. The batteries change from a normal to an abnormal state, and the internal temperature starts to increase. Stage 2: Heat accumulation and gas release process. The internal temperature quickly rises, and the battery undergoes exothermal reactions. Stage 3: Combustion and explosion. The flammable electrolyte combusts, leading to fires and even explosions[496]. Copyright 2018, American Association for the Advancement of Science. **b** Readings of the seven sensors in thermal runaway test. The dashed line labeled with "visible venting" indicates the time when venting was visible outside of the battery housing. All sensors detect the thermal runaway effects of the cell within a time window of about 20 s[32]. Copyright 2018, Multidisciplinary Digital Publishing Institute

mechanical abuse (e.g., collision and crush), electrical abuse (e.g., external short circuit, overcharge, and over-discharge), and thermal abuse (e.g., overheating)[12,13]. Mechanical abuse may cause the deformation of LIBs, which can result in contact of cathode and anode and generate internal short circuit. Electrical abuse is usually caused by abnormal operation conditions, such as over-charge and overdischarge, leading to dendrite growth and internal short circuit. Thermal abuse will boost side reactions in the LIBs to generation of numerous heat and gases, such as decomposition of electrolyte. The TR process typically undergoes three stages as illustrated in Fig. 1a. At initial stage, the LIBs transition from a normal operational state to an abnormal one, such as over-charging, overheating, internal short circuits, etc., result-ing in an increase of LIB temperatures. During this stage, the self-heating rate remains relatively low (0.2 °C/min), and sometimes can be dissipated within the LIB packs.

While an increase in temperature may trigger sustained exothermic reactions that further elevate the temperature, the LIBs will go to stage 2. Once the stage 2 commences, the LIBs undergo a series of complex reactions, including the decomposition of solid electrolyte interphase (SEI) and cathode materials, as well as the melting of polymer separators. These reactions can accelerate the heat accumulation and gas release processes. At this stage, it is hardly to quench the TR process via any external cooling mechanism. The aforementioned exothermic reactions will lead to a dramatic increase in temperature, pressure, gas production, etc., and then the LIBs proceed to stage 3. As stage 3 starts, irreversible damage may occur within the LIBs, including risks of combustion and explosion. Furthermore, adjacent LIBs could be destroyed, potentially leading to a disaster.

Therefore, to ensure the safety of human life and personality, high-precision technologies are essential for providing an early warning of the TR in individual LIB cell. Such advancements could afford people a couple of few minutes to stay away from potential hazards. Currently, several safety warning systems for LIBs are available, primarily focusing on the detection of electrical, thermal, mechanical signals, and gas emissions. Although the end voltage of LIBs is a widely recognized electrical parameter for evaluating the TR, the process of voltage drop exhibits variability when encountered different TR trigger factors[14,15]. Moreover, an obvious change in voltage often occurs when the TR process evolves into an irretrievable state[16,17]. Thus, relying solely on battery voltage detection for early warning of TR is unreliable. In addition, temperature is a typical thermal indicator for judging whether TR has occurred within the LIBs. Currently, commonly used temperature sensors primarily monitor the surface temperature and usually fail to supply adequate and in-time information due to the significant disparity between the internal and external temperatures of LIBs[18,19]. Although there are several types of temperature sensors (e.g., thermocouples[20–22], and thermal resistance[23,24], optical fibers[18]) capable of detecting the internal temperatures, they often come with high costs and technical complexities[25–27]. Since TR-induced elevated temperatures and gas release can cause pouch cell swelling and deformation, detection of the mechanical signal such as pressure is more appropriate than temperature for serving as an early safety indicator[28,29]. However, the pressure sensors fail to trigger timely alerts under pressure abuse conditions[28]. Notably, during the stage 1, a large amount of gas is generated from electrochemical reactions inside the cell that allows gas sensors to be an alternative technology for early warning alert. Additionally, during the TR process, two distinct venting events can be observed, with the second event signifying battery failure. Consequently, the time gap between the two venting events provides a window for early warning[30]. Wenger et al.[31] carried out a series of overcharging experiments by varying the charge rate of current (e.g., 5A(1C), 30A(6C), and 60A (12C)) and found that the gas sensor detected the failure earlier than sensors based on temperature and voltage measurements. Koch et al.[32] selected a set of sensors to assess their capability for fast and reliable early warning by detecting various signals, including voltage, temperature, pressure, smoke, creep distance, force, and gas (as shown in Fig. 1b). Among these sensors, the SnO_2-based gas sensor, which is sensitive to CO and CH_2, provided the fastest detection speed and strongest sensing response[32]. Huang et al.[30] built a simulation model demonstrating that the gas sensor responds faster than the external temperature and pressure sensors. Consequently, gas sensors are capable of accurately monitoring released gases for practical early safety warnings.

The TR process of LIBs involves the decomposition of SEI and cathode materials, melting of polymer separators, and formation of Li dentaries. This process releases a lot of gases such as H_2, O_2, CO_2, CO, C_xH_x (CH_2, C_2H_4, etc.), HF and some organic vapor[33–35]. Golubkov et al.[36] investigated the components of venting gases in LIBs with different cathode materials, revealing that CO_2, CO and H_2 are three main gas components. Additionally, a small amount of HF can only be detected when the LIBs contain specific fluorine-containing materials[37]. To date, many researchers have analyzed the composition and released time of venting gases to identify typical gas indicator as early warning signs of TR through precise instruments such as differential electrochemical mass spectrometry[38], gas chromatograph (GC)[39], on-line electrochemical mass spectrometry (OMES)[40] and Raman[41,42]. Yang et al.[39] selected eight types of commercial $LiFePO_4$ LIBs to analyze the gas components using GC under overcharge abuse conditions. The results reveal that H_2 and CO_2 account for the highest proportions among five main gases, as shown in Fig. 2a. However, the accuracy of CO_2 detection in practical applications may be impacted by environmental factors. Thereby, Yang et al.[39] chose H_2, CO, and CH_2 as gas signals of overcharging to determine which one is the best for early warning, as shown in Fig. 2b, c. Obviously, H_2 was detected first, 204 s earlier than CO and 619s earlier than CH_2, and significantly earlier (579 s) than TR[39]. Zhang et al.[40] conducted operando OEMS characterizations under practical operation conditions, including overcharging, high temperature, and cycles of ageing/storage (Fig. 2d, e). Similarly, the release of H_2 is detected significantly earlier than that of CO_2 and CO under both normal charge and overcharge conditions at 25 °C (Fig. 2d). At high-temperature, the evolution of H_2 is much more distinguishable compared with CO and CO_2 under normal charge cycles and H_2 is the first

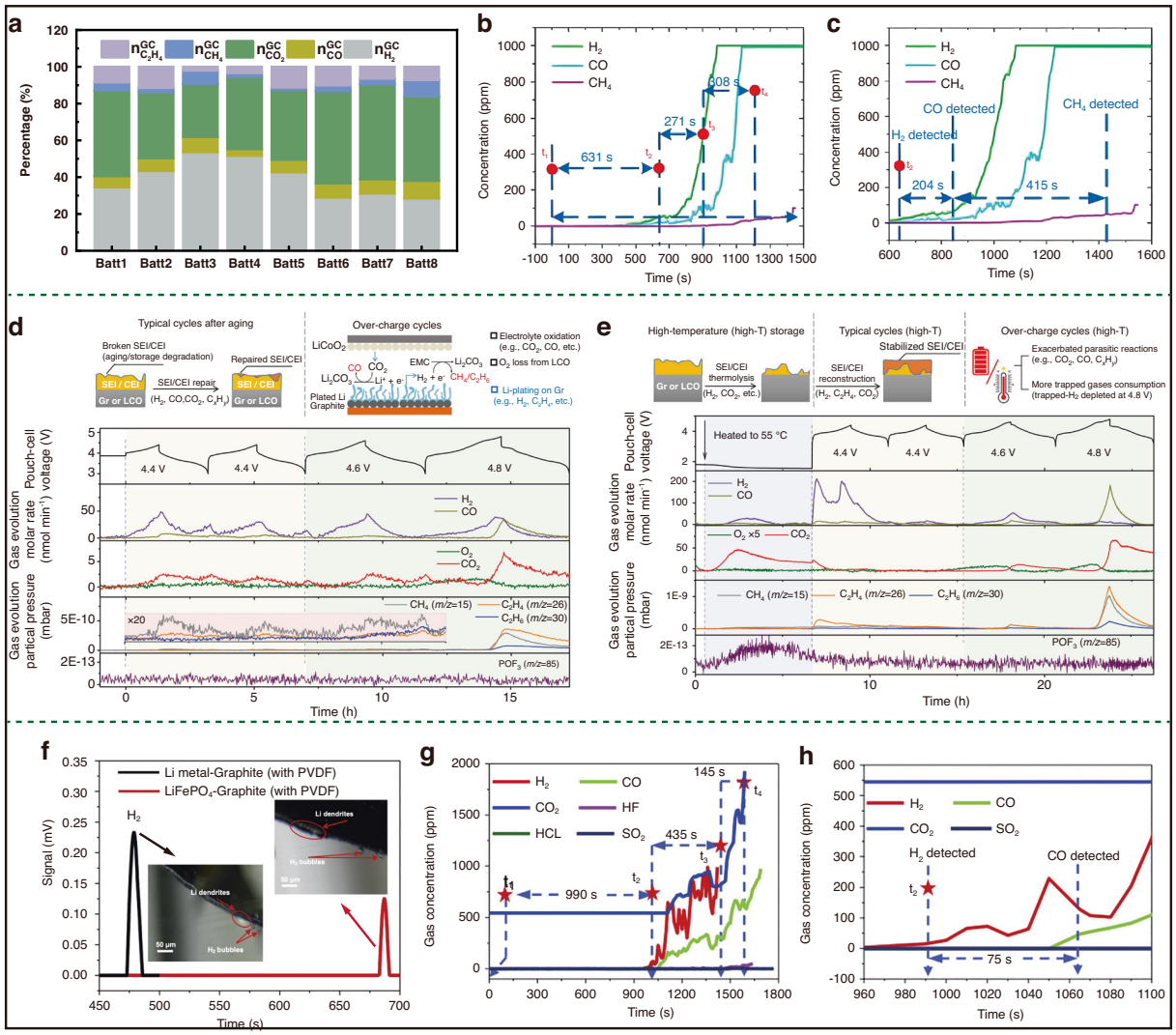

Fig. 2 The index gases released during TR process. a Histogram of proportion of main gas components according to the results of gas chromatography, which is obtained based on GC results of ref. [39]; **b**, **c** Overcharging test of battery 1 with real-time monitoring of three gases in the chamber[39]. Copyright 2023, Elsevier. The galvanostatic time–voltage profiles of stepwise increasing cut-off voltages (4.4–4.8 V) and real-time gassing behavior under different storage temperatures **d** RT, **e** high temperature, respectively[40]. Copyright 2023, Elsevier. **f** H_2 gas was captured at 683 and 472 s for the two kinds of assembled LIBs through automatic GC detecting and relative microscopy images of graphite anode surface during the charging process; **g**, **h** Overcharge experiment of a $LiFePO_4$ battery pack with online detection of six gases (t_1 represents the initial time of overcharge; t_2 represents the time when the gas sensor detects the characteristic gas; t_3 represents the time when white smoke is observed; t_4 represents the time when fire explosion occurs)[43]. Copyright 2020, Elsevier

detected gas under overcharge state (Fig. 2e). Figure 2f-h provide a micro-scale perspective on why detection of H_2 is essential for safety early warning because the release of H_2 gas can serve as an indicator for identifying the formation of trace Li dendrites, which are inducements of LIBs safety issues[43]. For the sake of safety warning, United States Department of Energy (US DOE) set a goal for the advancement of H_2 sensor in the applications of TR monitoring, hydrogen energy transportation and storage, including achieving the response/recovery time (t_{res}/t_{rec}) within 1 s for $H_2 \geq 1\%$, a broad detection concentration range of 0.1–10%, and a lifespan exceeding 10 years[44]. Therefore, development of H_2 sensors with fast response speed, high responsibility and stability is essential in real applications.

To date, various H_2 sensors have been briefly reported in the realm of H_2 sensing, including chemiresistive, electrochemical, optical, conductometric and catalytic-combustion H_2 sensors. As summarized in Table 1, electrochemical and optical sensors, while capable of sensitive and selective detection of H_2, suffer from high fabrication cost and performance degradation due to their

Table 1 The mechanism and characteristics of different types of hydrogen sensors

Classification	Mechanism	Advantages	Drawbacks
Chemiresistive	Based on changes of electrical signals (resistances or conductances) when H_2 molecules interact with the sensing materials.	High sensitivity; Acceptable stability; Ease of integration[37,49]; Low-cost fabrication.	Poor selectivity; Many sensors need high operating temperatures[459].
Electrochemical	Based on changes in charge transfer or electrical properties due to chemical reactions between H_2 and the sensor electrode, where H_2 is oxidized at the anode and O_2 is reduced at the cathode.	Low power consumption; Good selectivity[460]; High sensitivity[461,462].	Easy corrosion and difficult packaging for liquid electrolyte; Susceptible to ambient conditions (oxygen and humidity levels)[45]; High fabrication costs.
Thermal conductive	Detecting changes in the thermal conductivity of a gas mixture caused by the presence of H_2.	Fast response; Good stability[463,464]; Low cost.	Low sensitivity[48]; Susceptible to variations in flow rate and temperature[465].
Optical	Relying on changes in light intensity upon exposure to H_2.	Improved safety[52]; Anti-electromagnetic interference; High selectivity[46].	High cost; Difficult integration into battery production process[16].
Catalytic	Measuring the temperature increase generated by flameless combustion of H_2 on a catalytic surface for the detection of H_2	Low-cost; Fast response.	Poor selectivity[47]; High power consumption; Degradation of catalyst[466].

sensitivity to ambient condition fluctuations[45,46]. Catalytic sensors exhibit poor selectivity and pose safety risks in LIB applications due to their flameless operation[47]. Thermal conductive sensors lack the accuracy and sensitivity required for early warning detection[48]. Compared with other types of gas sensors, chemiresistive gas sensor offer more superiorities such as high sensitivity, acceptable stability and low cost of fabrication. Moreover, due to their ease of integration and compatibility with Micro-Electro-Mechanical-Systems (MEMS) techniques[37,49], miniaturized chemiresistive gas sensors have already demonstrated the potential to monitor released gases during TR process[32,50].

Therefore, this review primarily focuses on presenting a comprehensive overview of chemiresistive H_2-sensing mechanisms, research advances, and remaining challenges in H_2 sensors. first, the authors elucidate the essentiality of developing chemiresistive H_2 sensor with high performance (e.g., high sensitivity, sub-second t_{res}/t_{rec}, high stability, humidity tolerance, good selectivity, etc.) for the sake of safety issues of LIBs. Although the importance of hydrogen monitoring in new energy systems, storage, and transportation is well-established, its critical role in battery TR warning requires more detailed discussion. This review provides a distinctive focus on systematically analyzing why H_2 serves as one of the most essential gaseous markers for early TR detection in LIBs. Different to prior review articles which are merely focusing on few kinds of materials (e.g., Pd based H_2 sensors[51], 2 dimensional (2D) material H_2 sensor[52], or nanogap determined H_2 sensors[53]), this review provides a more comprehensive discussion of chemiresistive H_2 sensors based on various sensing materials, which are divided into the following categories metal-, metal oxide-, carbon-, transition metal dichalcogenide-, and III–V wide bandgap semiconductor-based H_2 sensors. Moreover, this review not only presents the advancements in enhancing H_2 sensor performance with respect to material and device design, but also emphasizes significant breakthroughs aligned with the standards set by US DOE for LIB safety. We believe this review will provide a forward-looking perspective on development H_2 sensors to meet US DOE's critical metrics.

Metal-based chemiresistive H_2 sensor

Among various metals, Pd is the most widely utilized metal for H_2 sensing and storage as it can reversibly absorb a volume of H_2 around 1000 times than its own[54–58], and has been reported to have a higher binding energy with H_2 compared with Pt, Au, Ru, etc[59,60]. Thus, in this review, we mainly focus on Pd-based and Pd functionalized H_2 sensors.

At room-temperature (RT), Pd reacts with H_2 molecules to form PdH_x hybrids, resulting in a significant increase in the overall resistance of the sensor, which transitions into a high-resistance state. Consequently, numerous Pd-based H_2 sensors have been developed, including those utilizing Pd nanomaterials, Pd-based alloys, and Pd-based

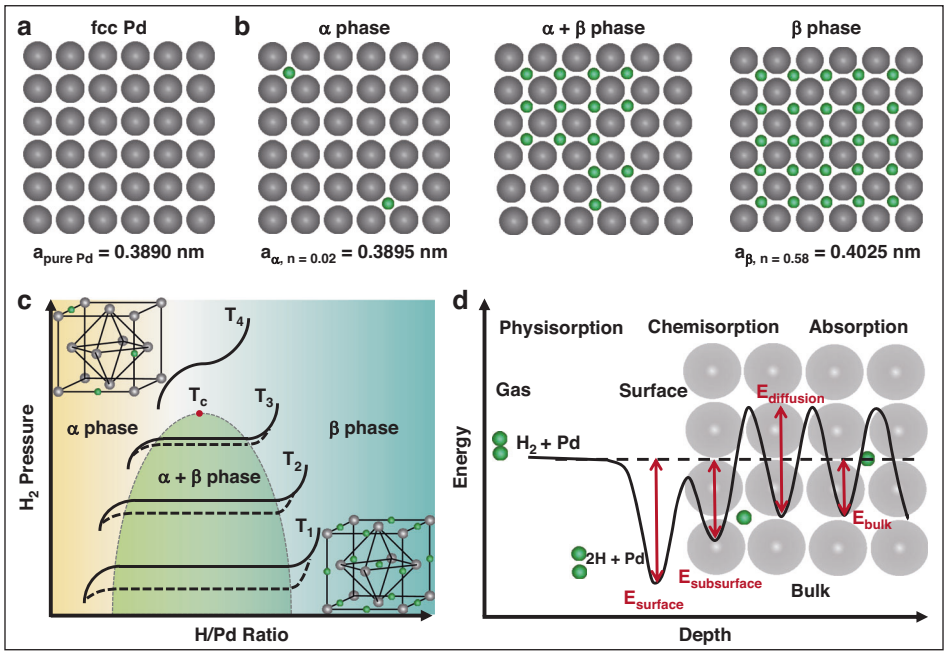

Fig. 3 The fundamental mechanism of Pd-based H_2 sensor. Schematic illustrations for (100) surface of fcc Pd (**a**) and the phases formed during H_2 adsorption (**b**); **c** PCT curves of bulk Pd-H on desorption process; **d** Energy landscape encountered by a H_2 molecule upon interaction with a Pd surface. In the first step, the H_2 molecule dissociates on the Pd surface into hydrogen atoms (H). In the next step, the H atoms diffuse into the subsurface region and occupy subsurface interstitial lattice sites. Subsequently, H diffuses interstitially further into the bulk

composites. In this section, we review the fundamental sensing mechanism of Pd based sensors as well as recent advancements in metal-based H_2 sensors.

Fundamental mechanism of Pd–H interactions

Since Graham et al.[61] first reported the hydrogen-storage property of Pd in 1866, the PdH_x hybrid has been systematically studied. During the adsorption process, H_2 molecules dissociate into hydrogen (H) atoms upon exposure to Pd, and these H atoms occupy the interstitial octahedral sites of a face-centered cubic (fcc) lattice as shown in Fig. 3a and b. Therefore, the transportation of free electrons within Pd crystal is impeded (namely electron scattering), and volume expansion of the Pd lattice occurs. The alterations in electrical properties and lattice expansion of the Pd crystal are significantly influenced by the composition of H atoms (x). When the x is in a low region ($0 < x < 0.02$), the PdH_x is stable at α phase with local expansion in Pd lattice, and the PdH_x is stable at β phase with huge lattice expansion when the x is in a high region ($x > 0.6$)[62]. While the two phases coexist when $0.02 < x < 0.6$. Researchers have demonstrated that the lattice expansion of Pd is positively related to the concentration of H atoms via powder X-ray diffraction (XRD) characterization[63–67]. Figure 3c presents the pressure-composition-temperature (PCT) curve of Pd-H system. With the increase of H_2 pressure, PdH_x undergoes a first-order phase transformation. During the coexistence of the α- and β-phases, a temperature-dependent plateau pressure is observed and as well as the hysteresis, which is generated by the PdH_x hydride formation and decomposition at constant temperature. Both the width of plateau and the extent of hysteresis shrink with increasing temperature, and ultimately vanishing as the temperature approaches the critical threshold (T_c). Figure 3d demonstrates a schematic graph of the energy landscape encountered by an H_2 molecule when interacting with a Pd surface. Obviously, the rate-limiting step in H_2 absorption involves the diffusion of H atoms from the Pd surface into its bulk.

As previously mentioned, the adsorption process of H_2 induces electronic change and lattice expansion. Therefore, electron scattering is the main sensing mechanism for Pd-based H_2 sensor, leading to an increase in sensor resistance[68,69]. A secondary mechanism associated with Pd-based sensor pertains to the volume expansion of Pd, which can be achieved through the design of discontinuous Pd nanostructures or films (nanogap-controlled Pd-based H_2 sensors). For the second type of sensor, the resistance decreases upon H_2 adsorption due to the formation of new electrical contact points within the Pd nanostructures/films[70–73]. However, the pressure plateau and the hysteresis of H_2 adsorption/desorption also cause a series of problems in H_2 sensing. First,

according to the PCT curve, the coexistence of two phases occurs within a narrow pressure range, leading to low sensitivity. Second, owing to the hysteresis loop between H_2 adsorption and desorption, it becomes challenging to obtain a precise signal related to H_2 pressure at any specific point in time. Therefore, to enhance the performance of Pd-based H_2 sensor (e.g., sensitivity, t_{res}/t_{rec}, and limit of detection (LOD)), researchers have proposed various approaches such as the design of Pd nanostructures, Pd nanogap, and Pd-M alloy nanomaterials. Compared to their bulk counterparts, Pd-based nanomaterials offer greater degrees of freedom such as size, shape, alloy composition, and nanogap distance, which can dramatically affect the H_2 sensing performance. Furthermore, linear detection of H_2 in a wide concentration range and long-term duration of Pd-based H_2 sensors are achieved via device structure design.

Pd nanostructure-based H_2 sensor

Recently, Pd nanomaterials have been utilized as H_2 sensing material due to their unique selectivity toward H_2, high specific surface ratio and quantum size effect. Yamauchi et al.[74] reported that decreasing palladium nanoparticle (NP) size leads to increased hydrogen solubility in α-phase, whereas β-phase shows a distinct behavior. Thus, the pressure plateau narrows and the T_c significantly decreases with reduced size of Pd NPs. In addition, decreasing the size of Pd nanomaterials may also reduce the t_{res} by shortening the diffusion distances for H atoms[75–77]. Langhammer et al.[78] were the first to measure the kinetics of H_2 adsorption and desorption in Pd NPs. They demonstrated that the kinetics exhibit a strong size dependence since both the adsorption/desorption times of H_2 decline with the reduction in Pd NP size, which is consistent with Monte Carlo simulation results of diffusion-controlled adsorption kinetics[78]. Thus, engineering efforts aimed at downsizing Pd nanomaterials would weaken the impact of pressure plateau and hysteresis[79–82]. Cho et al.[83] reported a H_2 sensor based on ultrasmall grained Pd NPs, which exhibited no hysteresis. Figure 4a displays the H_2 device structure derived from the fabricated Pd nanopattern arrays with the smallest grain size and interface dimensions of 5 nm and 2 nm, respectively. Attributing to the small grain size/interface, this unique Pd nanopattern array demonstrated the capability to detect a wide range of H_2 concentrations (2.5–30,000 ppm) with minimal hysteresis effects (Fig. 4b, c). It exhibited both lattice expansion and electron scattering mechanisms across different ranges of H_2 concentration. The lattice expansion mechanism predominates at low concentration ranges (2.5–100 ppm), resulting in a reduction in resistance upon exposure to H_2. In contrast, the sensor transitions to an electron scattering-dominated regime under high H_2 concentration ranges (0.5–3%), exhibiting an increase in sensor resistance. Kumar et al.[84] revealed that the polycrystalline Pd nanowires (NWs) exhibited faster t_{res}/t_{rec} and higher sensitivity throughout 0.1–1% H_2 compared to quasi-single-crystalline Pd NWs (Fig. 4d-h). The improved sensing properties is caused by the reduced grain size as well as exposed high-index active facets[84,85]. Li et al.[86] reported that Pd octahedrons with {111} facets have a fast response for H_2 adsorption compared with Pd cubes with {100} facets through XRD and in-situ solid-state ^2H NMR characterization. Except for reducing Pd NP size, increasing of exposed surface area is also an effective strategy for improvement sensor sensitivity. For instance, employing low-cost porous paper as a substrate greatly enhanced the sensitivity of polycrystalline Pd NWs-based H_2 sensor ascribing to the increased contact area of H_2 and Pd NWs, as shown in Fig. 4i. Different from previous reports that focus on reducing the size of Pd nanomaterials, Li et al.[87] fabricated highly sensitive H_2 sensors using Pd hollow shells (with ~10 nm thickness) by using Si nanoparticles (283 to 633) as template (Fig. 4j-l). The sensor achieved the LOD at 75 ppm when utilizing the largest Pd hollow shell size (633/10). Such sensitivity can be attributed to a larger volume expansion, which can effectively tune the sensor's resistance even at low H_2 concentrations. Consequently, decrease of the Pd particle size, increase of the exposure area of Pd, and construction of grain boundaries can considerably enhance the sensitivity and lower the t_{res}/t_{rec} of sensor toward H_2, as well as extend the detection range, achieving several ppm level LOD. However, the sensor exhibits t_{res}/t_{rec} spanning several hundred seconds, which hinders real-time application in providing early warning for TR in LIBs. Therefore, it is imperative to explore innovative strategies to enhance key sensing performance.

Pd nanogap-controlled H_2 sensor

Among Pd-based H_2 sensors, the sensing mechanism of Pd nanogap-controlled H_2 sensors is dominated by lattice expansion, resulting in an on-off behavior. These sensors usually exhibit high sensitivity, and fast t_{res}/t_{rec}. For this type of sensor, detecting conductive signals in the initial state (off-state) poses a challenge due to the presence of the formed nanogap. However, upon exposure to H_2 (on-state), there is a significant decrease in resistance attributed to lattice expansion that effectively bridges the nanogaps. In 2001 year, a Pd nanogap-based H_2 sensor was firstly proposed by electro-deposition of Pd mesowire arrays[71]. Although this Pd nanogap-controlled H_2 sensor demonstrated a rapid t_{res} (<75 ms), it exhibited a disadvantage in detecting trace H_2 since the LOD was 2.25% H_2[71]. While, by increasing the density of Pd NPs, the Pd mesowire-based sensor can operate as an always-on-state sensor, resulting in a reduced LOD of 0.5% H_2. Thus, the width of nanogap plays an essential role in determining

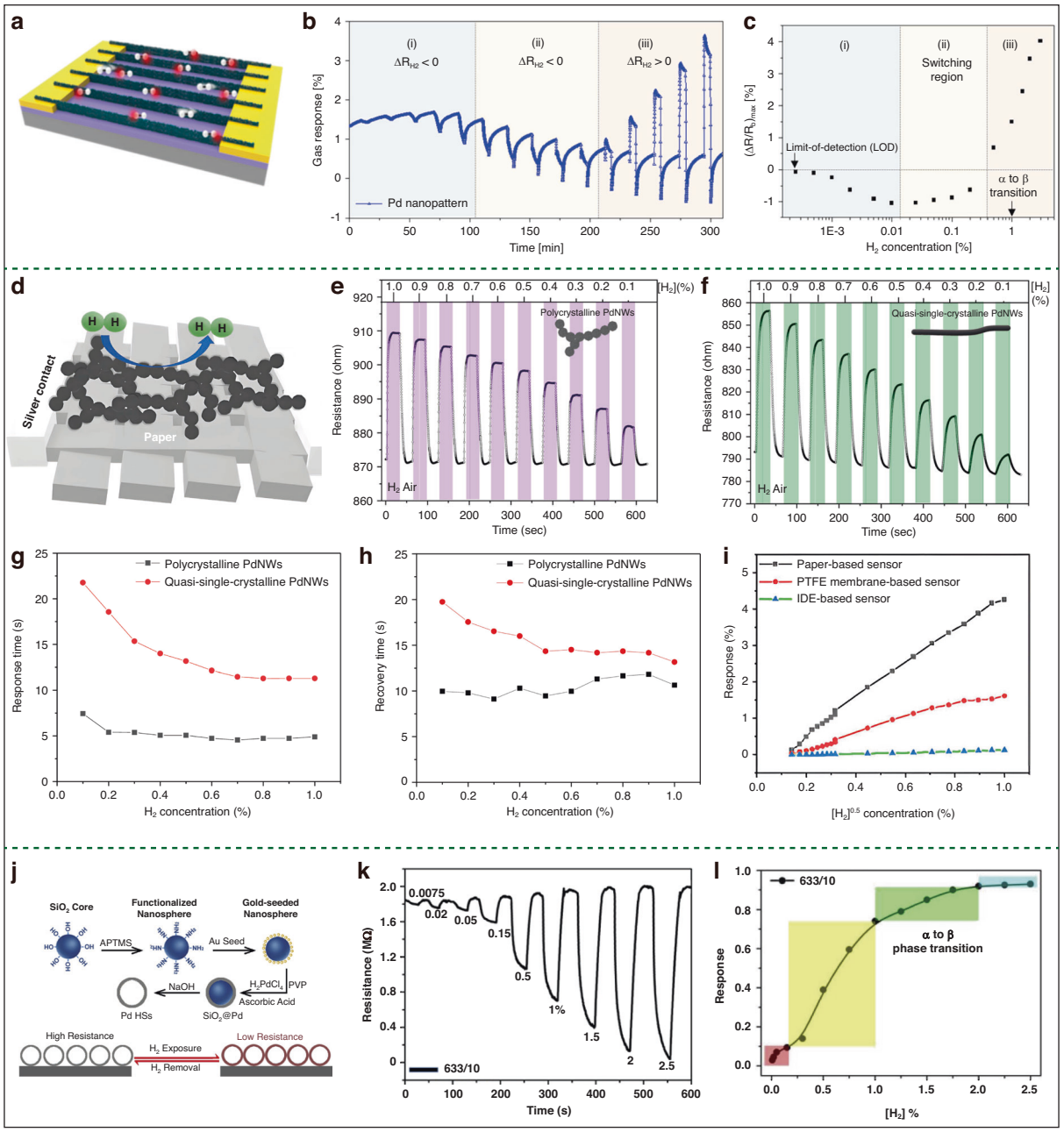

Fig. 4 H_2 sensors based on Pd nanograins. a–c Schematic graph of H_2 sensors based on a high-resolution Pd nanopattern with ultrasmall grain boundaries and relevant real-time dual-switching H_2 sensing behavior with variation of the H_2 concentration range[83]. Copyright 2018, American Chemical Society. **d–f** Schematic graph of paper-based H_2 sensor using polycrystalline Pd NWs and relevant dynamic H_2 sensing performance of two sensors; **g**, **h** t_{res}/t_{rec} vs H_2 concentration (0.1–1 vol %) of the sensors; **I** the influence of substrate to the sensing response of polycrystalline Pd NWs-based H_2 sensor[84]. Copyright 2023, American Chemical Society. **J** Schematic fabrication of Pd hollow shells; **k**, **l** Real-time response of Pd hollow shells to different concentrations of H_2 in N_2 at 25 °C and its plotted response curve (the core diameter is 633 nm and the shell thickness is ~10 nm)[87]. Copyright 2019, Elsevier

the performance of H_2 sensing. To date, there are two primary strategies for forming nanogaps: (i) a lithography-free method that uses an elastomeric substrate (ES) to fabricate Pd nanogap-based H_2 sensors; (ii) a lithography method employing rigid substrates.

For the first strategy, the formation mechanism of Pd nanogaps is ascribed to the differences in properties between ES and Pd films. Specifically, ascribing to the distinct Young's moduli of ES and Pd films, a Pd film-crack-based H_2 sensor was firstly fabricated through

mechanically stretching the ES-polydimethylsiloxane (PDMS)-to form nanogaps at the edge of the broken Pd films[88,89]. In addition, owing to the different volume expansion upon H_2 between Pd film and ES (which is insensitive to H_2), cracks are generated in the Pd film when removing the H_2 and the width of Pd nanogap can be modulated by varying the initial concentration of H_2[90,91]. In addition, the disparity in thermal expansion coefficients between Pd film and ES provides an additional force for nanogap formation when subjected to liquid nitrogen freezing treatment[92–96]. However, since the Pd films are simply deposited onto the surface of ESs, those sensors are suffering from poor mechanical stability and limited stretchability, thereby hindering their application in wearable electronic devices. To address this issue, Won et al.[97] proposed a sensitive and stretchable H_2 sensor by embedding Pd NP networks in PU fiber through a facile two-step chemical solution process as shown in Fig. 5a, b. The PU fiber was firstly immersed in a Pd precursor solution, subsequently, it was air-dried before being immersed in a reducing agent. Figure 5c demonstrates that the obtained H_2 sensor exhibits a wide sensing ranging from 5 to 100000 ppm, with the capability to detect under strains of up to 110%. Son et al.[98] used the similar method to develop a H_2 sensor based on PdO NPs-embedded carbon nanotube (CNT) yarns, which demonstrated well-maintained sensing performance under two deformation states, namely, bending and loading. Therefore, embedding sensing material networks into ESs presents a promising approach for enhancing stability, despite the random distribution of nanogaps with varying widths. To precisely control the width of nanogap, a rigid substrate (e.g., steel foil) was used to fabricate Pd/Cr nanogap H_2 sensor via one-step bending deformation by using a cylinder[99]. The width of the nanogap can be adjusted from 8 to 80 nm by varying the diameter of the cylinder (1–6 mm) (Fig. 5d). Figure 5d illustrates a schematic diagram of the fabricated sensor, which consists of 4 layers, namely, a steel substrate, Kapton tape, a 3 nm Cr film, and a 2 nm Pd film, respectively. The sensor based a single nanogap (15 nm) works as an on-off behavior and exhibits an optimized sensing performance, including broad detection range (0.0001–4% H_2), good repeatability and fast t_{res}/t_{rec} (3/4.5 s) as displayed in Fig. 5e-g. Moreover, lithography method is also an another effective strategy to precisely control the width of the Pd nanogap with high uniformity and repeatability[100,101]. However, achieving sub-100 nm gaps using conventional UV lithographic techniques poses significant challenges[101–103]. To address this problem, a self-aligned nanogap is formed using oxidized Cr film as a shadow by using two steps of photolithography and the width of nanogap (45–300 nm) depends on the thickness of Cr film (Fig. 5h)[101]. Figure 5h also displays the cross-section diagram of a sensor, clearly showing that the Au and Pd films are partially suspended due to the third photolithography for selective wet etching of the underlying SiO_2 layer. This suspended film structure provides enough space for the expansion of the Pd film when exposure to high concentration of H_2 (4%). Figure 5i-k presents the dynamic sensing response of the suspended Pd film, demonstrating that the sensor is capable of detecting H_2 concentrations ranging from 1% to 4%. To improve the sensitivity to low H_2 concentrations, Pak et al.[100] proposed a strategy for fabricating a 15 nm nanogap sensor through transferring a deposited PdAu film onto a polystyrene substrate using a Si stamp with periodic gratings measuring 500 nm in width and 100 nm in height (Fig. 5l, m). During the detachment process, the width of the PdAu nanogap decreases in a controllable manner (from 40 nm to overlap) due to variations in the shrinkage degree of the PS substrate at different detachment temperatures. The 15 nm PdAu nanogap sensor demonstrates a fast t_{res} (11.54 s) across the full detection range of H_2 concentrations (0.005–10%) and the sensing response is much higher than that of sensor based on pure Pd nanogap (Fig. 5n and o). Therefore, precisely control the nanogap width of nanogap architectures has shown promise in enhancing sensitivity ($\Delta R/R_0 > 1$), expanding detection range (several ppm to 4% H_2), and accelerating response/recovery dynamics (few seconds). However, there is remain a significant gap in meeting the targets set by US DOE, which specify a t_{res}/t_{rec} within 1 s for H_2 concentrations ≥ 1%. While this disadvantage could be addressed by integrating with algorithms as discussed in the following section "Pd-based H_2 sensor integration of algorithms".

Pd alloy-based gas sensor

As discussed above, there are two primary sensing mechanisms for Pd-based H_2 sensor. However, current pure Pd-based sensors face challenges due to their high cost and inherent hysteresis associated with hydride formation and decomposition, which significantly diminishes sensor accuracy[104]. The fabrication of Pd alloys with other metals (Ms) presents an effective approach to reduce costs and eliminate hysteresis, as confirmed by both theoretical calculations and experimental tests[105,106]. The presence of the second M, which is non- or weak hydride former, increases the energy barrier for hydride formation during hydrogen absorption[51,105]. When the atomic radius of the alloyants exceeds that of Pd, such as Au, Y, and Mo, the lattice structure of Pd expands, thereby reducing the strain-induced energy barrier caused by hydrogen absorption[104]. Mamatkulov et al.[105] used density functional theory (DFT) to study the influence of other Ms and presented that the hysteresis of Pd toward H_2 can be dramatically suppressed by introducing Au and Ta. According to their

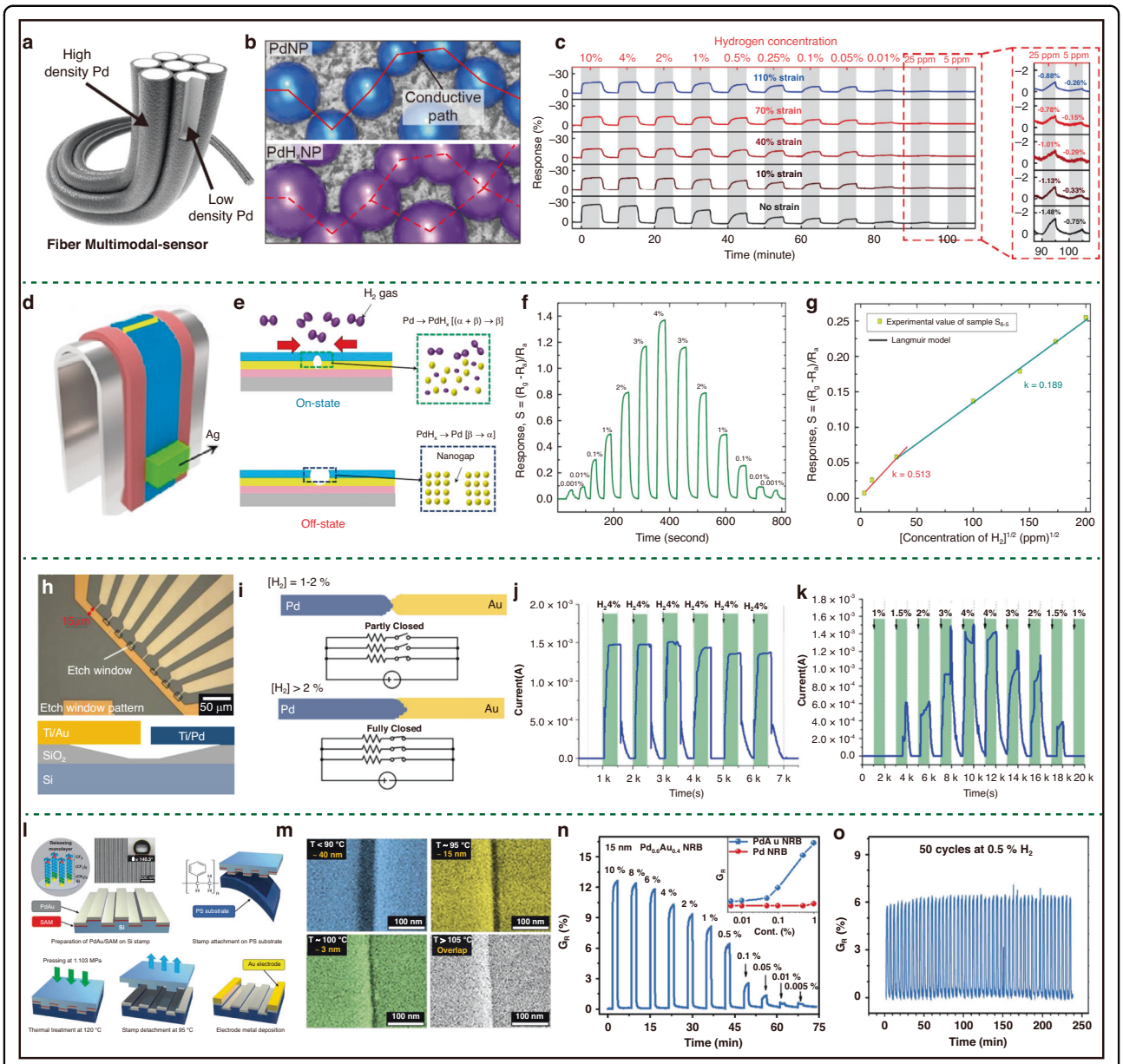

Fig. 5 Different strategies for the design of Pd nanogap controlled H_2 sensors. a Schematic graph of the fiber multimodal sensor and **b** structure of the conducting network regarding Pd NPs and PdH_x NPs on the surface of fiber; **c** response of the 0–100% strained sensor for 10% to 5 ppm H_2 gas[97]. Copyright 2020, American Chemical Society. **d** Schematic diagram of fabricated Pd/Cr nanogap sensor and **e** its on-off operation mechanism; **f** Real-time resistance sensing response of optimized Pd/Cr gap sensor for various H_2 concentrations (10–40,000 ppm) and **g** resultant linear correlation[99]. Copyright 2020, Elsevier. **h** Optical image of the Pd nanogap H_2 sensor and its schematic cross-sectional structure; **i–k** Schematic illustrations of the sensor structures and sensing operations in response to two different H_2 concentration ranges[101]. Copyright 2022, American Chemical Society. **l** Schematic fabrication procedure of PdAu nanogap sensor; **m** SEM images of four samples with different nanogap widths when detached at different temperatures; **n** dynamic sensing response of a 15 nm $Pd_{0.6}Au_{0.4}$ sensor to 0.005–10% H_2 and **o** the repeatability test to 0.5% H_2[100]. Copyright 2018, John Wiley and Sons

calculations, the fraction (f) of the second M, H-M interaction (ε_{HM}), and effective M-M interaction (ε^*) play crucial roles in suppression of hysteresis in Pd, as shown in Fig. 6a-c. In pure Pd (Fig. 6a), H_2 is absorbed at RT up to an H/Pd ratio of ~0.66, which exhibits considerable hysteresis with a high T_c (600 K). While the hysteresis loop in the alloys shifts to the left, and the T_c of $Pd_{0.85}Ta_{0.15}$ decreases to ~320 K (Fig. 6b). Notably, the reduction in T_c exhibits a positive correlation with ε_{HM} when compared with other additives[105]. Figure 6c illustrates that an increase in f can significantly suppress hysteresis as well. Therefore, considerable efforts have been made to develop hysteresis-free

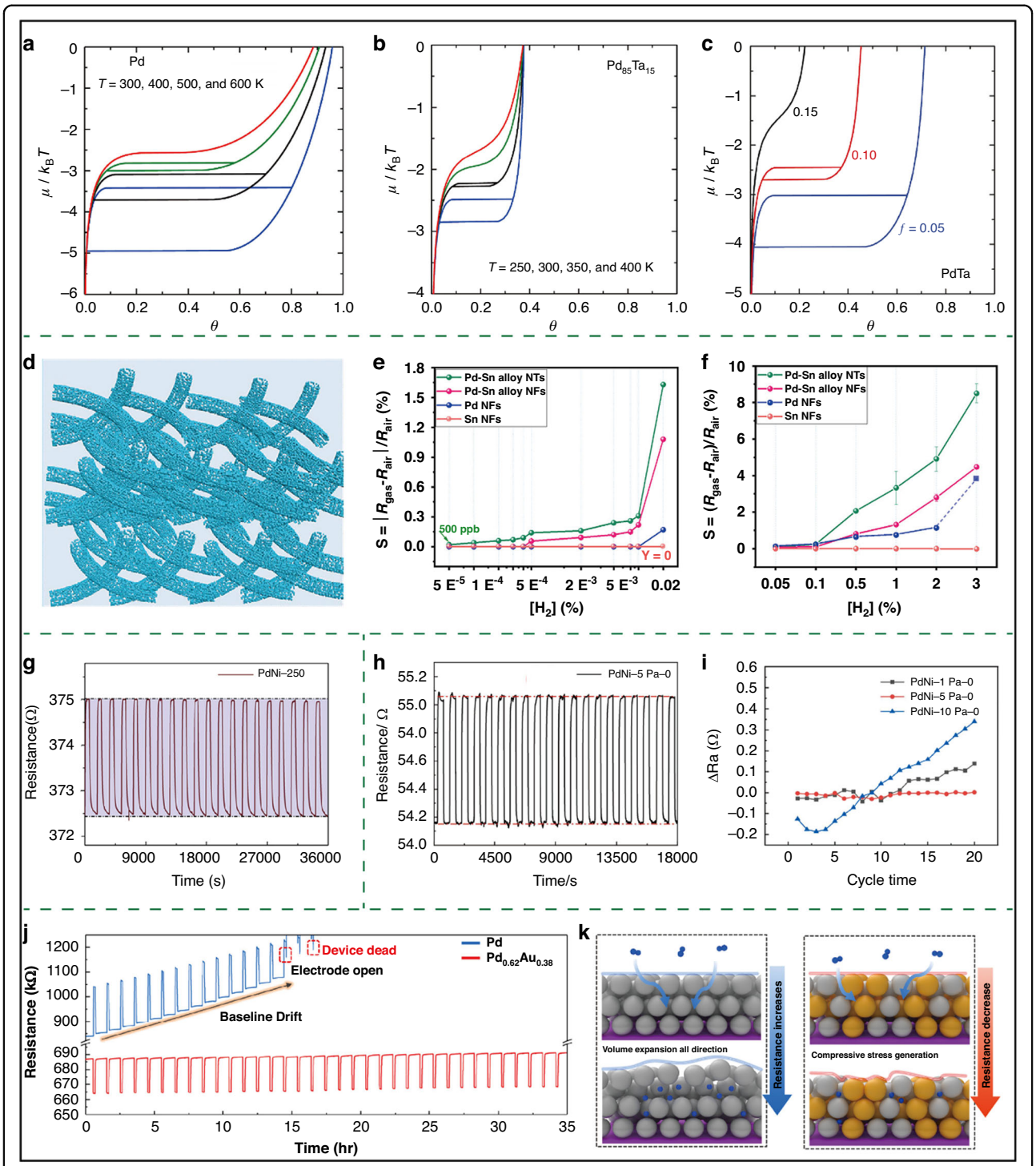

Fig. 6 The advantages of H_2 sensors based on Pd-M alloy. Calculated H_2 adsorption isotherms for **a** pure Pd and **b** $Pd_{85}Ta_{15}$ alloy at four different temperatures; **c** calculated H_2 absorption isotherms for the Pd-Ta alloys at 30 °C[105]. Copyright 2021, Elsevier. **d** Schematic diagram of prepared PdSn alloy NTs; Normalized response versus H_2 concentrations for PdSn alloy NTS, PdSn NFs, Pd NFs, and Sn NFs at H_2 concentrations of **e** 0.5–200 ppm and **f** 500–30,000 ppm[111]. Copyright 2022, American Chemical Society. **g** repeatability test for 1% H_2 of PdNi alloy film annealed at 250 °C[113]. Copyright 2020, Elsevier. **h** Repeatability test for 1% H_2 of PdNi alloy film prepared under 5 Pa and **I** the variations in $_{\Delta}R$ values of three PdNi alloy samples deposited under different pressures[114]. Copyright 2024, Elsevier. **j** Long-term repeatability curves of the nonalloyed Pd and $Pd_{0.62}Au_{0.38}$ sensors at 5% H_2 atmosphere and **k** schematic of the mechanism of resistance change when H_2 penetration occurs in Pd and PdAu[115]. Copyright 2024, American Chemical Society

H_2 sensors based on Pd alloys, particularly in comparison to sensors based on pure Pd, especially in the realm of optical H_2 sensors[107–109].

In addition, the introduction of a second M can significantly improve the sensing performances of the sensor, including sensitivity, stability and t_{res}/t_{rec}. Zhao et al.[110] demonstrated that PdAu alloy-based sensors achieved a 3.9-fold faster t_{res} and a 1.1-fold faster t_{rec} compared to pure Pd-based devices. Additionally, the PdAg alloys exhibited a higher sensitivity for H_2 detection than pristine Pd. Kim et al.[111], employed Sn as a second M to fabricate low-cost PdSn nanotube (NT)-based H_2 sensors. Although Sn itself is not particularly sensitive for H_2 sensing, its presence significantly improves both the sensitivity and tolerance of the sensor up to 4% H_2 (Fig. 6d-f). Because PdSn alloys exhibit lower oxygen adsorption energy compared to pristine Pd, they can facilitate a greater amount of chemisorbed oxygen species, thereby enhancing the sensitivity of the sensor. Furthermore, when exposed to high concentrations of H_2 (0.05–3%), the presence of Sn effectively inhibits phase transitions and the growth of Pd nanograins, significantly improving the endurance and stability of sensor to under elevated H_2 concentrations. Similarly, the incorporation of 8% Ni into Pd film also can significantly inhibit the α-β transformation, thereby enhancing the sensor's tolerance of the up to 4%[112]. Additionally, a zero-drift suppression in PdNi alloys has been reported through the reduction of defects in PdNi alloy films via annealing treatments (Fig. 6g)[113]. Liu et al.[114] obtained PdNi alloy films with different morphologies by adjusting the deposition pressure and founded that the degree of rearrangements in the alloy structures is influenced by their morphologies. As a result, the sensors (PdNi-5 Pa-0) featuring tiny cracks, which were obtained under a pressure of 5 Pa, exhibited superior stability compared to those obtained under different deposition pressures (Fig. 6h, i). This enhanced stability can be attributed to the minimal structural rearrangement observed after exposure to H_2. Kim et al.[115] reported a H_2 sensor based on PdAu alloys, which demonstrated excellent durability with an optimized composition of $Pd_{0.62}Au_{0.38}$. The drift of the baseline and changes in sensing response are neglective (only 0.02% per cycle) during over 35 h of repeated operation in 5% H_2, as illustrated in Fig. 6j. Whereas the resistance of Pd drifted significantly, averaging 1.6% of the initial value per cycle, and failed completely after 15 cycles (Fig. 6j). Notably, in contrast to sensors based on pure Pd, the $Pd_{0.62}Au_{0.38}$-based sensor illustrated a decrease in resistance when exposed to H_2. The relative sensing mechanism is illustrated in Fig. 6k. For sensors based on pure Pd, the formation of PdH_x in Pd lattice results an increase in resistance. Whereas, when H atoms penetrate the octahedral sites of Pd_4Au_2, it induces the displacement of Au atoms while simultaneously compressing the Pd matrix. The displaced Au atoms are then compressed together with those Au atoms sites that remain unoccupied by H atoms, leading to the formation of a compressed layer. This induced pressure consequently results in a decrease in resistivity within the compressed metal structure. Thereby, construction of Pd alloys cannot only reduce the cost but also can improve sensing properties, including suppressing hysteresis enhancing sensor sensitivity and stability. Particularly, the long-term stability over months has been verified experimentally, during which both the signal response and baseline resistance remained virtually unchanged. Such remarkable stability underscores the reliable deployment of Pd alloys in the demanding environment of battery safety monitoring.

Novel Pd-based H_2 sensor design

Pd nanograins, Pd nanogaps, and Pd alloys have been reported to enhance the sensor performance, such as sensitivity, stability and reduce of hysteresis. However, due to the inevitable phase transition upon H_2 concentrations above 2%, it induces undesirable electrical and mechanical alterations for the sensors based on Pd. In particular, nonlinear gas response ($\Delta R/R_0$) associated with phase transitions has posed a significant challenge for detection of high H_2 concentrations. Although fabrication of Pd alloys is an efficient approach to suppress phase transition and shows the capability to detect H_2 in high concentrations, it is difficult to explicitly control the material composition with the alloying method for nanofabrication with high reproducibility[116,117]. Unlike material alloying, employing a mechanical approach to suppress lattice expansion offers greater flexibility in the design of nanomaterials. Kim et al.[79] reported that the phase transition is suppressed by introducing of a buffer layer at the interface of the Pd film and substrate. In 2022, Yoon's group designed a phase transition-inhibited Pd nanowire H_2 sensor that can linearly detect H_2 up to 4% with high sensitivity by inserting a layer of Al_2O_3 between Pd and substrate[118]. Figure 7a shows the schematical graph of the Pd NWs-based sensor. The device comprises an aligned array of Pd NWs serving as the sensing material, equipped with four electrodes. Figure 7b presents the mechanism of suppression of phase transition. As mentioned, the formation of PdH_x leads to the lattice expansion of Pd. However, as the bottom of the Pd NWs is anchored to the substrate, a compressive stress is formed at the interface between Pd NWs and substrate to constrain the volume expansion. Considering this factor, the phase transition would be inhibited, particularly in regions adjacent to the substrate where high levels of compressive stress are generated. It was calculated that at least 0.25 GPa stress is needed to prevent phase transition

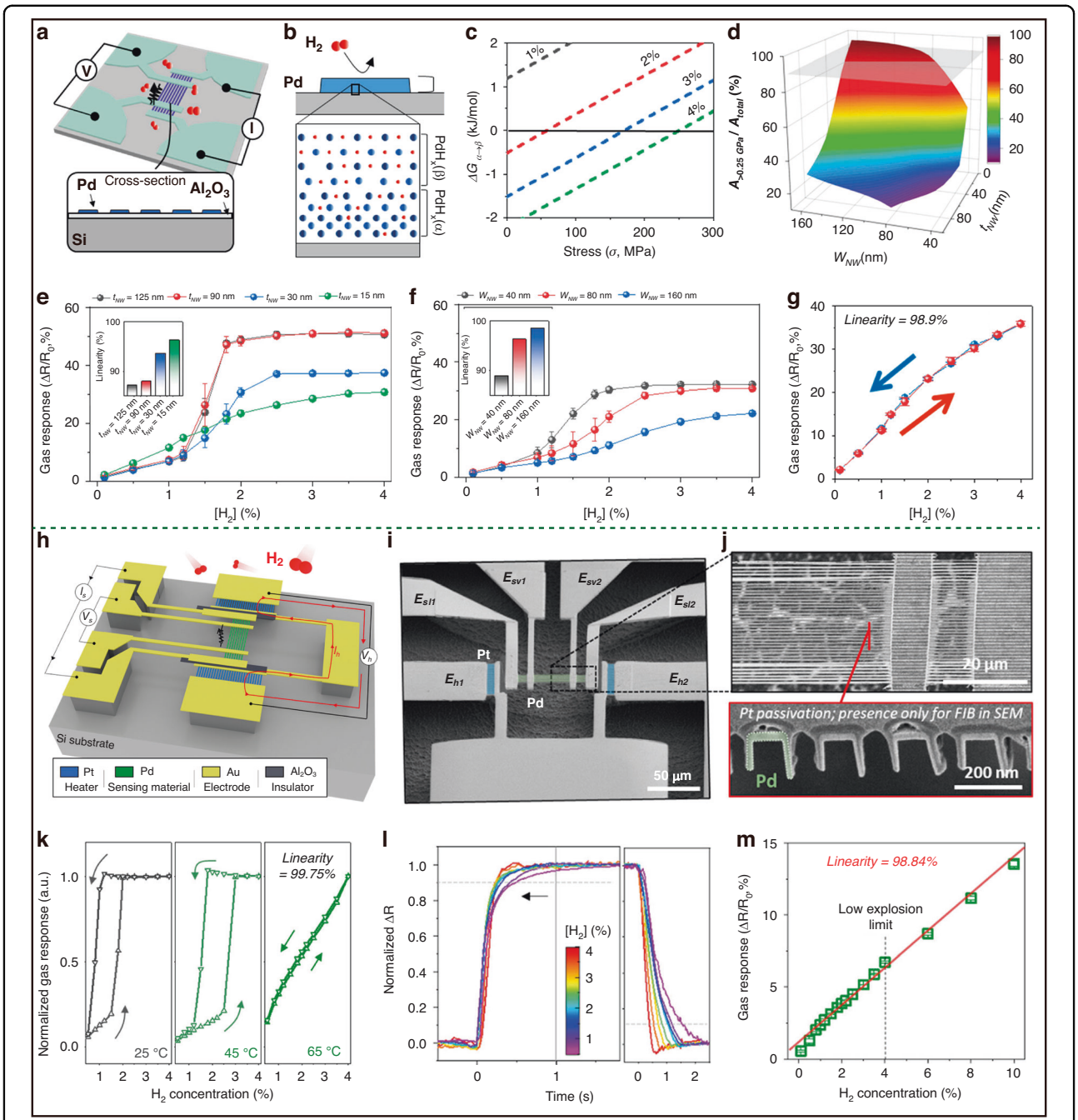

Fig. 7 The strategies for improving the sensing linearity of Pd based H_2 sensors. a Schematic illustration of perfectly aligned Pd NWs based H_2 sensor with inhibited phase transition. **b** Schematic of the internal lattice structure of Pd NWs with two phases; **c** Gibbs free energy change of PdH_x phase transition ($\Delta G_{\alpha\rightarrow\beta}$, kJ/mol) according to stress (σ) at four different concentrations of H_2. **d** Ratio of a cross-sectional area with a stress greater than 0.25 GPa to the total area with respect to w_{NW} and t_{NW}; Influence of **e** t_{NW} and **f** w_{NW} of the Pd NWs to the H_2 sensing performance; **G** Gas response based on optimized Pd NWs sensor (w_{NW} = 160 nm, t_{NW} = 15 nm) as increasing and decreasing H_2 concentration[118]. Copyright 2022, American Chemical Society. **h** Schematic graph and **I**, **j** SEM images of the nanoelectromechanical H_2 sensor; **k** Hysteresis characteristics depend on the sensor temperature; **l** Response time and **m** linear gas response according to the H_2 concentrations at 65 °C[119]. Copyright 2023, American Chemical Society

at 4% H_2 (Fig. 7c). Based on the assumption that PdH_x expands with a linear expansion coefficient of 3.5%, the author found that the stress distribution of the Pd NWs depends on their geometrical dimensions such as the thickness (t_{NW}) and width (w_{NW}) of Pd NWs by using a finite element method. Figure 7d demonstrates the stress

distribution of a Pd NW results when the proportion of the area with a stress greater than 0.25 GPa to the total area ($A_{>0.25\ GPa}/A_{total}$). Thus, to accommodate the stress between Pd NWs and the substrate during absorption of H_2, a lot of efforts have been done to modulate the thickness and width of Pd NWs to implement linear detection of H_2 concentrations up to 4% (Fig. 7e and f). Highly linear and distinguishable gas response (linearity = 98.9%) for up to 4% H_2 was achieved by optimizing the geometrical dimensions of Pd NWs ($t_{NW} = 15$ nm, $w_{NW} = 160$ nm), as displayed in Fig. 7g. In 2023, to further broaden the linear detection up to 10% H_2, Yoon's group employed thermal activation mechanism to achieve fast response rate and inhibit the phase transition of PdH_x through device structural design[119]. Because providing thermal energy to Pd is an effective approach for enhancing the response rate by accelerating the hydrogen adsorption process and thermodynamically inhibiting the phase transition. The schematic graph of the device is displayed in Fig. 7h. Different to conventional device structures, in which a heater, an insulating layer, and sensing materials are vertically arranged, the Pt heaters are laterally placed at the bottom side of the suspended Pd NWs with C-channel-shape feature (Fig. 7i, j). This unique structure can maximize the exposed reaction sites of the Pd NWs and raising the temperature by lateral heaters. By measuring the continual gas response of the device depending on the temperature, the operating temperature for a linear gas response without phase transition is 65 °C (Fig. 7k). The designed sensor demonstrates the capability to detect H_2 within 0.6 s, which is the fastest detection rate in metal-based chemiresistive sensors at the time of publication, with high linearity (98.8%) across a concentration range of 0.1–10% at 65 °C when the thickness of Pd is 20 nm (Fig. 7l and m). Therefore, ingenious device structure design can also suppress phase transition and expand the linear detection range. This strategy demonstrated a potential approach for the early detection of H_2 in TR process. Moreover, if incorporating strategies discussed in prior sections, further improvements in sensitivity could be achieved to realize the practical deployment in LIB safety systems.

Pd-based H_2 sensor integration of algorithms

Rapid H_2 detection is the prerequisite of LIB TR monitoring. Therefore, it is essential to develop a fast H_2 sensing system with a wide detection range. Although Pd alloys can efficiently broaden the linear detection range and enhance the stability, while the t_{res}/t_{rec} of most the reported chemiresistive sensors still unable to meet the requirement of US DOE[111–114,118]. To address this issue, integration of algorithm in the H_2 sensing system to predict the H_2 concentration based on first few data samples could achieve ultrafast alarming (<1 s). Leveraging the advantages of Pd alloys and the principle that heating can mitigate hysteresis, Huang et al.[120] developed a PdNi alloy based H_2 sensor with the capability of fast detection of 0.1–4% H_2 at 40 °C (<1 s) as shown in Fig. 8a-d. Although the t_{res} of the sensor meets the requirement of US DOE under specific conditions, the t_{res} still exceed 1 s toward H_2 concentration lower than 1% (Fig. 8c, d). To tackle this problem, the authors develop a neural network concentration prediction method utilizing an autoencoder architecture for faster concentration output (Fig. 8e). The underlying mechanism is grounded in the adsorption kinetics of H_2 on Pd. After acquiring the real sensor response dataset, zero drift compensation and normalization were applied to minimize drift impact data scale differences. The mean (μ) and standard deviation (ω) of the first 50 values of the baseline was calculated and used to set the threshold ($\mu + 3\omega$) for determining the start of a response. The start value r[t] is determined when $r[t]-r[t\text{-}1] > \mu + 3\omega$. Once the initial $r[t]$ is obtained, a short segment of early response signal (40 data points, 150 Hz, ~0.3 s) is used as the input to the algorithm. Therefore, by extracting ~0.3 s data segment to the H_2 concentration model which is consisted of an encoder and a fully connected neural network (FCNN) can successfully predict H_2 concentration. It can be clearly observed that most of the predicted concentrations are almost consistent with the true concentrations, the relative error has a mean error of 0.17% and standard error of 1.36%. A similar PdNi based H_2 sensor, which is using polyimide film as substrate, with the ability to detect as low as 5 ppm is reported by the same research group (Fig. 8f-g)[121]. Furthermore, by integration with the prediction model algorithm, the alarm triggering time was greatly shortened to 0. 4 s compared to the system without the algorithm (Fig. 8h, i). Therefore, integration algorithm to the H_2 detection system offers a promising solution to decreasing the alarm time within sub-second under the full detection range.

Table 2 presented sensing properties of metal-based H_2 sensors. In summary, Pd is a typical metallic chemiresistor for H_2 detection through phase transition mechanism and lattice expansion mechanism. Although Pd-based sensors are capable of detecting H_2 at RT with high selectivity, they usually displayed poor sensing properties, such as low responses and long t_{res}/t_{rec}. To date, various approaches have been reported to enhance their sensing performance including reducing size of Pd NPs, employing Pd alloys, construction of Pd nanogaps, design novel device structures, and integration with prediction algorithms. Some of these strategies are capable to enhance the sensor's stability, broaden the linear detection range, and improve the t_{res}/t_{rec} for real-time TR monitoring. However, the expense associated with noble-metal-based sensors is significantly higher than that of other sensing materials, which may pose a challenge for their commercialization.

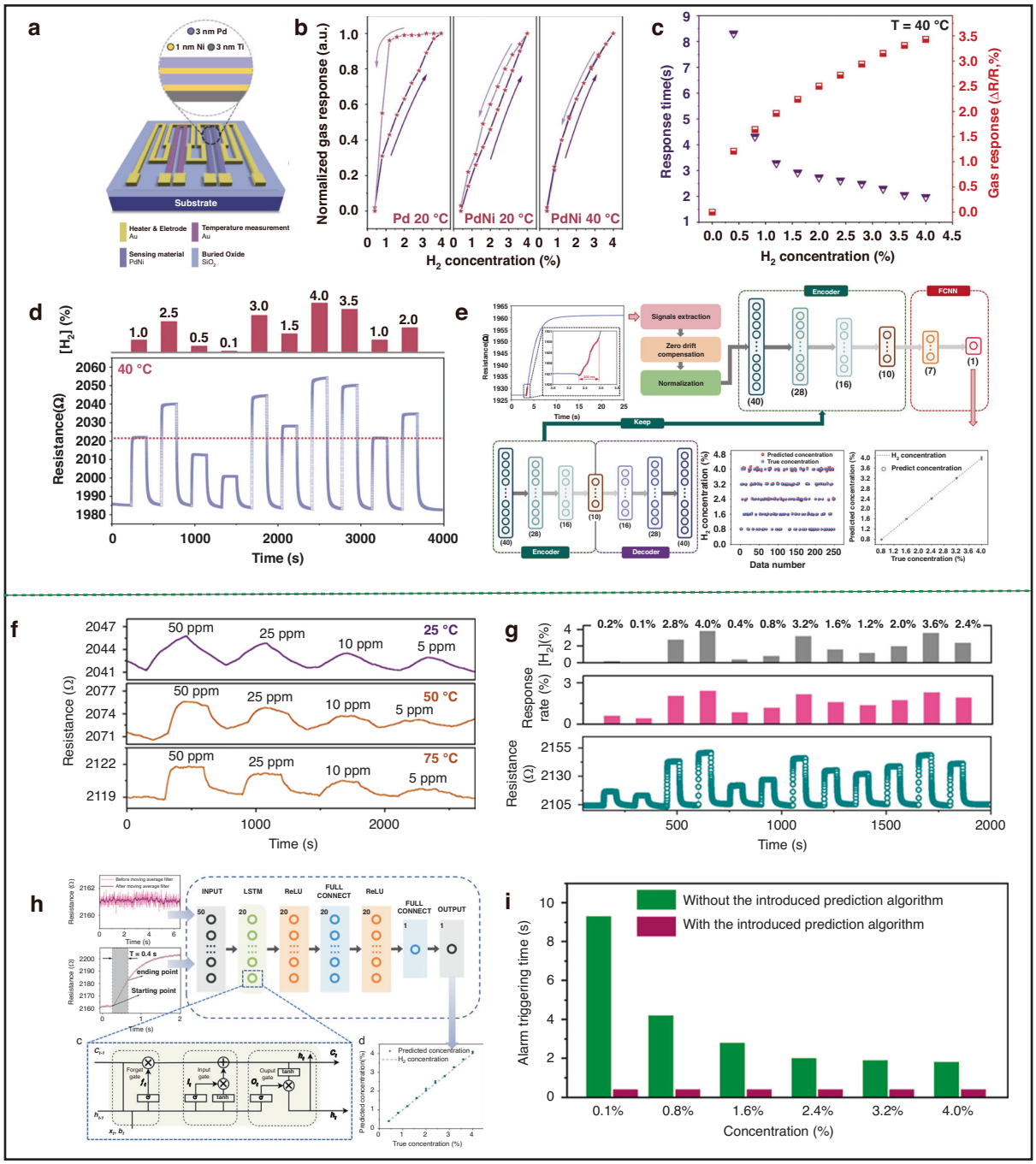

Fig. 8 Advantages of integrating algorithms into H_2 sensors. a Schematic diagram of the coplanar-structured H_2 sensor based on a PdNi film; **b** Hysteresis characteristics depend on the sensing material and temperature; **c** t_{res} and response value of the sensor towards 0.4–4% H_2; **d** sensor response towards various random H_2 concentrations; **e** working principle and flowchart of the prediction algorithm and its predicted results[120]. Copyright 2025, Elsevier. **f**, **g** Dynamic sensing response of PdNi film-based sensor upon 5–40,000 ppm H_2; **h** prediction algorithm of H_2 sensing system; **i** Comparison of the response time of the detection system with and without the introduced prediction algorithm for different concentrations of H_2[121]. Copyright 2025, American Chemical Society

MOS-based chemiresistive H_2 sensor

The MOS-based resistive gas sensors have garnered great attention due to their high chemical and thermal stability, rapid t_{res}/t_{rec}, and low cost, positioning them as a primary research direction for H_2 sensing. However, the sensitivity of MOS-based sensors is fundamentally reliant on the redox reactions that occur between adsorbed oxygen species and target gases. This intrinsic mechanism cannot

Table 2 Summary of sensing properties of metal-based H_2 sensors

Material	T (°C)	detection range (ppm)	Tested concentration (ppm)	Response	t_{res} /t_{rec} (s)	Tested LOD (ppm)	Ref.
quasi-single-crystalline Pd NWs	RT	100–10,000	10,000	8%[a]	9.3//13	100	84
Pd NSs	RT	5–10,000	10,000	0.4%[a]	50/60	5	467
Pd NPs	RT	2.5–30,000	30,000	~4%[a]	12/19	2.5	83
half-pipe Pd NTs	RT	8000–18,000	18,000	2.1%[a]	12/18	314	468
Pt NWs	RT	0.01–1,000,000	1000	14%[a]	NG/NG	0.01	469
Pd NWs	RT	1000–39,000	30,000	~41.9%[a]	~85.7/~296	1000	470
Pd NWs	65	1000–100,000	40,000	~5.8%[a]	0.6/<2	1000	119
Pd NWs on Al_2O_3	RT	0.1–4%	30,000	~30%[a]	56/NG	1000	118
suspended Pd NWs	RT	4000–20,000	20,000	4.8%[a]	~350/~70	4000	471
Pd hollow shells (450/10)	RT	250–25,000	10,000	60%[a]	16/NG	250	87
Pd NPs cracks on PU	RT	5–100,000	40,000	~27%[a]	32.3/~38	5	97
Pd/Cr nanogap	RT	10–40,000	10,000	50%[a]	3/4.5	10	99
Pd nanogap	RT	15,000–40,000	15,000	On/off manner	22/NG	15,000	101
$Pd_{0.6}Au_{0.4}$ nanogap (15 nm)	RT	5–100,000	10,000	~8.1%[a]	11.54/9.83	5	100
Pd nanogap contains Au/Cr buffer	40	20–60,000	40,000	~55%[a]	60–170/ 30–240	20	103
PdAu Sensor	RT	3000–30,000	30,000	NG	204/198	3000	48
Pd@Pt@Yarn	RT	1–40,000	40,000	9.54%[a]	12/48	1	472
Au@Pd (17/4)	RT	1000–1,000,000	10,000	>225%[a]	NG/NG	1000	473
Pd-Sn Alloy NTs	RT	0.5–30,000	20,000	5.2%[a]	20.2/17.9	0.5	111
Pd-Ni+organosillica membranes	70°C	1–400	200	121%[a]	107/NG	1	474
Ag-Pd/Cr	200	800–40,000	40,000	2.13%[a]	80/170	800	475
PdMoY nanosheets	RT	1–1,000,000	10,000	18.7%[a]	73/40	1	104
Pd/Ni film	75	800–20,000	20,000	3.17%[a]	7/6	800	476
PdNi film	RT	2–10,000	10,000	~0.7%[a]	~315/~100	2	113
$Pd_{63}Co_{37}$ NWs	RT	1000–30,000	1000	~5-6%[a]	85/200	1000	477
PdNi film	40	2–40,000	40,000	~3.3%[a]	0.3/~	2	120
PdNi film	75	5–40,000	40,000	~2.3%[a]	0.4/~	5	121

[a]Refers $S = \Delta R/R_0$ or $\Delta R/R_g$

completely eliminate cross-sensitivity, which ultimately constrains gas selectivity. In addition, many MOS-based gas sensors require high operation temperatures (>200 °C) to ensure an adequate number of charge carriers enter the conduction band for active participation in these reactions. This requirement not only increases power consumption and impacts the long-term stability of the sensors but also poses a safety concerns when detecting combustible gases. Additionally, the sensitivity of sensors based on a single MOS usually shows low sensitivity. Consequently, various investigations have been performed to enhancing sensitivity, improving selectivity and reducing the operational temperature of MOS-based H_2 sensors. In this section, we present the fundamental sensing mechanisms and recent advancements in the development of MOS-based H_2 sensors, including single MOSs, heterojunction MOS nanostructures, and MOSs modified with noble metal NPs.

Fundamental sensing mechanisms for MOS-based H_2 sensors

In general, the basic mechanism underlying MOS-based sensors involves a change in current or resistance induced

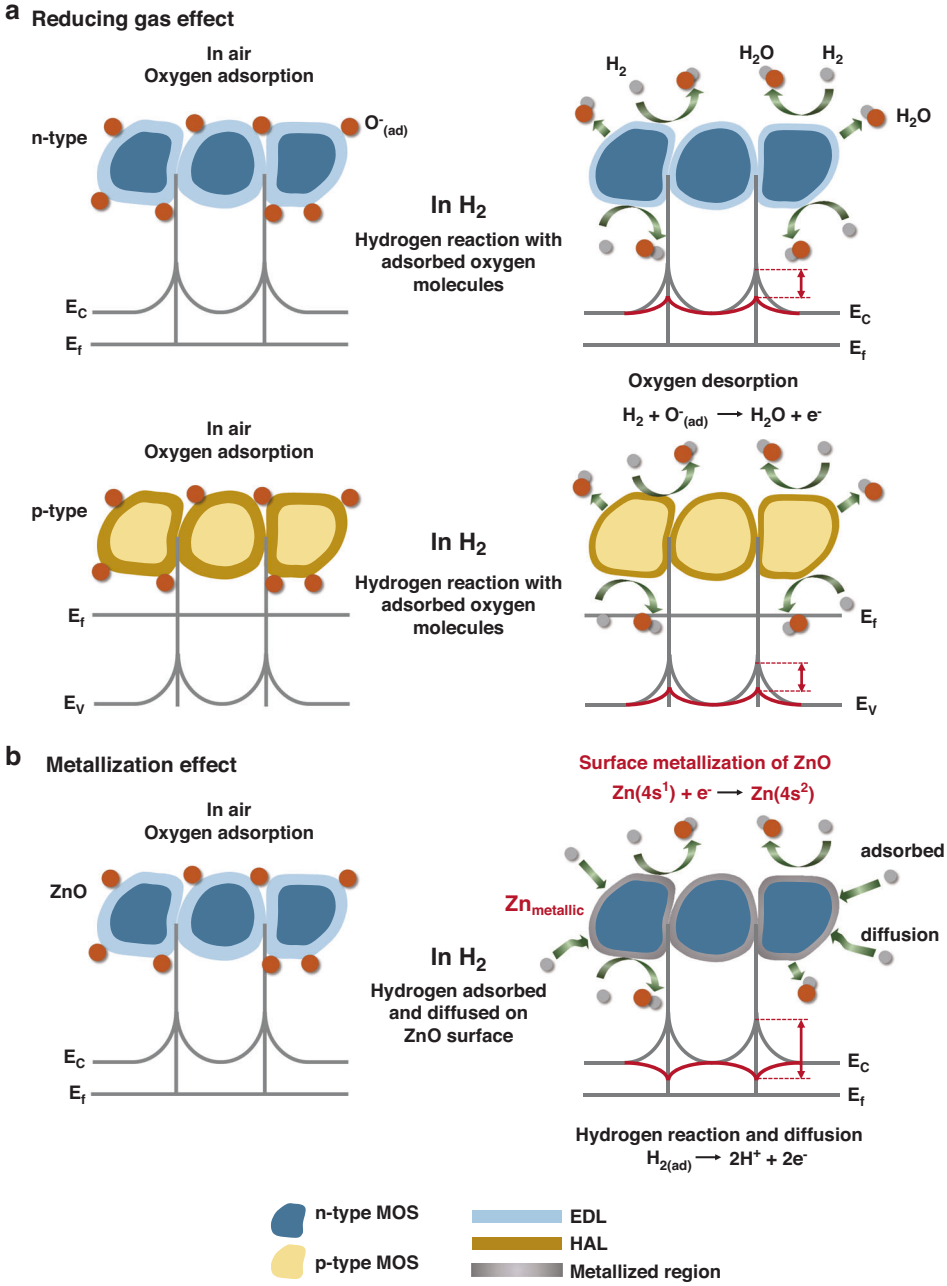

Fig. 9 Fundamental sensing mechanisms of H_2 sensor based on MOSs. Schematic representation of H_2 sensing mechanisms: **a** Reducing gas effect mechanism of n- and p-type MOSs; **b** Metallization effect mechanism of ZnO nanograins

by the interaction between H_2 and absorbed oxygen species. This process typically encompasses two key steps: (i) adsorption of O_2 to form reactive oxygen species, and (ii) subsequent reactions between these oxygen species and H_2 molecules, as shown in Fig. 9a[122,123]. The absorbed O_2 molecules serve as electron acceptors, capturing electrons from the MOSs and dissociating into different oxygen species (O_2^-, O^-, O^{2-}), which are temperature dependent[124–126]. MOSs can be categorized as either n-type or p-type MOSs based on their dominant carriers (electrons for n-type and holes for p-type semiconductors). When O_2 adsorb on the surface of n-MOSs, there is a reduction in electron density at the surface of n-MOSs, resulting in the formation of an electron depletion layer (EDL). The presence of the EDL dramatically increases the resistance of n-MOSs due to the decrease in electron density and the formation of potential barriers at grain boundaries. Upon exposure to reducing gases (e.g., H_2), H_2 reacts with oxygen

species to produce H_2O and release electrons back to n-MOSs. This reaction leads to a decrease in the width of the EDL and consequently results in a decrease in resistance. Whereas, for p-MOSs, a hole accumulation layer (HAL) is formed after absorption of oxygen species through electron extraction. As the predominant carrier of p-MOSs is hole, the resistance of p-MOS-based sensors decrease with the formation of HAL. The reaction between H_2 and adsorbed oxygen species effectively neutralizes these holes by releasing electrons, which leads to a shrinkage of HAL and increase in resistance of p-MOS-based sensors. Therefore, for both n-type and p-type MOS-based sensors, it is essential to enhance the specific surface area and elevate reactivity towards analytes to improve their sensing capabilities.

In addition to the reaction between oxygen species with H_2 molecules, certain MOSs, such as ZnO and CuO can directly react with H_2 molecules, leading to the metallization of MOSs[127–130]. As shown in Fig. 9b, the metallization mechanism of ZnO-based H_2 sensors involves the formation of a metalized region on the ZnO surface upon exposure to H_2. This process facilitates electron flow from the metallic Zn surface back to ZnO, significantly lowering the sensor's resistance and thereby improving its sensing performance. When these materials are re-exposed to air, the metalized region oxidizes and reverts back to ZnO, allowing the resistance to return to its original baseline level.

H_2 sensors based on single MOSs

Because of the advantages of low cost, stable physical and chemical properties, and the abundance of available materials, MOSs have been extensively employed in H_2 sensing. The fundamental sensing mechanism of MOSs indicates that their sensing response is greatly influenced by the reactivity of materials towards H_2 and the quantity of adsorbed oxygen species. Therefore, numerous researchers are concentrating on obtaining MOSs with high reactive facets and increasing adsorption sites of MOSs[131–135].

In terms of exposed facets, since the surface energy of various facets differs arising from distinct atomic arrangements, researchers have studied the correlation between sensing performance and exposed crystal facets of MOSs from both theoretical and experimental perspectives[131,136–139]. Zhou et al.[140] successfully tuned the exposed facets of rutile TiO_2 by varying the ethanol content in the hydrothermal solvent. Figure 10a demonstrates the XRD patterns for rutile TiO_2 prepared on fluorine-doped tin oxide (FTO) substrates. E_x is used to label the TiO_2 samples, where x denotes to the specific volume of ethanol used, such as 2, 4, 6, 8, and 10 mL. Obviously, the ratio of (002) facet increases along with the ethanol content. The sensing response values, t_{res}/t_{rec} of different TiO_2 samples are demonstrated in Fig. 10b, c. DFT simulation results reveal that H_2 preferentially adsorb and dissociate on the (002) and (101) facets of TiO_2, attributing to a low energy barrier. This phenomenon leads to improved sensitivity and rapid t_{res}. While the negligible reaction barrier for atomic H to recombine into H_2 molecules on the (110) surface of TiO_2 facilitates fast t_{rec}. Thereby, it is essential to rationally design MOSs with appropriate facet ratios to balance the sensing performance of sensors[140–142].

So as to achieve a greater number of adsorption sites, researchers typically employ the following two strategies: (i) modulation of defect concentrations[143–145] and (ii) increase of specific surface area[146,147]. To date, annealing, plasma etching, and chemical reactant treatments have emerged as three predominant approaches for adjusting defect concentrations[148–152]. Figure 10d presents a general annealing treatment to obtain SnO_2 with different concentrations of oxygen vacancies (O_V) under H_2 atmosphere by tuning the temperatures[153]. The percentage of O_V for SnO_2, SnO_2-D3, SnO_2-D4 and SnO_2-D5 are 21.11%, 22.32%, 29.47%, and 23.65%, respectively. Among these samples, SnO_2-D4 illustrates the highest sensing response toward H_2, attributed to its elevated concentration of O_V (Fig. 10e, f). This enhancement in sensitivity can be explained by the role of O_V as potential active centers for gas adsorption[154,155]. Additionally, the presence of O_V increases the electron density in the conduction band of SnO_2-D4, thereby facilitating the formation of reactive oxygen species[153,156]. Wang et al.[157] also revealed that O_V can promote the H_2 sensing performance of ZnO. Moreover, they found that both O_V and metal vacancy (M_v) may influence the H_2 sensing behavior, as the position of Fermi level (E_f) is affected by the types of existing defects. To enhance the specific surface area, in addition to reducing the dimensional size of sensing materials such as 0D quantum dots[158,159], 1D NWs/NTs[160–162], and 2D nanosheets (NSs)[163,164], designing porous structures presents as a promising strategy[165–167]. Due to their inherently high specific surface area, porous structures facilitate the migration of gases in and out more effectively than non-porous structures. Kumar et al.[129] synthesized 2D holey ZnO NSs for H_2 detection at RT by programmatically tuning the pore/hole size through annealing treatment, as shown in Fig. 10g. The density of pore in ZnO NSs consistently reduces as the annealing temperature increases from 400 °C to 800 °C. Owing to the high specific surface area and increased channels for gas diffusion and transport, the 2D holey ZnO NSs obtained at 400 °C exhibit the highest response of ~115 (20 times more than ZnO@800 sample) towards 100 ppm H_2 at RT with fast t_{res}/t_{rec} (9/6 s), as displayed

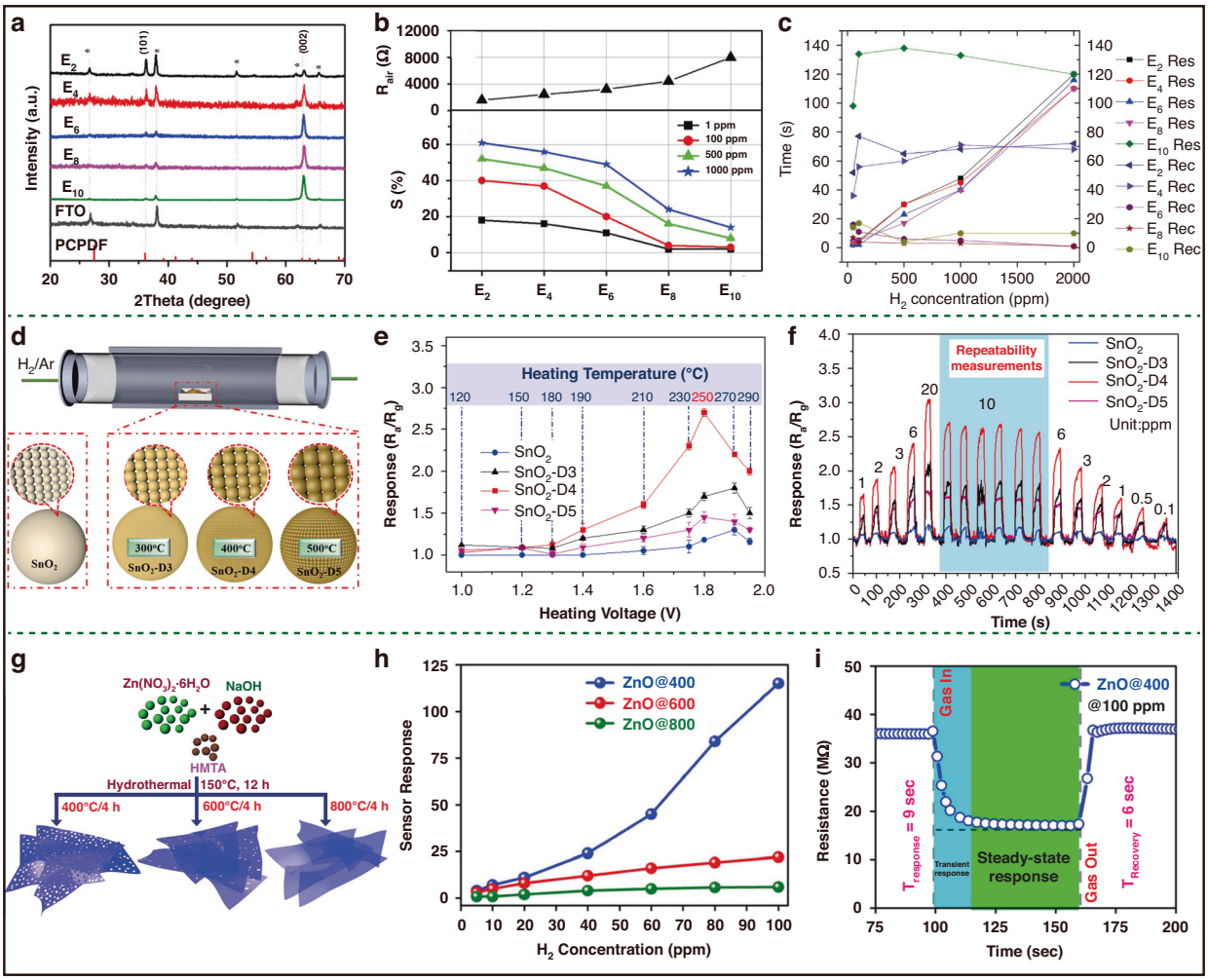

Fig. 10 Different approaches for regulating the sensing performance of pristine MOSs. a XRD patterns of TiO_2 films synthesized with different ethanol contents. * indicates the diffraction peaks from FTO substrate; **b** intrinsic resistance of four samples without H_2 and the response of four samples to different H_2 concentrations; **c** Response and recovery time of the hydrogen sensors to various H_2 concentrations[140]. Copyright 2018, American Chemical Society. **d** Schematic of the formation process of SnO_2 nanospheres and **e**, **f** the sensing performance of four sensors toward H_2[153]. Copyright 2022, Elsevier. **g** Synthesis process for 2D holey/unholey ZnO NS; **h** Linearity sensing response of holey/unholey ZnO based sensors to different H_2 concentrations and **i** The response/recovery time of optimized holey ZnO-based sensor toward 100 ppm H_2[129]. Copyright 2021, Elsevier

in Fig. 10h and i. Currently, many researchers use metal-organic-frame (MOF), such as ZIF-8, MIL-88, MIL-68, to develop porous MOSs for highly sensitive gas sensing[168–173]. He et al.[173] synthesized hexahedral hollow porous In_2O_3, which is derived from MIL-68(In), for dual gas sensing of NO_2 (at RT) and H_2 (at 160 °C).

The above-discussed H_2 sensors are primarily using n-MOSs as sensing materials because n-MOSs is more sensitive to p-MOSs. The relation between resistance and the band banding in MOSs can be expressed as $R_p = \exp(eVs/2kT)$ and $R_n = \exp(eVs/kT)$ for p-MOSs and n-MOSs, respectively[174,175]. Therefore, the response of p-MOSs is equal to the square of the response of n-MOSs ($SR_p \sim \sqrt{SR_n}$) with a similar morphology toward the same target gases[175]. Although p-MOSs based sensor is theoretically poor than n-MOSs, the p-MOSs also arouse significant attention due to their excellent catalytic effects, and less affected by humidity and high temperature. To date, some p-MOSs such as CuO[176,177], NiO[178] and Co_3O_4[179,180] have been used for H_2 sensing. Volanti et al.[177] designed various morphologies of CuO for H_2 sensing with the ability to detect 10 ppm H_2, such as urchin-shaped NPs, fibers and nanorods. Zhao et al.[176] designed a nano-patterned CuO NWs with voids for ppb-level H_2 sensing by optimizing the channel width (33 nm) as shown in Fig. 11a-c. The CuO NWs consist of small CuO grains (<10 nm) with voids were obtained by "pre-H_2 annealing" fresh Cu NWs to enhance their crystalline and form semicircular Cu NWs, and then followed by ex situ oxidizing process.

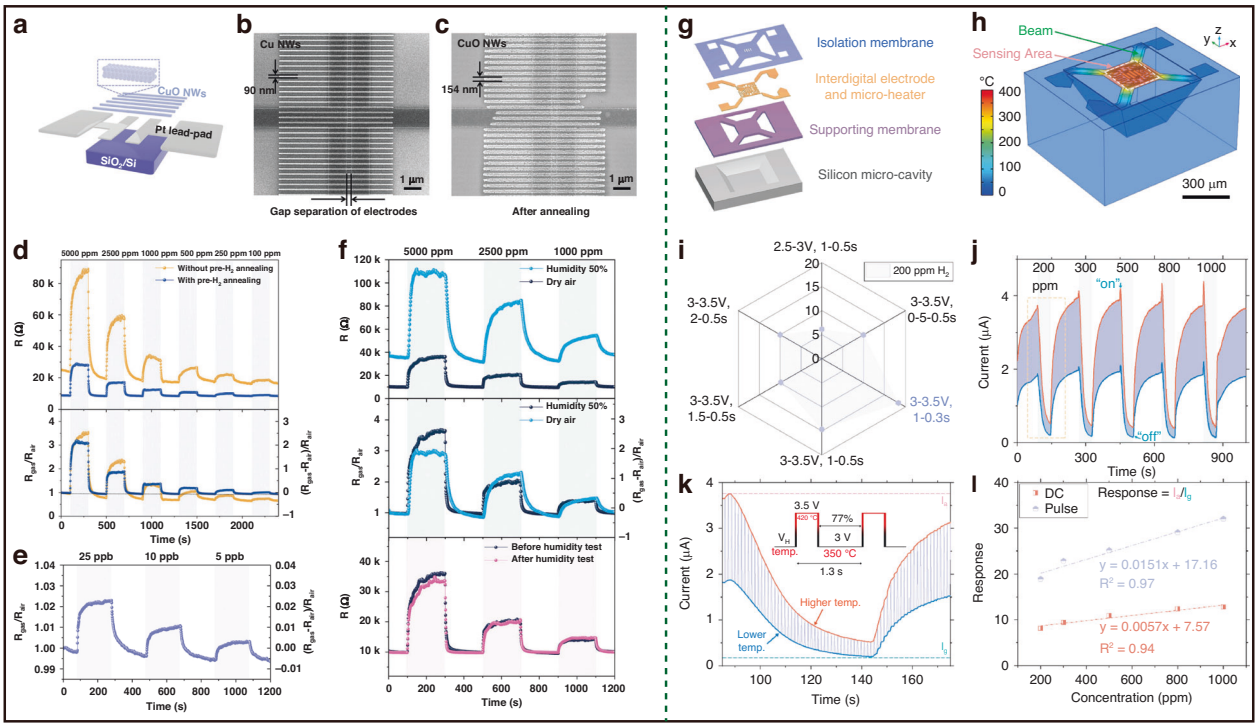

Fig. 11 The H_2 sensors based on p-type MOSs. a Schematic diagram and SEM images of Cu NWs **b** before and **c** after Ar/H_2 and dry air annealing; **d**, **e** Dynamic sensing resistance and response of CuO NW sensors toward H_2 from 5 ppb–5000 ppm; **f** Dynamic sensing response under different RH conditions[176]. Copyright 2024, John Wiley and Sons. **g** Schematic design concept and **h** surface temperature of the micro-hotplate; **i** Hydrogen sensing performance across different pulsed operation modes. **j**, **k** Transient current response to 200–1000 ppm H_2 and **l** linear gas response according to the H_2 concentrations under DC and pulsed operation[178]. Copyright 2024, Elsevier

Attributing to pre-H_2 annealing treatment, no hysteresis or baseline shift was observed (Fig. 11d). In addition, the CuO NW with voids exhibited the ability to detect 5 ppb H_2 with improved t_{res}/t_{rec} (<10 s) at 150 °C (Fig. 11e). Although the t_{res} and t_{rec} are slightly prolonged under 50% relative humidity (RH), the sensitivity to H_2 at 50% RH showed almost equal to that under dry air (Fig. 11f). The humidity tolerance of CuO is also corroborated by another research work that reported nearly constant response values under 150 °C while RH varied from 25–55%[181]. In a word, the ultralow LOD, negligible baseline drift and humidity resistance properties of CuO NWs position them as a promising candidate for trace H_2 detection under demanding conditions during the TR monitoring. While it still falls short of the US DOE standard to a certain extent when discussing the t_{res}/t_{rec} of the device. Except for solely designing of sensing materials, using pulsed heating mode (PHM) is an effective strategy for enhancing device sensitivity, selectively identifying gas species, and lowering power consumption[182,183]. Different to conventional operation mode, PHM has been rigorously explored as a power-saving strategy, minimizing the active operation time and average power consumption by applying pulse heating voltages[184,185]. Yan et al.[178] significantly enhanced the sensitivity of p-NiO sensor toward H_2 by employing PHM strategy compared with conventional DC mode (Fig. 11g and h). Moreover, based on this working mode, it enhances the extrapolation of data derived from isothermal measurements of MOS sensors. This mode can significantly enhance the device ability for discrimination multi-gases when combining with algorithms (Fig. 11i-l)[183].

To date, the sensing properties of single MOSs-based H_2 sensors, such as sensitivity and t_{res}/t_{rec}, could be improved through facet engineering, porosity design, as well as vacancy regulation. However, many reported single MOSs exhibit a low response ratio of H_2 to its strongest interferent, affecting the accuracy of detection under TR conditions with complex gas mixture[44]. This cross-sensitivity of single MOSs hinders their further advancements. Consequently, it is essential to investigate and design new functional MOSs materials to enhance the sensitivity, selectivity, and t_{res}/t_{rec} of H_2 sensors. The subsequent sections will provide a detailed discussion on heteroatom doping, construction of heterojunction, fabrication of ternary or quaternary MOSs, and decoration MOSs with metals.

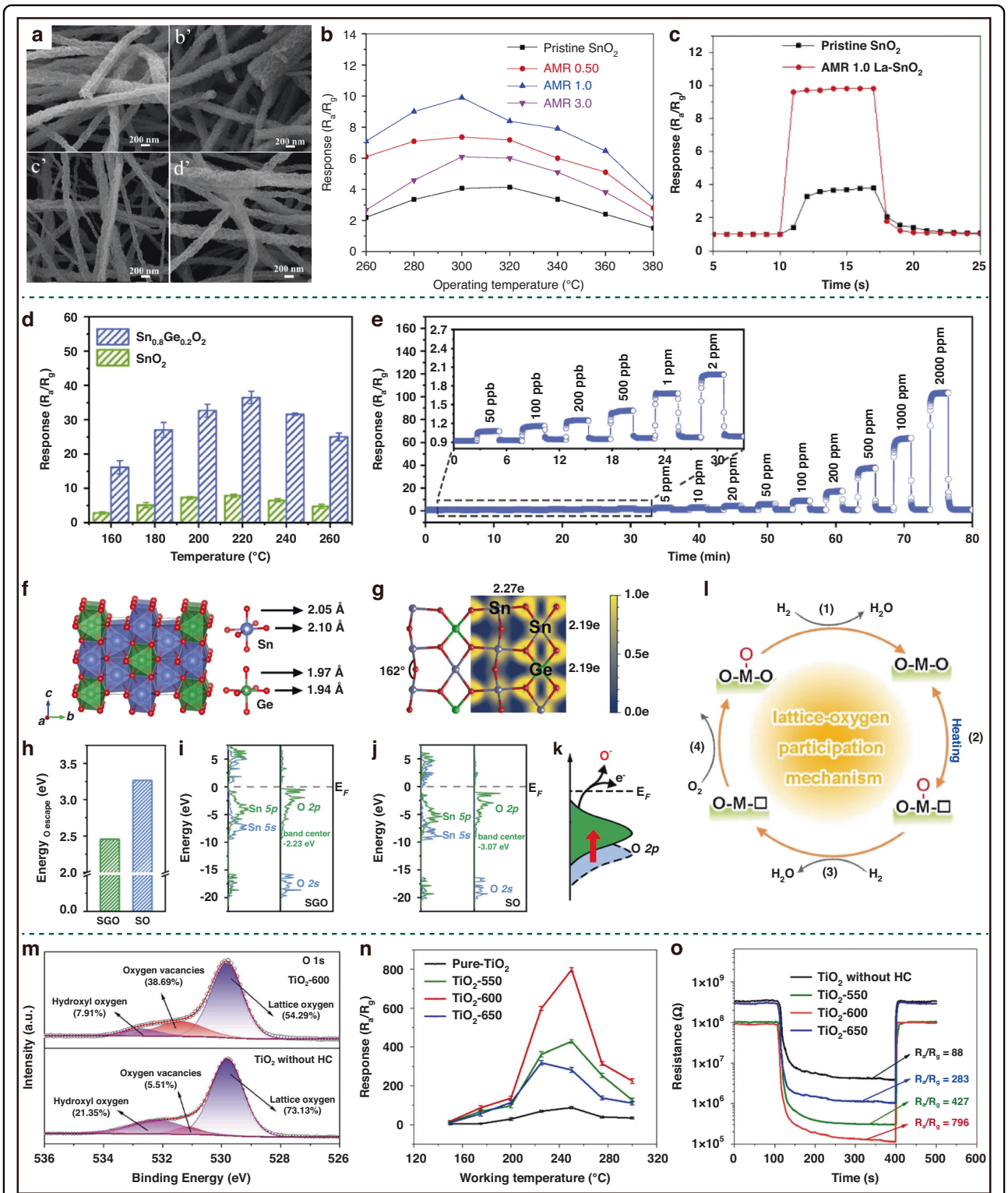

Fig. 12 (See legend on next page.)

(see figure on previous page)
Fig. 12 The enhanced sensitivity of MOSs based H_2 sensors via heteroatom. a SEM images of the SnO_2 and La-doped SnO_2 NFs; **b** Temperature-dependent response of SnO_2 and La-doped SnO_2 NFs to 100 ppm H_2 and **C** dynamic sensing response of SnO_2 and La-doped SnO_2 NFs to different H_2 concentrations[194]. Copyright 2019, Elsevier. **d** Response of sensors based on SnO_2 and Ga-doped SnO_2 (SGO) to 500 ppm H_2 at different temperatures and **e** real-time sensing response of SGO to various H_2 concentrations; **f** Schematic crystal structure and **g** electron local function and the bader charge of SGO; **h** Escape energy of O atoms in SGO and SnO_2; The electronic density of states of **I** SGO and **j** SnO_2; **k** the relationship between the position of O p-band and the conversion from surface lattice oxygen to chemisorbed oxygen; **l** Schematic diagram of the mechanism of the gas-sensing reaction with lattice oxygen participation[187]. Copyright 2024, Springer Nature. **m** O 1s of TiO_2-600 and TiO_2 without HC; **n** Response of four sensor at different temperatures toward 1000 ppm H_2; **o** Dynamic response-recovery curves of four sensors at 250 °C toward 1000 ppm[200]. Copyright 2025, Elsevier

Hetero MOS-based H_2 sensor

To achieve enhanced H_2 sensing performance in MOSs, several strategies have been performed, including heteroatom doping[186], the construction of heterojunction, and the fabrication of ternary or quaternary MOSs.

Doping is an effective method for improving the sensing performance of MOS through modulating their electronic structure and influencing their physicochemical properties such as bandgap, conductivity, and defect concentration[187–191]. For instance, after doping of Mn into Fe_2O_3 lattice, it weakens the bonding between neighboring oxygen ions, leading to the release of oxygen ions and the formation of O_V[186]. Kim et al.[188] reported that the percentage of O_V increased from 26.42% to 33.58% by doping 3% Cu^{2+} into the SnO_2 lattice, and the sensitivity of the sensor increased from 0.241%/ppm to 0.286%/ppm. Catalytic La^{3+}, which facilitates fast dissociative adsorption of H_2 through polaron effect[192,193], was selected to dope SnO_2 nanofibers (NFs) with varying atomic ratios (At%) relative to Sn (0%, 0.5%, 1.0%, and 3%) via electrospinning and calcination. Figure 12a shows the SEM images of the fabricated four La-SnO_2 samples[194]. The response value of 1% La-SnO_2 NFs for H_2 detection is 9.9 towards 100 ppm H_2 at 300 °C, which present an enhancement of 2.5 times and 1.6 times compared to pure SnO_2 and 3% La-SnO_2 NFs, respectively (Fig. 12b). When the At. % of La reaches a high level (≥3%), La^{3+} ions are expelled from the SnO_2 NFs, leading to the formation of a p-n junction between n-type SnO_2 and p-type La_2O_3. This p-n heterojunction significantly contributes to the enhanced sensing mechanism. In contrast, when the At. % of La is low, La^{3+} ions are incorporated into the SnO_2 crystal lattice by replacing the Sn sites, resulting in partial p-type doping regions within the SnO_2. The area occupied by these p-type doping regions undergoes expansion upon exposure to air and shrinkage when exposed to H_2. Owing to the abundant pores present in the La- SnO_2 NF film, H_2 can easily penetrate into/depart from the entire sensing film. This contributes to rapid t_{res}/t_{rec} (~1 s), which is approaching the detection speed set by US DOE as shown in Fig. 12c. In addition, Li et al.[187] revealed that the dopants can also enhance the reactivity of surface lattice oxygen (O_L) in MOSs. The H_2 sensing response of $Sn_{0.8}Ge_{0.2}O_2$ (SGO) significantly surpasses that of pure SnO_2, with the LOD reaching as low as 50 ppb, as illustrated in Fig. 12d and e. According to the DFT calculations, the introduction of Ge induces lattice distortion, which in turn results in an increased concentration of O_V (Fig. 12f). Specifically, compared to pure SnO_2, the length of the Sn-O bond in SGO along both the a-axis and b-axis is elongated from 2.08 Å to 2.10 Å, while the length along the c-axis is changed to 2.05 Å. When viewed from the (110) direction, the bond angle of Sn-O-Sn changes from 180 ° to 162 °, thereby altering the electronic structure of SGO (Fig. 12g). Moreover, the oxygen escape energy in SGO is dramatically lower than that in SnO_2 (2.45 eV vs 3.26 eV). This finding implies that the O_L in SGO transitions more readily into chemisorbed oxygen species compared to its counterpart in SnO_2, as depicted in Fig. 12h. This difference is primarily derived from the variations in the positions of O 2p orbitals between these two samples, and a higher O 2p-band center (relative to E_f) thermodynamically facilitates the transformation from O_V into chemisorbed oxygen species (Fig. 12i-k). Since the SGO exhibits a comparable or even higher H_2 response value in Ar, this further provides experimental evidence for the involvement of O_L in H_2 sensing[45,187,195]. Thus, the H_2 sensing mechanism of SGO-based sensors involves a four-step process (Fig. 12i): (i) H_2 molecules react with adsorbed oxygen species; (ii) surface O_L transforms into chemisorbed oxygen species and generates O_V; (iii) newly generated chemisorbed oxygen species continue to react with H_2 molecules; and (iv) upon exchange to air, the O_2 molecules adsorb on the surface of SOG and undergo conversion back into surface O_L and chemically adsorbed oxygen. Furthermore, some nonmetal elements such as C, N, S and Si are often utilized as doping heteroatoms to enhance gas sensing response[196–199]. Li et al.[200] used waste honeycomb (HC) as a bio-template to fabricate N-doped TiO_2 with a hierarchical porous nanostructure for rapid and selective H_2 detection. In comparison to pure TiO_2 synthesized without HCs, the obtained N-TiO_2, which was calcinated under 600 °C, exhibited a higher concentration of O_V (Fig. 12m). Beneficial from the introduction of active sites, the sensor based on N-TiO_2-600 demonstrated a high

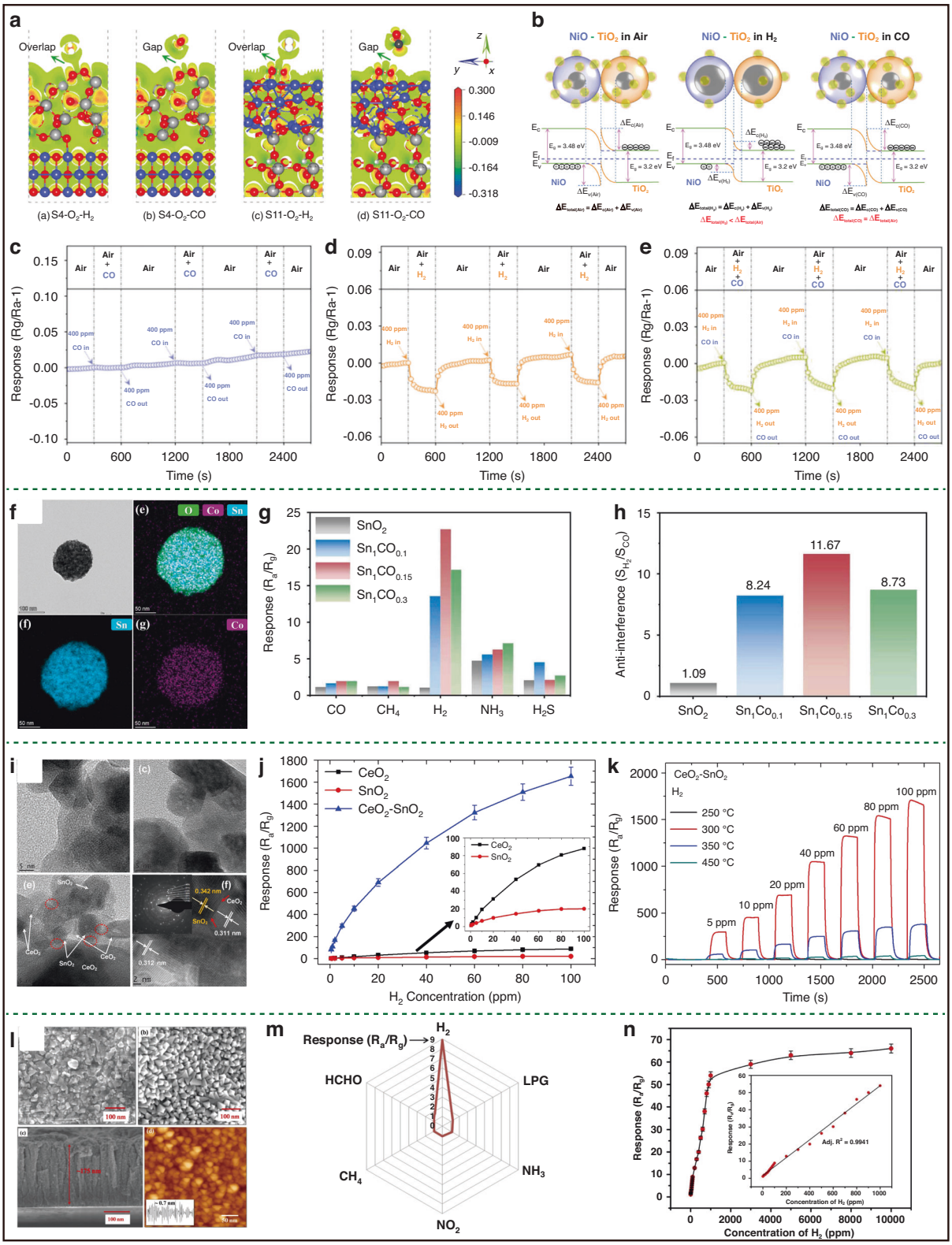

Fig. 13 (See legend on next page.)

(see figure on previous page)
Fig. 13 The influence of MOS heterojunction design on H_2 sensor selectivity. a Differential charge density of NiO/TiO_2 and TiO_2/NiO heterojunctions after absorption of O_2-H_2 and O_2-CO; **b** Gas selectivity mechanism of the NiO-TiO_2 heterojunction in the presence of Air, H_2, and CO; **c** cycle response curves of NiO/TiO_2 to 400 ppm of CO, H_2, and the mixture of H_2 and CO[207]. Copyright 2023, American Chemical Society. **f** TEM images of SnO_2-Co_3O_4 nanocomposite; **g**, **h** Gas selectivity of four samples to different gases at 325 °C[201]. Copyright 2025, Elsevier. **I** TEM images of SnO_2, CeO_2, and SnO_2-CeO_2; **j** Response curves of the CeO_2, SnO_2, CeO_2-SnO_2 exposed to different concentrations of H_2 at 300 °C; **b** dynamic response curves of CeO_2-SnO_2 sensor to various H_2 concentrations at different temperatures[212]. Copyright 2018, Elsevier. **I** SEM and AFM images of $AgInO_2$ thin film; **m** Selectivity of $AgInO_2$ thin film towards 100 ppm of various gases at 360 °C; **n** Calibration plot of $AgInO_2$ thin film towards different concentrations of H_2 at 360 °C[213]. Copyright 2023, Elsevier

response, rapid t_{res}/t_{rec} (8/3.8 s) at 250 °C for 1000 ppm H_2, as illustrated in Fig. 12n, o.

The construction of heterojunctions by incorporating two or three types of MOSs is one of the most important strategies for enhancing sensor performance, such as selectivity and sensitivity. Heterojunctions can modulate the charge distribution and electronic structure of the host material, thereby further optimizing sensor performance via both tuning the resistance value and adjusting the concentration of adsorbed oxygen species. Upon establishing heterojunction interfaces, the E_f of two components equilibrate at the interface, resulting in electron transfer from the component with a higher E_f to that with a lower E_f. This process leads to the formation of an EDL. The increased interfacial potential barrier energy and synergistic surface reactions greatly contribute to improvements of sensing performance. In general, the heterojunctions can be classified into p-n, n-n, and p-p junctions, as well as complex heterojunctions (e.g., n-p-n, p-n-p), depending on the types of MOSs employed. Among these classifications, the construction of p-n heterojunctions has emerged as a widely used strategy for selective detection of H_2, such as n-SnO_2/p-Co_3O_4[201,202], n-In_2O_3/p-Co_3O_4[203], n-WO_3/p-PdO[204,205], n-WO_3/p-CoO[206], n-TiO_2/p-NiO[207], and n-SnO_2/p-Cr_2O_3[208]. During the industrial H_2 production and TR process, CO not only serves as the interfering gas but also possesses similar chemical properties with H_2. Consequently, many researchers have aimed at enhancing the selectivity for H_2 in the presence of CO interference[201,208,209]. In the realm of gas sensing, the adsorption energy (E_{ads}) is an essential index for evaluating the selectivity of the sensor. Thereby, the NiO (100) site supported TiO_2 (101) exhibits a good selectivity to H_2 since its E_{ads} to H_2 (−0.377 eV) is much more negative than CO (−0.022 eV) (Fig. 13a-e)[207]. The change in the heterojunction energy barrier after interaction with H_2 ($\Delta E_{total(H_2)}$) is significantly lower than that of $\Delta E_{total(O_2)}$, while $\Delta E_{total(CO)}$ remains nearly equivalent to $\Delta E_{total(O_2)}$ (Fig. 13b). Consequently, the TiO_2-NiO heterojunction exhibits an n-type sensing response to H_2 and exhibits no response to CO (Fig. 13c-e). Similarly, since the E_{ads} of H_2 (−2.38 eV) is more negative than that of CO (−1.9 eV) on the surface of n-SnO_2/p-Co_3O_4 composites, resulting to an outstanding anti-interference with an impressive H_2 to CO response ratio (SH_2/S_{CO}) of 11.67 (Fig. 13f-h)[201]. Additionally, both p-p and n-n heterojunctions also possess the capability to modulate the barrier energy at their heterointerface, several H_2 sensors with enhanced sensing response have been reported by using the MOSs with the same semiconductor type[210–212]. Motaung et al.[212] reported a highly sensitive H_2 sensor based on CeO_2-SnO_2 n-n heterojunctions, as illustrated in Fig. 13i-k. The response value of the n-n heterojunction is significantly higher than that of pure CeO_2 and pure SnO_2 owing to the presence of a large number of defects induced by heterojunctions. Moreover, instead of confining the search domain to construction of heterojunctions, the fabrication of ternary MOSs (TMOSs) represents a promising strategy for enhancing sensor performance[213,214]. Further, numerous reports have demonstrated that TMOSs-based sensors exhibit superior sensing performance compared to binary MOSs. Owing to the presence of two differently sized cations in TMOSs with multiple oxidation states, these TMOSs are endowed with a higher density of interstitial defects and O_V, and a stronger surface adsorption of atmospheric oxygen. This ultimately leads to enhanced gas sensing performance. Figure 13l displays the SEM and AFM images of $AgInO_2$ film, which is deposited at RT for the first time[213]. The $AgInO_2$-based sensor exhibited high sensitivity and excellent selectivity toward H_2, achieving an impressive ratio of H_2 to NH_3 response ratio (SH_2/SNH_3) of ~7.5, as displayed in Fig. 13m, n.

Rational design of MOS heterostructures demonstrates enhanced sensitivity, excellent selectivity, ppb level LOD, and acceptable t_{res}/t_{rec} for H_2 sensors, making them suitable for detection of trace H_2 in early stage of TR. Moreover, since p-MOSs have a higher tolerance toward humidity than n-MOSs, it is possible to design humidity-resistance H_2 sensor for practical monitoring LIB safety by optimizing the p-n or p-p MOS heterostructures[181,203].

H_2 sensors based on noble metal decorated MOSs

Noble metals are widely recognized for their exceptional catalytic properties. They can effectively reduce the E_{ads} of gases on the surface of sensing materials, thereby enhancing their performance. Additionally, the modification of

MOSs with noble metal such as Pt, Pd and Au introduces more active sites on the MOSs surface, facilitating the preferential adsorption of target gases[215–217]. Furthermore, due to their inherent catalytic characteristics, noble metals provide reaction pathways for H_2 dissociation, which can lower the activation energy and subsequently enhance the response speed, sensitivity, selectivity and reliability of the sensors[218]

Moreover, the noble metals also create spillover effect in H_2 sensing when deposited on the surface of MOSs. For instance, in the context of H_2 sensing, the spillover effect refers to a process where H_2 molecules absorb onto the surface of noble metals and are subsequently dissociate into H atoms. To elucidate the mechanism underlying this spillover reaction, operando techniques are employed to reveal the dynamic reaction process, such as in-situ Raman[219], in-situ infrared spectroscopy (IR)[220], in-situ electron energy loss spectroscopy[220,221], and in-situ X-ray photoelectron spectroscopy (*XPS*)[222,223]. Li et al.[223] used Pt-γ-WO_3 as a model sample and employed near ambient pressure XPS (NAP XPS), DFT calculations, and micro-kinetic model to study the dynamic evolution of surface states, during H_2 sensing, as illustrated in Fig. 14a, b. The activation barrier height (E_a) of H_2 dissociation on the surface of Pt-γ-WO_3 is much lower than that on the surface of pure WO_3. As a result, H_2 preferentially dissociates on the surface of Pt-γ-WO_3. W 4f and O 1s spectra from Pt-γ-WO_3 were collected at RT under 5 mTorr H_2 gas (Fig. 14b). The NAP XPS analysis demonstrated several dynamic changes when exposed to H_2, including the presence of W^{5+}, the formation of adsorbed water (H_2O_{ads}), and an increase in undercoordinated oxygen species, revealing that H_2 spillover through proton-coupled electron transfer. By studying the effect of temperature via NAP XPS and theoretical calculations, Li et al.[223] concluded that H_2 spillover involves multiple pathways after dissociation into H atoms on the surface of Pt: (I) at low temperatures (25–50 °C), H inserts into the bulk oxide lattice (H_{bulk}); (II) reverse H spillover is observed when the temperature increases to 50–150 °C; and (III) an accumulation of O_V is detected due to the facilitation of H_2O_{ads} desorption with further increases in temperature (150–400 °C) (Fig. 14c). Thus, the incorporation of noble metals reduces the reaction activation energy of MOSs, leading to faster t_{res}/t_{rec} and lower operation temperature[224–226]. Meng et al.[227] reported that the operation temperature of SnO_2 decreased from 300 °C to 125 °C after Pd loading. Figure 14d demonstrates the TEM image of Pd/SnO_2. Figure 14e shows that the sensing response of 0.5 at% Pd/SnO_2 to 5000 ppm achieved a value of 2727, which is approximately 47.15 times greater than that of SnO_2. Figure 14f, g presents a RT H_2 sensor based on Pd/PdO_2 composites that achieves detection of 4% H_2 within ~1 s ascribing to the rapid reduction kinetics associated with PdO_2[228]. The fabrication of Pd/PdO_x composites was conducted via an electrophoretic deposition method, during which the Pd^0 content gradually decreased from 43% to 29% as the electrode potential increased from 1 to 10 V. The presence of metallic Pd allows rapid dissociation of H_2 into adsorbed H atoms and coupled with ultrafast reduction kinetics of PdO_x, enabling 1 s detection of 4% H_2 at RT. However, it is important to note that since the reduction process for PdO_x is irreversible at RT, the Pd/PdO_x composites do not recover after exposure to H_2. In recent years, to further improve the catalytic effect of noble metals, atomically dispersed single-atom catalysts (SACs) have been proposed to maximize the exposure of metal atoms and enhance their utilization efficiency[229,230]. To highlight the unique role of SACs, the sensing performance of Pd SA/Co_3O_4 and Pd NPs/Co_3O_4 were studied to provide a deeper insight and understanding of the effect of Pd SACs (Fig. 14h-j)[231]. Different concentrations of Pd SAs were obtained by increasing the at% of Pd/Co from 1 to 5%. The sensing response of Pd/Co_3O_4 to H_2 gradually increased with rising concentrations of Pd SAs (1–5% Pd). As the Pd/Co ratio was further increased (7.5–20% Pd), Pd NPs formed due to the aggregation process and the response value of sensor subsequently decreased. Because all of the Pd SAs can serve as electron doners compared with Pd NPs to sensitize the sensor performance. However, the high surface energy of SACs presents a significant challenge in fabrication of SACs on sensing materials with high stability[232]. Thus, defect engineering has been proposed as a strategy to stabilize SAs, given that both the unsaturated coordination conditions and the high diffusion barrier at the defects can facilitate anchoring of SAs[233,234]. By construction of O_V, Pt SAs were steadily anchored on the surface of Fe_2O_3 NSs. enabling ultrafast H_2 sensing (t_{res} = ~2 s), as shown in Fig. 14k-n[235]. According to DFT results, Pt SAs are positioned in the vacancy position sites and coordinated with the adjacent Fe atoms. The Pt-Fe spacing in the Pt-Fe_2O_3-O_V is smaller than that in Pt-Fe_2O_3, indicating enhanced stability of the former structure (Fig. 14l). Consequently, the attenuation rate of the sensor based on Pt-Fe_2O_3-O_V was merely 7.5% over a testing period of 30 days, significantly lower than the 15.1% observed in the Pt-Fe_2O_3-based sensor (Fig. 14n). In addition, owing to the lower E_{ads} of H_2 on the surface of Pt-Fe_2O_3-O_V, this configuration demonstrates higher sensitivity towards H_2 while maintaining improved stability. At the device level, Guo et al.[236] developed Pd-catalyzed dual-gate TeSeO FET H_2 sensors, achieving a theoretical LOD of 35 ppb. The dual-gate modulation offers practical strategies for the rational design of high-performance H_2 sensors based on noble metal-decorated MOSs.

To further enhance the sensing performance of noble metal-modified MOSs, researchers preferentially design

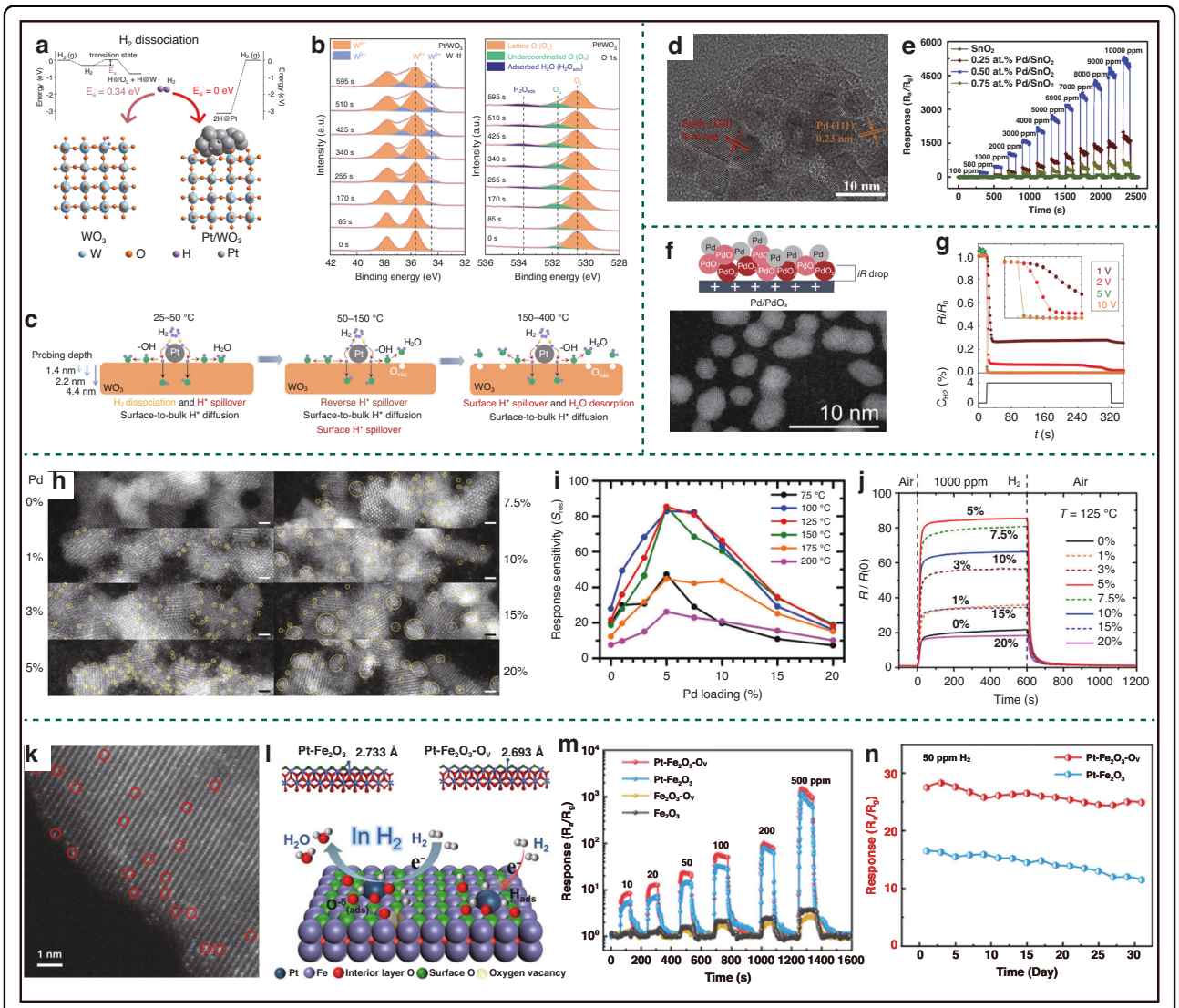

Fig. 14 Noble metal mechanisms for enhanced H_2 sensing in MOS devices. a Schematic H_2 dissociation on the monoclinic WO_3 (001) surface w/ wo Pt metal cluster based on DFT results; **b** Operando monitoring of H_2 spillover on WO_3 surface at RT using NAP XPS; **c** Schematic illustration of the reaction mechanism at varied temperatures[223]. Copyright 2025, American Chemical Society. **d** TEM image of 0.5 at.% Pd/SnO_2 NPs and **e** the dynamic response curves of the SnO_2 sensors with various Pd concentration ratios exposure to 100-10000 ppm H_2[227]. Copyright 2022, Elsevier. **f** Schematic preparation of Pd/PdO_x sensors by electrophoretic deposition and the SEM image of prepared Pd/PdO_x; **g** Dynamic sensing curves of Pd/PdO_x prepared under different voltages to 4% H_2[228]. Copyright 2023, Spring Nature. **h** STEM images of Co_3O_4 and Pd/Co_3O_4 with different Pd contents; **i**, **j** Hydrogen sensing properties of NP films of Co_3O_4 and Pd-Co_3O_4 with Pd contents of 1–20%[231]. Copyright 2020, American Chemical Society. **l** STEM image of Pt-Fe_2O_3-O_V nanosheet; **m** DFT simulations of Pt-Fe_2O_3 and Pt-Fe_2O_3-O_V after adsorption of H_2 molecules; **m** Dynamic sensing curves and **n** long-term stability of sensors to H_2[235]. Copyright 2024, American Chemical Society

more complicated sensing materials by introducing bimetallic catalysts or constructing ternary heterojunctions[237–240]. Bimetallic catalysts exhibit superior catalytic performance compared to their monometallic counterparts, primarily due to their synergistic effects. For instance, since Pd demonstrates excellent reactivity and durability to H_2 and Pt exhibits outstanding catalyst effect for both hydrogenation and oxygen reaction, PdPt bimetallic NPs are usually utilized for highly sensitive H_2 detection[241,242]. Zhou et al.[243] reported a humidity immunity H_2 sensor based on PdRh-sensitized Fe_2O_3, the sensing response of PdRh/Fe_2O_3 (105.9) to 10 ppm H_2 at 230 °C is significantly higher than that of Fe_2O_3 (36.3), Rh/Fe_2O_3 (64), and Pd/Fe_2O_3 (89.4). The enhancement mechanism can be attributed to the fact that Pd promotes the adsorption and dissociation of H_2, while Rh improves the dissociation of adsorbed O_2. To date various bimetallic catalysts have been reported in MOS-based H_2 sensor such as PdCo[244], PdPt[245], PdAu[246,247], PdRu[243], PdAg[248], NiPt[249], AgCu[250], AuSn[251], and so on. However,

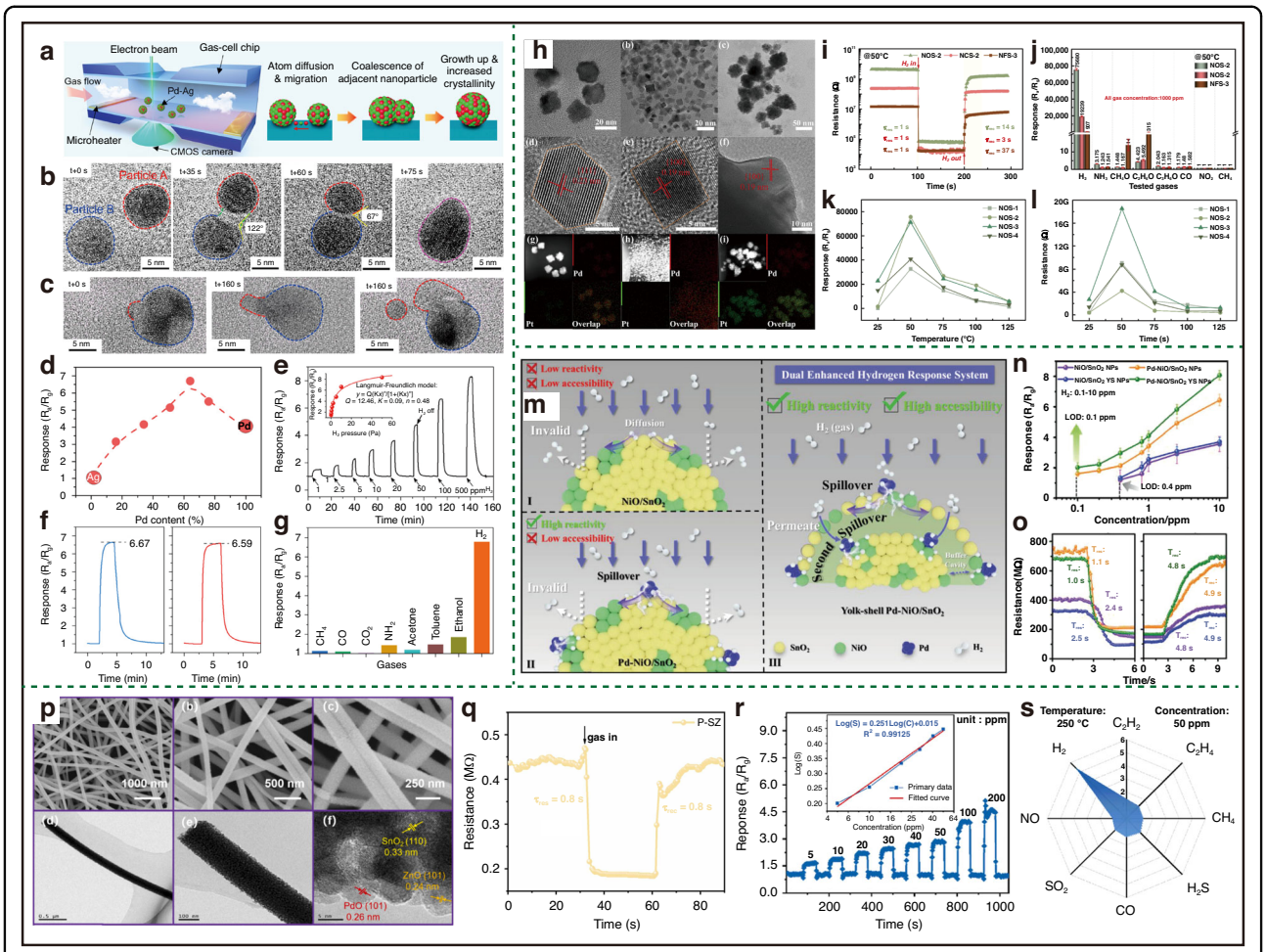

Fig. 15 High performance MOS based H_2 sensors via bimetallic catalyst modification or construction of ternary heterojunctions. **a** Schematic showing the coalescence sintering of PdAg NPs under the gas cell; Morphological evolution of PdAg NPs **b** at 300 °C and **c** at 500 °C in air; **d–g** Sensing results of the ZnO-based H_2 sensor with PdAg NPs as the catalyst[248]. Copyright 2022, American Chemical Society. **h** TEM and EDS mapping images of PdPt NPs with different shapes and exposure facets; **i–l** Sensing results of the PdPt/SnO_2-based sensors[253]. Copyright 2023, Elsevier. **m** Schematic diagram of hollow nanoreactor driven kinetics; **n**, **o** Dynamic sensing results of four samples such as NiO/SnO_2 NPs, Pd-NiO/SnO_2 NPs, NiO/SnO_2 YS NPs, and Pd-NiO/SnO_2 YS NPs[254]. Copyright 2023, John Wiley and Sons. **p** SEM and TEM images of Pd-SnO_2/ZnO nanofibers; **q–s** Sensing results of Pd-SnO_2/ZnO-based H_2 sensors[256]. Copyright 2024, Elsevier

MOS-based sensors typically operate at high temperatures, which greatly compromises their stability due to the deactivation or deterioration of noble NPs[252]. To investigate the stability mechanism underlying noble metal catalysts, in-situ TEM is employed to capture the dynamic evolution of PdAg NPs under operational conditions, as illustrated in Fig. 15a-c[248]. Based on in-situ TEM observations, two failure mechanisms have been identified: coalescence of PdAg NPs at 300 °C and phase segregation at 500 °C. At 300 °C, a decrease in centroid-to-centroid distance between two adjacent NPs is noted, accompanied by atom migration until two NPs merge into a larger NP (Fig. 15b). When the operation temperature increases to 500 °C, the Ag preferentially segregates from the alloy phase due to its lower Tamman temperature (~345 °C) compared to Pd (640 °C) (Fig. 15c). To avoid particle coalescence and phase segregation, it is essential to maintain a low density of PdAg NPs on the surface of ZnO, with an operational temperature kept below the Tamman temperature of Ag. Furthermore, the elemental ratios of Pd/Ag must also be taken into account to optimize sensing performance. Therefore, the optimized PdAg/ZnO-based sensor demonstrates a high sensing response along with satisfactory long-term stability, as shown in Fig. 15d-g. Similar to MOS-based sensors with different exposed facts, the noble NPs with different exposed facets can also significantly influence sensor sensitivity. Meng et al.[253] fabricated a series of PdPt/SnO_2-based H_2 sensors as shown in Fig. 15h. The sensing results illustrate that both the exposed facts of PdPt NPs

and their content ratios have a considerable influence on sensor performance (Fig. 15i-l). The PdPt nano-octahedrons (NOs) modified SnO_2-based sensor shows the highest sensing response owing to the higher catalytic of (111) facet. As discussed above, both construction of MOSs heterojunctions and the decoration of MOSs with noble metals are two efficient strategies to promote the sensor performance. Therefore, researchers are committed to integrating these strategies together to fabricate ternary heterojunctions for H_2 sensing[239,240,254]. Hu et al.[255] reported a remarkably enhancement in sensing response toward H_2 by employing ternary heterojunction as the response order is Pd/ZnO-SnO_2 > ZnO-SnO_2 > SnO_2. Cai et al.[254] presented a highly sensitive H_2 sensor based on Pd-NiO/SnO_2 with fast t_{res}/t_{rec} (1/4.9 s) to 1 ppm H_2. The improved sensing performance is mainly due to (I) the hollow NiO/SnO_2 heterojunction provides sufficient reactive sites; (II) kinetically promoted H_2 spillover effect by Pd NPs (Fig. 15m-o). Although sub-second t_{res} has been achieved in aforementioned works, the realization of comparably fast t_{rec} remains challenging. Xing et al.[256] addressed this issue by developing a Pd-SnO_2/ZnO-based sensor that exhibits ultrafast recovery kinetics (Fig. 15p). The rapid sensing mechanism relies on redox reaction acceleration, catalytic promotion by noble metals, and synergistic heterojunction effects among PdO, SnO_2, and ZnO. The sensor demonstrates notable performance in sensitivity and selectivity, combined with sub-second t_{res}/t_{rec} of 0.8/0.8 s toward 50 ppm H_2, surpassing most reported H_2 sensors with similar structural configurations (Fig. 15q-s).

Therefore, these results confirm the effectiveness of constructing noble metal-modified MOSs could further enhance the overall sensor performance specifically sensitivity and t_{res}/t_{rec} (within 1 s) to fulfill the US DOE standard. We anticipate that the already impressive performance could be further enhanced, particularly in terms of reliability via material-level optimizations discussed in prior Sections "H_2 sensors based on single MOSs" and "Hetero MOS-based H_2 sensor".

Table 3 displayed sensing properties of MOS-based H_2 sensors. To summarize, MOS-based H_2 sensors not only exhibit ultrahigh H_2 response with a low LOD but also have demonstrate high thermal and chemical stability. However, the majority of MOS-based sensors operate at elevated temperatures (over 200 °C) to facilitate H_2 reactions with chemisorbed oxygen species or the MOSs themselves. To lower the energy consumption, decoration of MOSs with noble metals and employing PHM method have been reported as effective strategies to lower the energy consumption. The other strategy is to employing materials with the capability to detect gases at RT such as carbon materials and 2D materials as discussed in the following sections.

Carbon material-based chemiresistive H_2 sensor

H_2 sensors based on pure carbon materials

Carbon-based materials have garnered significant attention as promising candidates for chemiresistive gas sensors due to their high specific surface area and tunable electrical properties[257–259]. Carbon nanomaterials exhibit a wide range of structures (e.g., 0D nanodiamonds (NDs) and active nanocarbon NPs, 1D CNTs, 2D graphene (Gr) and graphdiyne (GDY), as well as 3D fullerenes) that arise from different bonding configurations such as sp, sp^2, or sp^3 hybrid orbitals[260]. For sensors based on pure carbon materials, changes in the resistance of carbon materials can be measured, contributing to the electron transfer once exposed to target gases, as shown in Fig. 16. In inert atmospheres, H_2 directly donates electrons when adsorbed onto the surface of carbon materials. This causes a decrease/increase in resistance for n-type/p-type carbon materials[261]. In air, H_2 reacts with oxygen species adsorbed on the surface of carbon materials and releases electrons into the conduction band of these materials, leading to variations in resistance. However, pristine carbon materials suffer from poor H_2 sensitivity due to weak adsorption of H_2 molecules on material surface[262–265]. To activate sensing properties, several strategies have been employed, including increasing adsorption sites and utilization of external heat or light energy[266].

Construction of porous sensing materials is an effective strategy to provide more active adsorption sites[267]. Guo et al.[268] modulated the density of CNT to enhance H_2 accessibility to the underlying active sites of porous CNT films, which optimized H_2 sensing performance. Besides, the application of carbon materials with inherent abundant adsorption sites, can enhance the gas sensing performance as well. For instance, N-doped nanodiamonds (N-NGs), consisting disordered carbon with sp^2/sp^3 bonds, possess plenty of grain boundaries and defects, can enhance H_2 sensing response when combined with other carbon materials[264,269–271]. In addition, 2D porous carbon material-GDY, has aroused attention in gas sensing application[272–275] owing to its uniform nanopore structure and highly reactive triple bonds, which exhibits excellent electron capture capability[276,277]. Nam et al.[278] reported a H_2 sensor based on hydrogen-substituted GDY (HsGDY) with rapid and reversible H_2 sensing. Figure 17a depicts the schematic diagram of HsGDY structure and its synthetic route. Different from other 2D materials such as Gr, transition metal dichalcogenides (TMDs), and MXenes, the HsGDY with uniform 1.63 Å nanopores facilitate the diffusion of target molecules through these pores, thereby providing a significantly accelerated reaction pathway. Additionally, sp carbon in alkynyl linkage can serve as an effective binding site for the molecules. The HsGDY-based H_2 sensor showed a wide detection range (0.1–10,000 ppm) with good reproducibility ($n = 3$

Table 3 Summary of sensing properties of MOS-based H_2 sensors

Material	*T* (°C)	detection range (ppm)	Tested concentration (ppm)	Response	t_{res} /t_{rec} (s)	Tested LOD (ppm)	Ref.
ZnO inverse opals	200	7.5–200	7.5	121%[a]	NG/NG	7.5	478
ZnO nanobrushes	150	5–150	100	19,276%[a]	16/6	5	479
Dumbbell-shaped ZnO	85, UV	10–100	100	20%[a]	~20/~10	10	480
Holey ZnO NSs	RT	5–100	100	115%[a]	9/6	5	129
SnO_2	250	0.1–20	6	221%[b]	7	0.1	153
WO_3	100	1000–4000	4000	60,800%[b]	~240–300/NG	1000	481
TiO_2	RT	1–1000	1	18%[a]	2/40	1	140
NiO	puled-T	200-1000	1000	3210%[b]	NG/NG	200	178
$Sn_{0.8}Ge_{0.2}O_2$ nanofibers	220	0.05–2000	1000	3913%[b]	~2/~58	0.05	187
La-doped SnO_2 nanofibers	300	5–35000	100	990%[b]	1/1	5	194
N-doped TiO_2	250	NG	1000	79,600%[b]	8/3.8	NG	200
Mn-doped In_2O_3 hollow NTs	360	0.025–500	20	180%[a]	4/15	0.025	482
Mn-doped α-Fe_2O_3	300	10–400	200	6350%[a]	10/24	10	186
NiO/SnO_2	260	10–300	50	~700%[b]	2.4/4.2	0.275	483
WO_3/TiO_2	RT	1000–10,000	10000	562%[b]	48/5	1000	484
SnO_2-Co_3O_4 nanocomposite	325	5–500	300	2275%[b]	4/27	5	201
$AgInO_2$	360	1–10,000	100	890%[b]	~6/~24	1	213
Pd/SnO_2	80	0.3–20,000	5000	~2500%[a]	~3.8/~9.5	0.3	485
Pt/ZnO NPs	300	100–40,000	1000	14.9%[a]	133/112	100	486
Pd/WO_3 nanoflowers	150	20–1000	500	865,898%b	1/3	20	487
PdRh/Fe_2O_3	230	0.2–400	10	10,590%[b]	17/21	0.043	243
PdPt/SnO_2	50	4.5–1000	1000	7,568,000%[b]	1/14	10	253
PdAu/ZnO	300	5–100	100	8000%[b]	36/720	5	488
PdPt/SnO_2	50	100–1000	1000	78,515%[b]	1/9	10	241
Pd-NiO/SnO_2	RT	0.1–1000	1	40,000%[b]	1/4.8	0.1	254
Pd/SiO_2/WO_3 microspheres	210	1–100	50	3350%[b]	5/136	1	489
Pd-SnO_2/ZnO	350	5–1000	50	~280%[b]	0.8/0.8	5	256

[a]Refers $S = \Delta R/R_0$ or $\Delta R/R_g$
[b]refers $S = R_0/R_g$ or R_g/R_0

experimental replicates), as displayed in Fig. 17b. Compared with conventional 2D materials such as GO, MoS_2 and MXene, the HsGDY showed around 2 orders higher sensing response without any baseline drift and 4/6 times faster t_{res}/t_{rec} (8/38 s) to 1% H_2, as shown in Fig. 17c. Among previously reported 2D materials (before 2023), this is the maximum detection speed without any dopants or functionalization[52]. Both theoretical and experimental approaches were employed to study the sensing mechanism of HsGDY, as illustrated in Fig. 17d-f. Based on the DFT results, H_2 is observed to adsorb within the pocket sites formed by the horizontal slip between the A and B layers of bulk HsGDY, resulting in an expansion in the distance between two acetylenic bonds within the pocket (Fig. 17d). Furthermore, the chemisorption of H_2 would take place with each H atom chemisorbing to the top and bottom acetylene group of the identified adsorption site (Fig. 17e). This chemisorb interactions between acetylenic bonds and H atoms were verified by in-situ Raman characterization in Fig. 17f.

In addition to designing sensing materials characterized by a porous structure and abundant defect sites, which

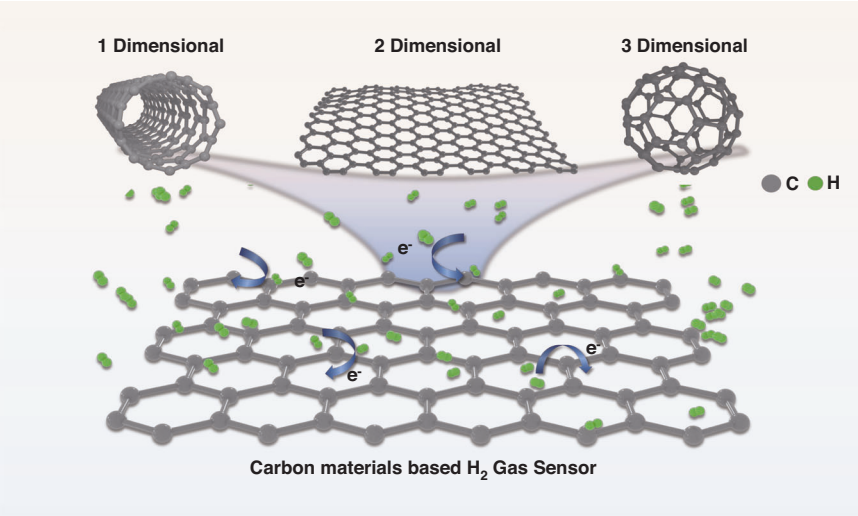

Fig. 16 The fundamental H_2 sensing mechanism based on carbon materials. Schematic diagram of H_2 adsorption and electron transfer on carbon materials with various dimensions

significantly enhance the number of active sites, the application of external energy (e.g., light and heat) is regarded as another effective strategy for improving sensor performance[279–283]. Specifically, elevating the temperature can optimize sensor response by activating the surface for chemisorption of target gas molecules[284]. Also, it ensures the complete desorption of gas molecules and accelerates the recovery process[285–288]. Park et al.[288] used polystyrene substrate as a template to create a wrinkled structure in multi-wall CNT (MWCNT) films via a thermal shrinkage effect. By increasing the applied voltage via electrothermal conversion, the operating temperature of the MWCNT films was raised, resulting in an improved sensing response to 10% H_2. However, additional heat supply increases power consumption and may bring about safety hazards when detecting flammable explosive H_2[289–291]. Applying light irradiation is a reliable alternative to enhance sensing ability which can modulate the concentration of photocarriers to promote charge transfer process, and provide more active sites for gas adsorption[292]. Tang et al.[293] applied UV irradiation to achieve the detection of H_2 down to 5 ppm based on pure Gr without modification (the sensor structure is shown in Fig. 17j). Prior to this, Gr alone was rarely reported as a H_2 sensor due to its lack of surface defects or functional groups, which limited gas adsorption[294,295]. In this case, UV light promotes the desorption of the pre-adsorbed water and oxygen on Gr surface, while also generating photogenerated carriers that enhance H_2 sensing capabilities[293]. Moreover, the change in surface potential illustrated in Fig. 17k revealed that UV light can alter electronic states of Gr into n-type doping, thereby accelerating desorption process. As shown in Fig. 17l, under illuminated conditions, the sensor exhibited a rapid and reversible response to 10 ppm H_2. Whereas, it showed no response in the absence of light, which indicates the critical role of UV light for proper sensing.

Despite the achievements in pure carbon materials for H_2 detection, most of them still suffer from unsatisfactory sensing performance owing to the weak physical adsorption on their surface. The limited intrinsic selectivity of pure carbon-based materials toward H_2 brings about challenges in the complex gas environment of TR process, ultimately compromising detection accuracy. Therefore, to increase sensor sensitivity and selectivity, various methods have been proposed, including surface treatments to introduce functional chemical groups, decoration of noble metal NPs and design of hybrid structure with MOSs.

H_2 sensors based on carbon materials with functional groups

During H_2 adsorption process, functional groups of carbon materials exert catalytic effects, promoting dissociation of H_2 into H atoms[296]. To date, surface treatment with liquid chemicals is a primary strategy to introducing of functional groups in CNT and Gr[296–300]. For CNT, strong acids (e.g., HNO_3, H_2SO_4) and strong oxidants (e.g., H_2O_2) are generally used to introduce functional groups (e.g., -OH, -N-H-, -C=O-) to the side walls and ends of CNTs[301,302]. Dhall et al.[296] developed a H_2 gas sensor based on multiwall CNTs (MWCNTs) with amount of functional groups (-COOH, -OH, C-O) (Fig. 18a and b). For functionalized MWCNTs (F-MWCNTs), there exist many H_2 adsorption sites, including outer surface, external grooves, interstitial channels, and inner pores, as shown in Fig. 18c.

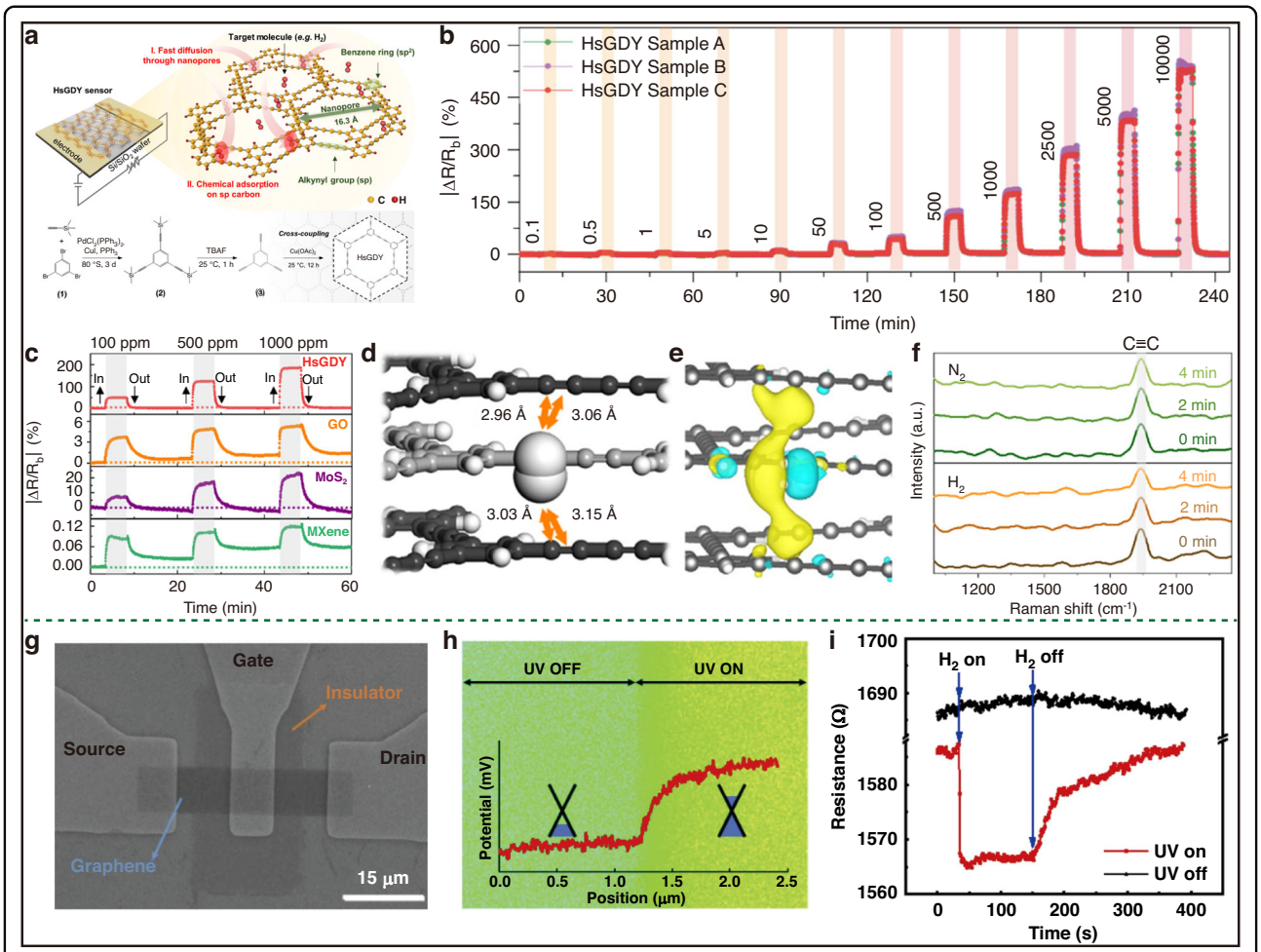

Fig. 17 H_2 sensors based on pure carbon materials. a Schematic illustration of the molecular sensing behavior and synthesis process of HsGDY; **b** Dynamic sensing response of HsGDY-based sensors to 0.1–10,000 ppm H_2; **c** Real-time response of HsGDY, and three other 2D materials upon H_2 exposure (100–1000 ppm); **d** Side-view image of the physisorbed configuration of the H_2 molecule in the interstitial pocket site between layers of HsGDY. **e** Charge density difference plot of HsGDY and physisorbed H_2 molecule; **f** In situ Raman spectra of the HsGDY film under N_2 and H_2 exposure[278]. Copyright 2023, American Chemical Society. **g** SEM image of Gr-based sensor; the effect of UV irradiation on **h** the surface potential and **i** sensing response of Gr[293]. Copyright 2025, Elsevier

Additionally, these functional groups act as catalysts that accelerate the adsorption/desorption rate[296,297]. Compared with raw MWCNTs (R-MWCNTs), the F-MWCNTs showed greatly improved sensitivity for H_2 sensing, as illustrated in Fig. 18d. After acid treatment, the response value of sensor increased from ~1.5% to 8%, and the t_{rec} was shortened from 190s to 100s. In terms of Gr, its derivatives, such as graphene oxide (GO) and reduced graphene oxide (rGO), possess a wealth of functional groups that serve as active sites for gas adsorption[303,304]. Figure 18e depicts a schematic diagram of an H_2 sensor based on GO NSs by using a porous PU foam as a substrate to form a dual-honeycomb structure. This porous device structure significantly enlarged the specific surface area and improved H_2 adsorption capacity. Figure 18f, g exhibits the concentration-dependent H_2-sensing performance and show that the sensor can detect H_2 in a range of 2–100%. Nevertheless, for effective warning of TR process, sensitive detection of low-concentration H_2 is critical[305]. Therefore, compared to GO, rGO is promising to achieve a lower LOD ascribing to existing abundant active defect sites, enhanced electrical conductivity, and Gr-like low noise features[306–308]. Since the density of functional groups, defect sites and conductivity of the rGO greatly depends on its reducing degree, modulating the degree of reduction presents an effective approach for optimizing its gas sensing capability[309–312]. To systematically investigate the effect of its reduction degree, Schipani et al.[300] fabricated a series of rGO-based sensors by varying the thermal reducing temperatures, as displayed in Fig. 18h. Raman spectra presented in Fig. 18i reveals that an increase in treatment temperature leads to a higher degree of reduction, which

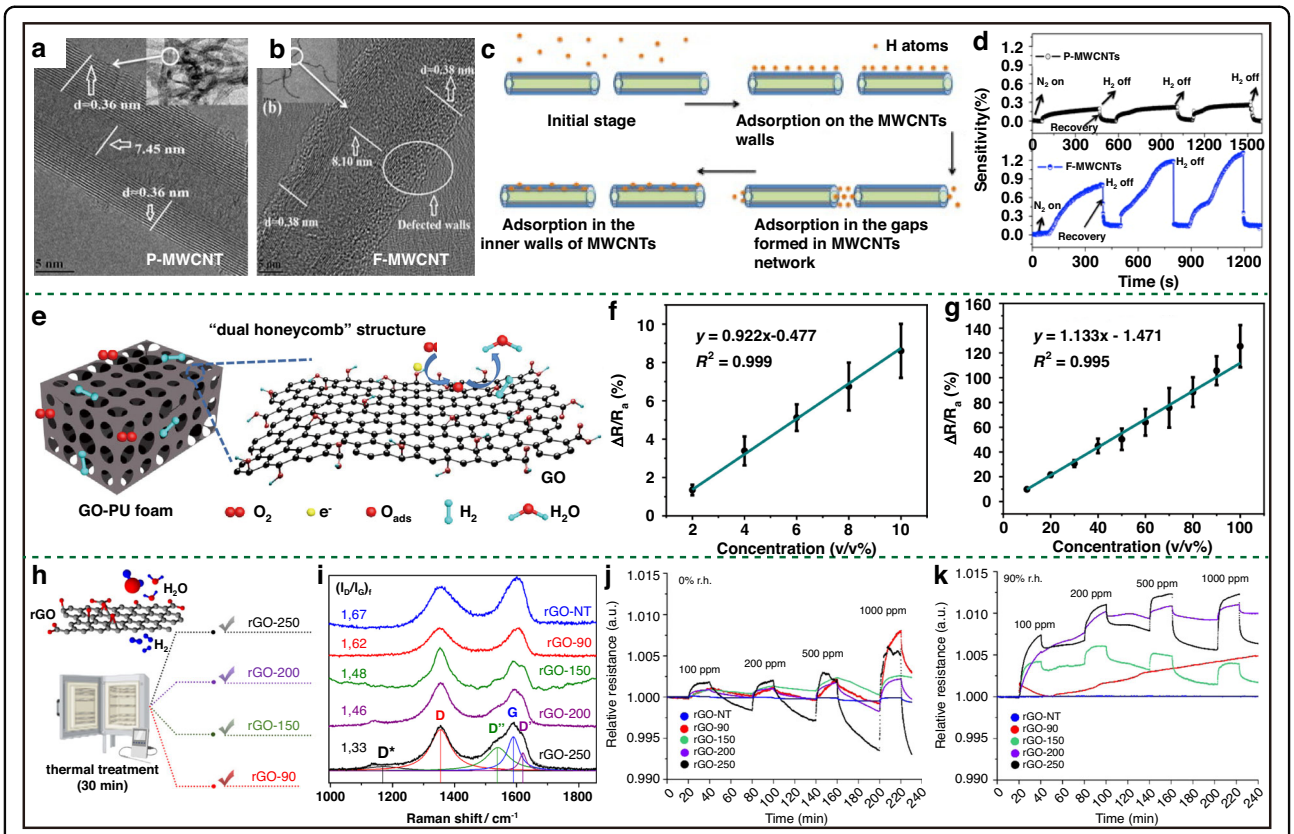

Fig. 18 Introduction of functional groups to improve sensing performance. HR-TEM images of **a** P-MWCNTs and **b** F-MWCNTs; **c** Schematic diagram mechanism for H_2 adsorption; **d** Dynamic response curve of P-MWCNTs and F-MWCNTs film at different concentrations of H_2[296]. Copyright 2013, Elsevier. **e** Schematic illustration of the porous GO structure and its sensing mechanism; **f**, **g** Linear gas response to various H_2 concentration (2–100%)[299]. Copyright 2022, American Chemical Society. **h** Schematic graph of rGO structure and the thermal process to prepare rGO sensors; **I** Raman spectra of rGO samples annealed at different temperatures; Response to H_2 concentrations from 100–1000 ppm for rGO-based sensors **j** in the absence of humidity and **k** under 90% RH[300]. Copyright 2023, American Chemical Society

correlates with an elevated content of sp^2 carbon within the rGO structure[300]. This reduction process provides a higher concentration of unsaturated carbon atoms that promote the current transport[298]. Figure 18j and k show that a higher degree of reduction in rGO enhances H_2 sensing response. Moreover, the higher degree of reduction lowered the content of oxygenated functional groups that may interact with H_2O[313–315], thereby improving the hydrophobic properties of rGO. The optimized rGO-based H_2 sensor exhibited a relatively good humidity tolerance, achieving a theoretical LOD down to ~2.5 ppm at high humidity[300,316]. Since the humidity in the environment undergoes dynamic and irregular fluctuations, employing carbon materials with hydrophobic properties to design sensing materials may diminish the impact of humidity on sensors in certain contexts.

H_2 sensors based on carbon materials decorated with hetero-materials

Another strategy to improve H_2 sensitivity of carbon materials is to construct heterostructures, including decoration of noble metals and combination of MOSs. Catalytic metals such as Pd[317–324], Pt[249,265,325,326] and Au[327] have been decorated on carbon materials to fabricate high-performance H_2 sensors mainly through aqueous reducing methods and physical deposition techniques[249,323,328–331]. In this system, carbon materials mainly act as channels for fast electron transportation as well as provide extra adsorption sites. Catalytic noble metals, such as Pd, Pt, Au etc., contribute to dissociation of H_2, and some of them can react with H_2 to form hydride as mentioned before[61,223,332]. Since intrinsic CNT is not sensitive to H_2, Girma et al.[324] fabricated Pd-SWCNTs films with Pd NPs evenly distributed on SWCNTs (Fig. 19a-c). The response curve in Fig. 19d revealed that the sensor achieved a wide H_2 detection range (0.002–2%) and a fast t_{res}/t_{rec} (10/3 s) to 1% H_2. The decoration of Pd NPs is critical to enhance H_2 sensing through reducing the adsorption energy of H_2 as well as lowering the activation energy of reactions between H_2 and adsorbed oxygen species[324]. For this kind of composites, the content of decorated noble NPs plays a

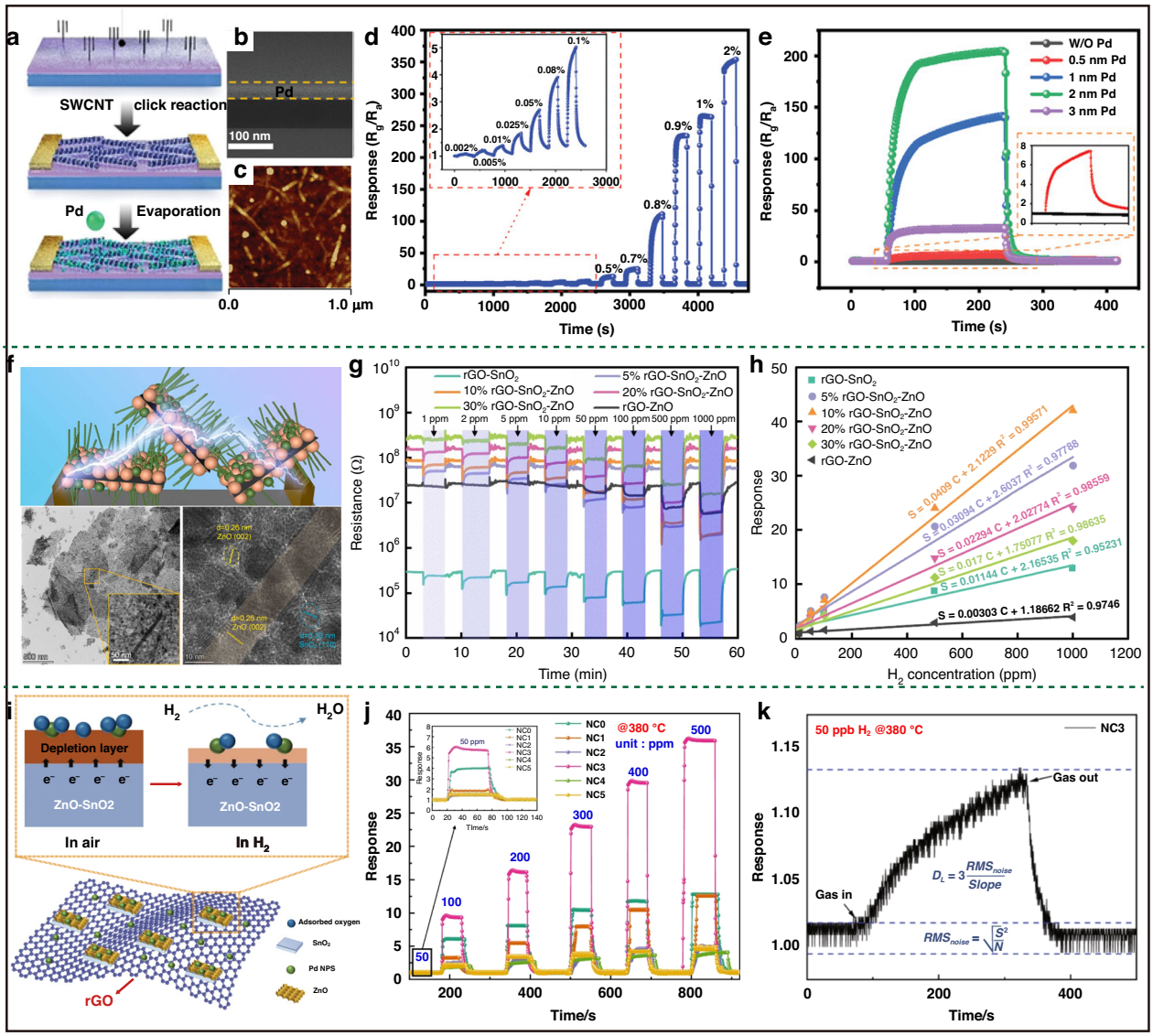

Fig. 19 High performance carbon based H_2 sensors via noble metal decoration or construction of heterojunctions. a Fabrication of Pd decorated SWCNT-based H_2 sensors and the corresponding **b** TEM and **c** AFM images; **d** Sensing responses toward various H_2 concentrations (2 ppm–1%); **e** Effect of the Pd thickness on sensor response under 1% H_2[324]. Copyright 2023, John Wiley and Sons. **F** Schematic illustration and TEM image of rGO-SnO_2-ZnO nanocomposites; **g** Dynamic resistance change curves and **h** the response versus H_2 concentration from 1 to 1000 ppm at 175 °C[346]. Copyright 2023, Elsevier. **i** Schematic graph of structure and sensing mechanism of Pd-doped rGO/ZnO-SnO_2 nanocomposite; **j** Dynamic response curves of samples towards 50–500 ppm H_2 at 380 °C (NC0, NC1, NC2, NC3, NC4, and NC5 represent samples with the weight ratios (wt%) of the GO and ZnO-SnO_2 being 0, 1, 2, 3, 4, and 5 wt%, respectively); **k** Response transients of the sensor to 50 ppb H_2[352]. Copyright 2022, Springer Nature

significant role in H_2 sensing performance, as shown in Fig. 19e. On one hand, excessively thin Pd film fails to generate sufficient effective sites to interact with H_2. Conversely, excess surface coverage of Pd introduces additional Pd conduction pathways that are less sensitive to electron transfer than semiconducting channels[323,324,333]. Moreover, to further enhance the sensing performance of noble metal-decorated carbon materials, bimetallic NPs are used to modify carbon materials such as NiPd[334], PdPt[335], NiPt[249,336], AuPt[337]. It has been reported that bimetallic catalysts can reduce the hysteresis of single noble metals and lower the adsorption energy of H_2[105,249,320], thus exhibit better sensitivity and reversibility than monometallic counterparts[338].

The second method to promote H_2 sensing ability is the addition of MOSs to carbon materials. MOSs have received widespread attention in the development of commercial gas sensors in regard of its simplicity of use and low cost, and acceptable sensitivity[339]. Incorporation of MOSs into carbon materials generates heterostructures

and induces more adsorption sites, which facilitates the adsorption of H_2 molecules and promotes electron transfer process[207,340]. Thus, the design of MOSs nanostructures in the hybrid is critical for modulating H_2 sensing performance[98,339–345]. Li et al.[346] fabricated rGO-SnO_2-ZnO nanocomposites, where 1D ZnO was distributed on 2D rGO-SnO_2 film to form heterostructures, as shown in Fig. 19f. The construction of heterojunction interfaces results in a greater variation in resistance decrease upon H_2 exposure and thus amplify the sensing response[346]. The fabricated rGO-SnO_2-ZnO-based H_2 sensor showed a wide detection range of 1–1000 ppm (Fig. 19g, h) and with a high response value of 19 to 500 ppm H_2, which surpassed the sensors based on rGO-SnO_2 (10.5) and rGO-ZnO (5.6).

Furthermore, the construction of multi-component systems, by incorporation of both noble metals and MOSs into carbon materials, can further improve H_2 sensing performance[347–353]. Typically, Zhang et al.[352] synthesized Pd-decorated rGO/ZnO-SnO_2 to fabricate H_2 sensors with good sensing properties (Fig. 19i). In this hybrid system, the high surface area of rGO facilitated H_2 adsorption and the formed a p-n-n heterojunction of rGO/ZnO-SnO_2 could amplify the changes in resistance, leading to enhanced sensing response, as shown in Fig. 19j[354]. Moreover, the selective reaction of Pd with H_2, coupled with its spillover effect, greatly contributed to the high sensitivity and accelerated response/recovery rate. From the sensing results in Fig. 19j, k, the Pd-decorated rGO/ZnO-SnO_2 nanocomposites can detect H_2 concentration from 0.05 to 500 ppm at 380 °C and shows the high response of 9.4 to 100 ppm H_2 within few seconds ($t_{res}/t_{rec} = 4/8$ s). The greatly enhanced sensor performance can be attributed to synergetic effects including good electronic properties and high specific surface area of rGO, electron transfer modulation of formed heterojunctions, as well as catalytic effects of Pd NPs. This highlights the importance of constructing hierarchical structures for H_2 sensing applications. The functionalization with noble metals and MOSs enhances the material's selective response to H_2, as well as yields a remarkable improvement in sensitivity by orders of magnitude, pushing LOD to the ppb level. It also enhances the sensor's selectivity toward H_2, which is crucial for reliable detection against gas interference inside battery packs. The resulting sensors achieved a rapid t_{res} close to 1 s, nearly satisfying the US DOE benchmark. This strategy of constructing heterostructures establishes a robust platform facilitating adaptive sensing capabilities and ensuring battery safety.

Sensing properties of carbon-based H_2 sensors have been summarized in Table 4. In general, carbon-based materials, such as CNTs and Gr, featured with high specific surface area, high carrier mobility and low operation temperature have been regarded as promising candidates for RT gas sensing applications. However, most pristine carbon materials suffer from poor sensitivity to H_2 because of weak adsorption. Although construction of carbo-based composites can lower the LOD and enhance their sensitivity, high operation temperature is still required for composites containing MOSs in most cases.

2D material-based chemiresistive H_2 sensor

H_2 sensors based on pure 2D materials

With the advancement of nanomaterial technology, 2D van der Waals (vdW) materials are attracting attention in gas sensing realm regarding to their high surface-to-volume ratio, unique electrical and optical properties[355]. These features facilitate electron transfer via molecular adsorption at RT. 2D materials, especially TMDs such as MoS_2, $MoSe_2$, WS_2, and SnS_2, have been widely investigated as sensing materials for H_2 detection[356–361]. However, bare TMDs-based H_2 gas sensors suffered from long t_{res}/t_{rec} and low sensitivity. To address these problems, several strategies have been proposed including design of porous nanostructures, modulation of vacancies, and construction of heterojunctions. The design of porous nanostructures, such as self-assembly of TMDs NSs to form hollow tubular, spherical and aerogel nanostructures, presents an effective method to enhance the exposed area of 2D materials and provide efficient pathways for gas diffusion[362–364]. Apart from porous nanostructures, Agrawal et al.[365] reported a pyramid MoS_2 structure for H_2 sensing, which was formed by layer to layer growth of monolayer MoS_2, as shown in Fig. 20a. The sensing performance of pyramid MoS_2 is exhibited in Fig. 20b, c. Compared with traditional MOS-based and other bare MoS_2-based H_2 sensor reported in literatures, the fabricated sensor showed superior performance by exhibiting a high sensitivity (69.1%) and a short t_{res} (32.9 s)[366–368]. Because this unique stacked in-plane monolayer of MoS_2 pyramid increases favorable adsorption sites on MoS_2, including top of hexagon (H), top of Mo atoms (T_M) and top of S atoms (T_S)[369]. Furthermore, modulation of vacancies is also an promising approach to increase H_2 sensitivity[370,371]. For TMDs, vacancies like S vacancies, Se vacancies serve as the major gas adsorption centers owing to their high catalytic activity[372–375]. They tend to induce greater electron transfer and stronger interaction with target gases according to theoretical calculations[376,377]. Rezende et al.[370] investigated the role of S vacancies in MoS_2 for H_2 sensing and the relevant optical image of the MoS_2-based H_2 sensor is shown in Fig. 20d. The concentration of S vacancies was precisely regulated through the deposition of Al_2O_3 on MoS_2. This is attributed to the preferential growth of Al_2O_3 on surfaces with localized defects, which effectively passivates

Table 4 Summary of sensing properties of carbon-based H_2 sensors

Material	*T* (°C)	Detection range (ppm)	Tested concentration (ppm)	Response	t_{res} /t_{rec} (s)	Tested LOD (ppm)	Ref.
SWCNTs	RT	NG	1000	0.25%[a]	NG/<60	NG	268
Nanocrystalline diamond CNT	RT	10–500	500	5.3%[a]	48/53	10	270
Graphyne	300	0.1–10,000	10,000	542%[a]	8/38	0.1	278
rGO/PU foam	RT	20,000–1,000,000	500,000	~50%[a]	68/37	20,000	45
Gr/N_2@UNCD	RT	50–500	500	14.6%[a]	36/32	50	264
Candle carbon soot	RT	5000–20,000	5000	~2%[a]	7/10	5000	490
CNT (acid-treated)	RT	500–5000	500	0.8%[a]	NG/ ~ 100	500	296
CNT (HNO_3 treated)	75	20–300	300	368%[a]	15/72	20	297
Pd/sorted CNTs	RT	0.89–311	311	>100,000%[a]	7/89	0.89	323
Pd/SWCNTs Covered with PMMA	RT	20–20,000	10,000	28,500%[b]	10/3	20	324
Pd/3D Gr	RT	1000–30,000	30,000	41.9%[a]	8/38	1000	491
Au/Gr	RT	1–1000	500	5.46%[a]	16/274	1	327
Pd/rGO	RT	2500–400,000	20,000	221%[b]	18/NG	2500	317
Pd NPs/CN 3D framework	RT	200–400,000	20,000	27.6%[a]	~25/~223	200	322
PdO/CNT yarns	RT	1000–40,000	10,000	~53.7%[a]	2/NG	1000	98
SnO_2-GO thin film	300	5–25	25	112%[a]	66.4/74	5	340
rGO/SnO_2	225	5–1000	500	1188%[b]	2/19	5	343
SnO_2/Gr	150	0.1–60	50	22.85%[a]	NG/NG	0.1	345
Protonic Titanate-rGO	RT	10–1000	1000	950%[a]	200/110	10	492
PVDF/SnO_2/rGO	RT	10–1000	100	49.2%[a]	34/42	10	344
AuSn/rGO-SnO_2	175	1–1000	500	7730%[b]	30>/60>	1	349
rGO/SnO_2-Pd	390	0.1–1000	0.1	~800%[b]	60>/3	0.1	353
Pd-rGO/ZnO-SnO_2	380	0.05–500	100	940%[b]	4/8	0.05	352

[a]Refers $S = \Delta R/R_0$ or $\Delta R/R_g$; [b] refers $S = R_0/R_g$ or R_g/R_0

the S vacancies. Figure 20e presents the H_2 sensing mechanism, the dissociative adsorption of H_2 is facilitated by the catalytic effect of S vacancies[378,379]. In Fig. 20f, the MoS_2-based sensor before Al_2O_3 deposition displayed obvious responses to H_2 from 0.5% to 50%. While after Al_2O_3 deposition, the sensor exhibited lower sensitivity and a longer t_{res}/t_{rec} (Fig. 20g), ascribing to the reduced S vacancies. Another method to improve H_2 diffusion and absorption is hybridizing TMDs to form heterojunctions, since EDL formed at the hetero-interface can tailor the electron transfer and actively tune the sensing performance[380,381]. Kalita et al.[382] synthesized $MoSe_2$-WSe_2 NSs for H_2 sensing through a liquid phase exfoliation method. As shown in Fig. 20h, i, during the exfoliation process, functional groups, vacancies, and structural defects are formed within the NSs of $MoSe_2$-WSe_2, leading to increased active sites for gas adsorption[360]. Compared to pure WSe_2, the formation of a built-in potential at the hetero-interface between WSe_2 and $MoSe_2$ facilitates adsorption of oxygen onto the surface of $MoSe_2$-WSe_2, promoting the reaction with H_2 and electron transfer (Fig. 20i, j)[382]. As illustrated in Fig. 20k, the $MoSe_2$-WSe_2-based showed a response of 59.57% to 25 ppm H_2, which is higher than that of WSe_2-(~38%) based sensors. Furthermore, owing to the enhanced efficiency of electron transfer, the t_{res} of $MoSe_2$-WSe_2-based sensor obviously shorted (Fig. 20l). However, sensors based on pristine 2D materials face limitations in detecting low H_2 concentrations and exhibit cross-sensitivity to polar gases (e.g., NH_3 and NO_2)[45,281,383]. Consequently, achieving highly sensitive and selective H_2 sensing with pure 2D materials remains challenging, which calls for effective methods, such as combining with noble metals or MOSs to improve their H_2 sensing properties.

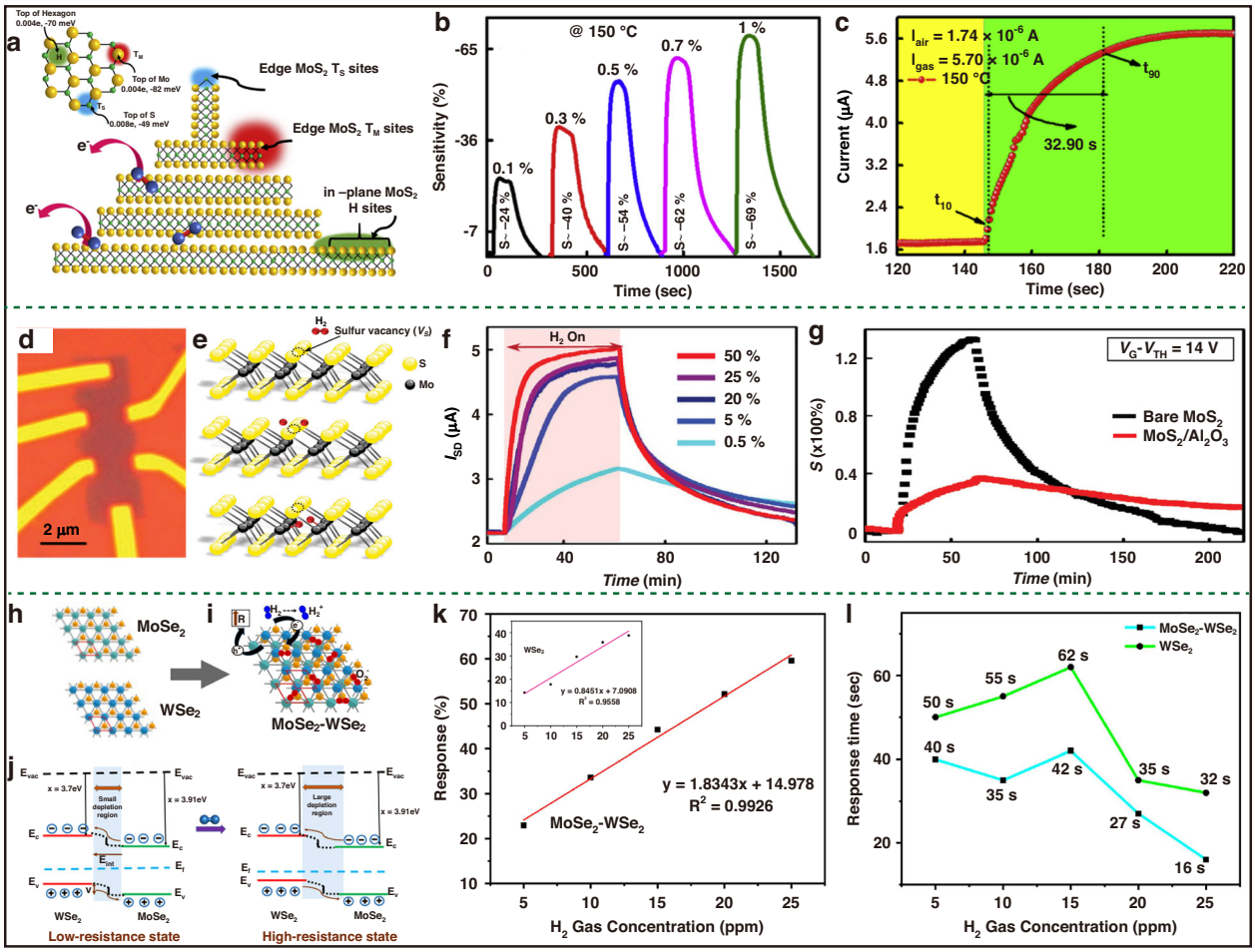

Fig. 20 Different approaches for enhancing H_2 sensing response of pristine 2D materials. a Schematic illustration of adsorption sites and interaction with H_2 on MoS_2 pyramids; **b** Dynamic response for different concentrations of H_2 and **c** response time of 1% H_2 at 150 °C[365]. Copyright 2020, Elsevier. **d** Optical image of the MoS_2 sensor and **e** representation of H_2 adsorption on V_S; **f** Real-time current change for different H_2 concentrations (0.5–50%); **g** Sensor response toward 20% H_2 of MoS_2 before and after Al_2O_3 adsorption[370]. Copyright 2019, John Wiley and Sons. Schematic diagram of **h** $MoSe_2$ and WSe_2, and **i** $MoSe_2$-WSe_2 nanocomposites; **j** Sensing mechanism of $MoSe_2$-WSe_2; **k** Correlation curve between sensor response and gas concentrations (5–25 ppm H_2) of $MoSe_2$-WSe_2; **l** Response time curve of $MoSe_2$-WSe_2 and WSe_2[382]. Copyright 2025, Elsevier

Noble metal decorated 2D materials

To increase H_2 selectivity, decoration of TMDs with noble metal NPs (Pd[359,384–393], Pt[358,394–397], Au[59,391], Ce[398] etc.) or metal alloys[399,400] is one common approach due to their catalytic properties and spillover effects[389,395,397]. Suh et al.[391] have found that modifying the MoS_2 surface with Pd leads to improved H_2 sensing performance. The underlying mechanism involves significant charge transfer upon H_2 exposure, facilitated by the spillover effect and the formation of PdH_x. which reduces the hole concentration and increases the resistance of the p-type MoS_2. Kim et al.[59] decorated different noble metal NPs on MoS_2 flakes (Fig. 21a), and investigated their respective role on the selectivity change by experimental and theoretical methods. Through DFT theoretical calculations, they observed a significant increase in binding energy for Pd (2.47 eV) and Pt (1.94 eV) when compared to pristine MoS_2 (0.15 eV), with reactive adsorption oxygen on the surface identified as the favorable binding sites (Fig. 21b, c). This finding is consistent with the experimental results in Fig. 21d. Therefore, apart from facilitating electron transfer, the decoration of Pd, Pt provides strong chemisorption sites for enhanced H_2 adsorption. Many reports have also observed similar performance improvements by noble metal decoration[386,389,391,392,394]. Moreover, assembling 2D materials into 3D hollow structures can further improve sensing response[358,359,366,396]. For instance, Park et al.[396], designed Pt-decorated ultrathin MoS_2 hollow spheres, resulting in a significant enhancement of the H_2 sensing performance, including response value and t_{res}/t_{rec}, compared with non-hollow structure. Wu et al.[384]

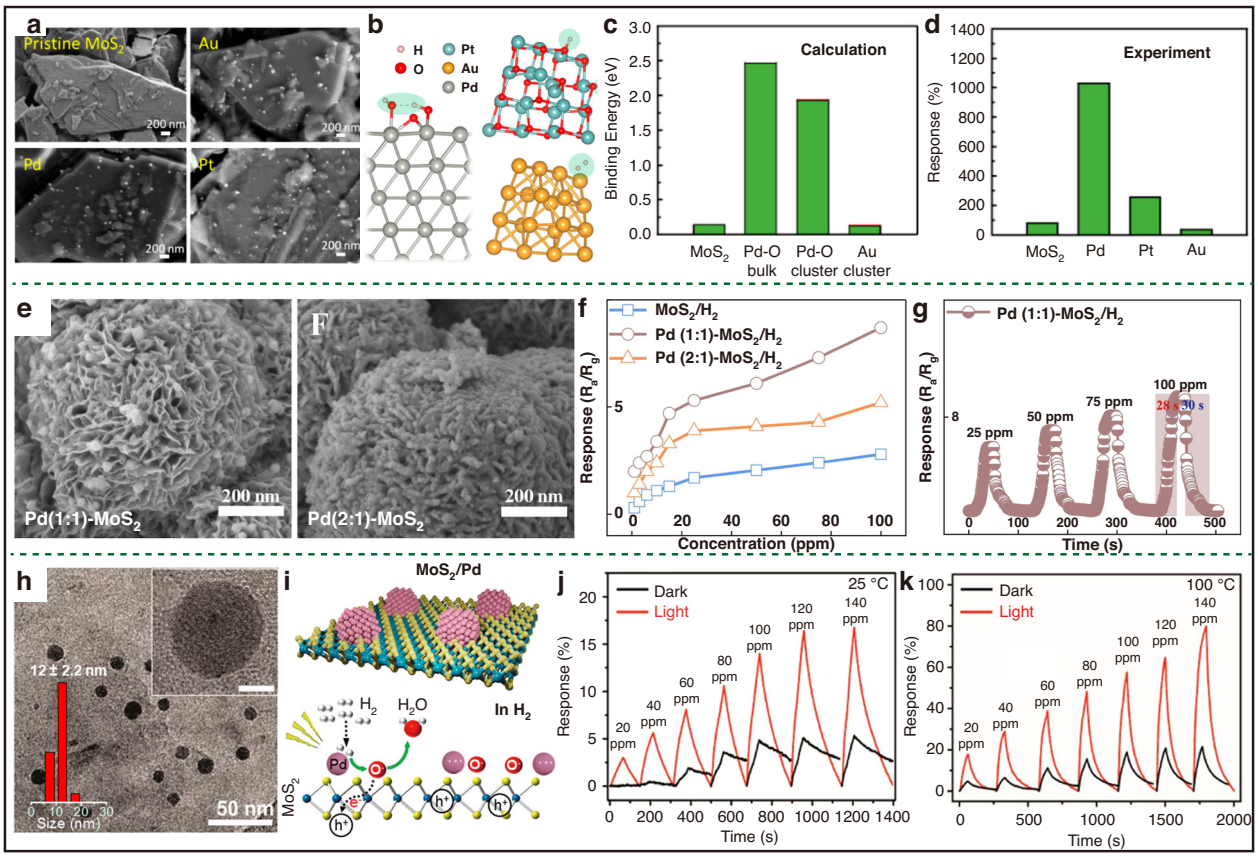

Fig. 21 Decoration of noble metal catalysts for improved H_2 sensitivity of 2D material based sensors. a SEM image of pristine MoS_2 and MoS_2 decorated with Pd, Pt, Au NPs; **b** Binding structure of H_2 molecule on different noble metal NPs; **c** H_2 binding energy and **d** the corresponding sensing values on various systems[59]. Copyright 2023, American Chemical Society. **e** SEM images of Pd (1:1)- MoS_2, and Pd (2:1)-MoS_2 at 200 nm scale; **f** Gas sensing response of MoS_2 sensors with varying concentrations of Pd NPs: **g** Dynamic response curve for different H_2 concentrations (25–100 ppm) of Pd (1:1)-MoS_2[384]. Copyright 2025, Elsevier. **h** High-magnification TEM image and **I** light activated sensing mechanism of MoS_2 decorated with Pd nanoclusters; Sensing response under dark and light conditions at **j** 25 °C and **k** 100 °C[390]. Copyright 2021, American Chemical Society

synthesized self-assembled MoS_2 NSs with Pd decoration and investigated the H_2 sensing performance. Figure 21e illustrates the evolution of MoS_2 nanoflowers with varying concentrations of Pd NPs. In the case of Pd (1:1)-MoS_2, Pd NPs were deposited along the edges of MoS_2 nanosheets while preserving their porous structure. Conversely, in the Pd (2:1)-MoS_2 composites, the high coverage of Pd NPs resulted in a reduction in material porosity, consequently leading to fewer accessible active sites. Thereby, the Pd (1:1)-MoS_2-based sensor showed the highest sensing response of 8.7 towards 100 ppm H_2, attributed to the catalytic effect of Pd NPs and the preservation of its porous structure (as illustrated in Fig. 21f, g). Similar to carbon materials, utilization of external heat or light energy during the sensing measurement is also an effective approach to improve the sensor performance[279–283]. Mai et al.[390] reported a light-induced H_2 sensor based on monolayer MoS_2 with Pd nanoclusters evenly distributed on MoS_2 surface (Fig. 21h). The sensing mechanism in Fig. 21i revealed that light irradiation generated additional charge carriers and reduced the background resistance which in turn amplified the sensing responsivity[390]. The sensor performance was studied under dark and light conditions at different working temperatures. Figure 21j, k demonstrate that sensing response is greatly enhanced under light illumination. Moreover, as the temperature increased from RT (Fig. 21g) to 100 °C (Fig. 21h), t_{res} was shortened from 351 s to 47 s. Therefore, the results verified the positive role of heat input and light irradiation in terms of the enhancement of sensor performance. Although decoration of noble metals and regulation of test conditions could enhance the sensitivity of 2D materials toward H_2, the adsorption/desorption kinetics remain relatively slow (hundred seconds of t_{res}/t_{rec}) that poses challenges for real-time monitoring. Thus, further methods are needed to address these hurdles to facilitate early failure detection in LIBs.

H_2 sensor based on MOSs modified 2D materials

Another promising strategy to enhance the sensing performance of 2D materials involves hybridizing them with MOSs to form heterojunctions. The gas sensing performance of these heterostructures can be tailored by controlling their composition, architecture, and surface properties. Yang et al.[401] utilized a hydrothermal method to prepare 2D MoS_2-decorated Zn-doped MoO_3 nanoribbons and the SEM/TEM images are shown in Fig. 22a. The composites showed enhanced sensitivity with a wide H_2 detection range (5–1500 ppm) and a good linear response (Fig. 22b, c). Beyond binary composites, the construction of more complex hybrids, such as synthesis of ternary composites and functionalization of noble metals, can further enhance the gas sensing response. Bai et al.[402] prepared the heterostructural CdS/PbS/SnO_2 composites which exhibited a response of 1125.2% to 100 ppm H_2 that is an order of magnitude greater than that of CdS/SnO_2 and PbS/SnO_2 at 200 °C. Meng et al.[361] used the hydrothermal method to prepare SnS_2/SnO_2 nanocomposites, with agglomerated SnO_2 NPs wrapped in the SnS_2 flakes, as shown in Fig. 22d. The composite was later modified with Pd NPs and demonstrated improved H_2 sensing performance due to Pd decoration by promoting the adsorption/dissociation of H_2 molecules. Figure 22e shows that 1.0 At. % Pd/SnS_2/SnO_2 sensor exhibited high response (95) and rapid t_{res}/t_{rec} (1/9 s) to 500 ppm H_2 at 300 °C. However, as shown in Fig. 22f, the response of the Pd/SnS_2/SnO_2 composites exhibited a slight fluctuating downward trend over 30 days. This instability may be due to partial oxidation of the 2D materials at high temperature under air atmosphere[403]. Furthermore, even at mild operating temperatures, long-term signal drift problems still occur due to slow oxidation of TMDs[356,404]. Therefore, for TMDs-MOSs composites with direct exposure of the TMDs, often fail to maintain good long-term stability[361]. In contrast, in-situ oxidation can form a dense of passivating MOS layer on the surface of 2D material and thereby inhibiting further oxidation of 2D material.[356]. Moreover, by adjusting oxidation times and temperatures, the thickness of MOS layer can be tuned to match the Debye length for improvement of sensing performance[405,406]. Various types of MOS/TMDs heterostructures have been synthesized including MoO_3/MoS_2[387], WO_3/WS_2[356,407], SnO_2/$SnSe_2$[408], and In_2O_3/In_2Se_3[409]. For instance, Paolucci et al.[408] obtained the amorphous SnO_2/$SnSe_2$ heterostructure by partially oxidation of $SnSe_2$, with the inner $SnSe_2$ uniformly covered by a self-terminating SnO_2 layer. After annealing the $SnSe_2$ in air at 200 °C for 48 h, a uniformly amorphous SnO_2 layer was formed on the surface of $SnSe_2$, as shown in HRTEM images (Fig. 22g). Attributing to the passivation effect of the formed SnO_2 layer, the inner $SnSe_2$ was prevented from further oxidation even when extending the annealing time to 170 h 220 °C (Fig. 22g). The obtained SnO_2/$SnSe_2$-based H_2 sensor exhibited a low LOD (5 ppm) and a short t_{res}/t_{rec} (3/19 s), as shown in Fig. 22b. Due to the chemical stability of surface SnO_2, the baseline resistance of the SnO_2/$SnSe_2$ showed no substantial differences as the operating temperature was cycled from RT to 150 °C and reversed back to RT (Fig. 22i). The response of the SnO_2/$SnSe_2$-based sensor to 100 ppm H_2 remained almost the same over a period of one year (Fig. 22j). The good long-term stability of In_2O_3/In_2Se_3 materials prepared via in-situ oxidation is also observed[409]. Figure 22k and l reveal the sensing properties of In_2O_3/In_2Se_3 and its good reproducibility of baseline resistance at different working temperatures even after one year, which further proves that the oxide skin layer effectively passivated the underlying TMD layer from spontaneous degradation[409]. Therefore, compared to merely construction MOS/TMD composites, the introduction of MOS passivation layer can significant extent the device lifetime and provide robust operation across an RH range of 0–80%. By further functionalization with noble metals, the detection of H_2 can be cut down to only 1 s, satisfying the requirements of US DOE for practical application.

2D MXene-based H_2 sensors

MXene is a class of carbide, nitride and carbon nitride 2D materials and has attracted wide attention due to its unique physiochemical properties and high electrical conductivity[410–412]. Generally, MXenes are prepared by selective etching of metal atoms of MAX phases in fluoride-contained acidic solution, leading to formation of -O, -OH, and/or -F functional groups[413,414]. Its chemical formula can be expressed as $M_{n+1}X_nT_x$, where M is the transition metal, X is carbon and/or nitrogen, T_x represents the surface groups. Different to most 2D materials, such as Gr, WS_2, and MoS_2, the abundance of functional groups present on the surface of 2D MXenes facilitates an increase in interlayer spacing within assembled MXene NSs. This expansion enhances the active surface area and creates nanosized interlayer channels that allow analytes to diffuse between the layers of stacked MXenes[415]. Lee et al.[416], synthesized single-/few-layer 2D V_2CT_x by etching V_2AlC MAX in 50% HF solution for 92 h at RT, as shown in Fig. 23a. After etching process, the interlayer space of V_2CT_x expands and the surface of it is terminated with -O, -OH and -F functional groups. The presence of the oxygen containing functional groups, indicating partial surface oxidation of V_2CT_x into VO_x. Attributing to a higher selectivity of vanadium oxides (VO_2, V_2O_5) and V-doped MOSs toward H_2[417–419], the V_2CT_x-based sensor demonstrated a significantly higher response to H_2 compared to other gases (Fig. 23b). The sensor also achieved detection of H_2 from 2 to 100 ppm with good linearity at RT under ambient humidity (Fig. 23c). Similar to other materials, modification of noble metal NPs and hybridization of with MOSs are accessible approaches to

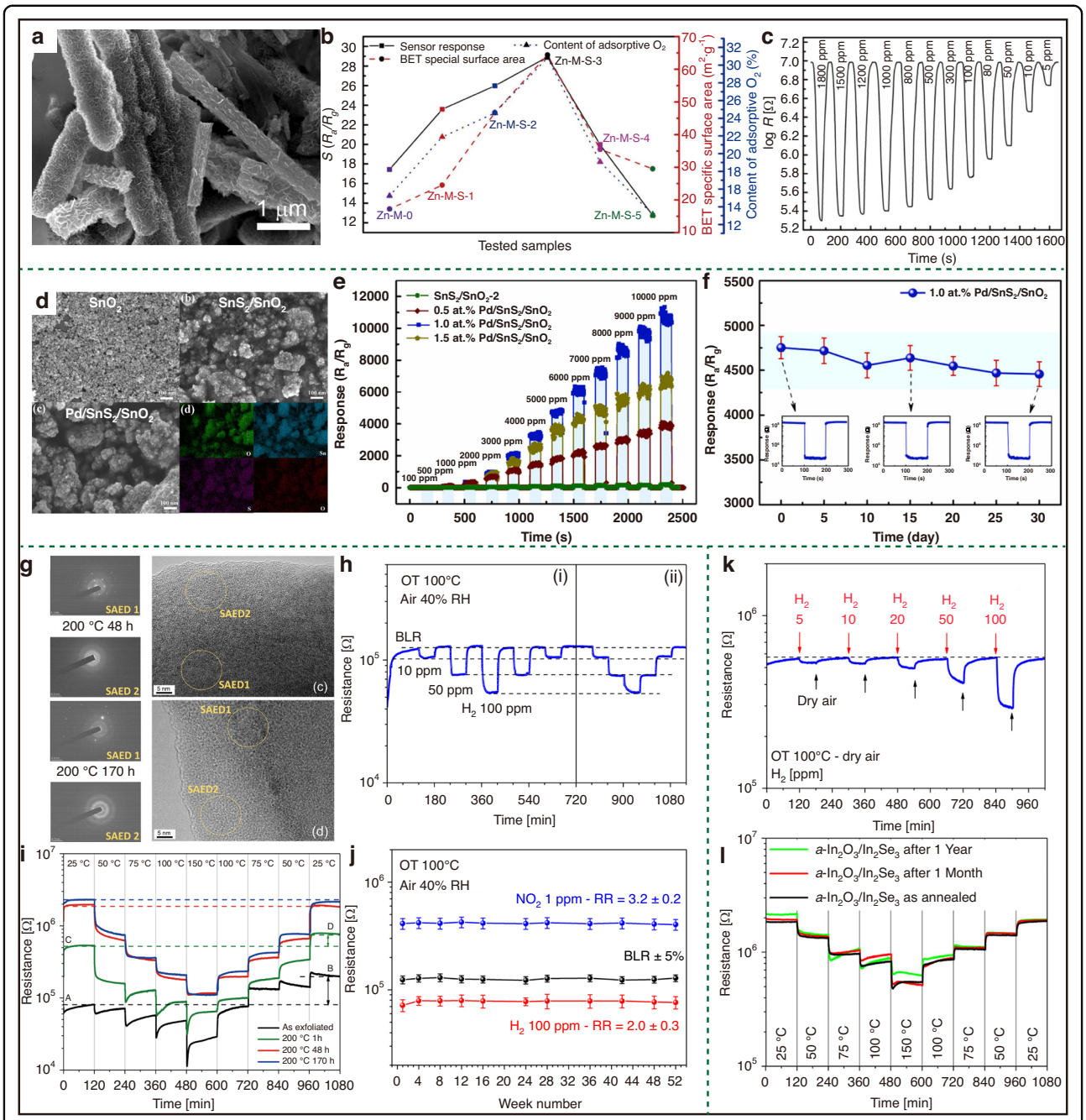

Fig. 22 Construction of heterojunctions to improve stability in 2D material based H_2 sensors. a TEM image of 2D MoS_2-decorated MoO_3; **b** The relationships among the sensor response, the BET specific surface area and the content of the adsorptive oxygen; **c** Sensing response towards 5–1800 ppm H_2[401]. Copyright 2022, Elsevier. **d** SEM images of SnO_2, SnS_2/SnO_2 and $Pd/SnS_2/SnO_2$; **e** Response curves of $Pd/SnS_2/SnO_2$ towards 100–10,000 ppm H_2; **f** Long-term stability of 1.0 at% $Pd/SnS_2/SnO_2$ to 5000 ppm H_2 at 300 °C[361]. Copyright 2022, Elsevier. **g** HRTEM images and related SAED patterns of the 48 h and 170 h annealed $SnSe_2$ flakes in air at 200 °C; **h** Dynamic electrical responses of $SnO_2/SnSe_2$ at 100 °C to H_2 (5–100 ppm); **i** Baseline resistances change of $SnO_2/SnSe_2$ with different annealing times by modulating the working temperature in 25–150–25 °C range; **j** Long-term stability of $SnO_2/SnSe_2$ sample to100 ppm H_2 over one year[408]. Copyright 2022, Elsevier. **k** Dynamic electrical responses of In_2O_3/In_2Se_3 at 100 °C to H_2 (5–100 ppm); **l** Baseline resistance variations of In_2O_3/In_2Se_3 by modulating the working temperature in 25–150–25 °C range over different time periods[409]. Copyright 2023, American Chemical Society

improve response and recovery speed of MXene materials. Noble metal promotes the adsorption and dissociation of H_2, and some of them can selectively react with H_2 to form hydride as mentioned before[417,420–422]. Moreover, it has been reported that bimetals can achieve higher reactivity than monometallic counterparts[110,249,338].

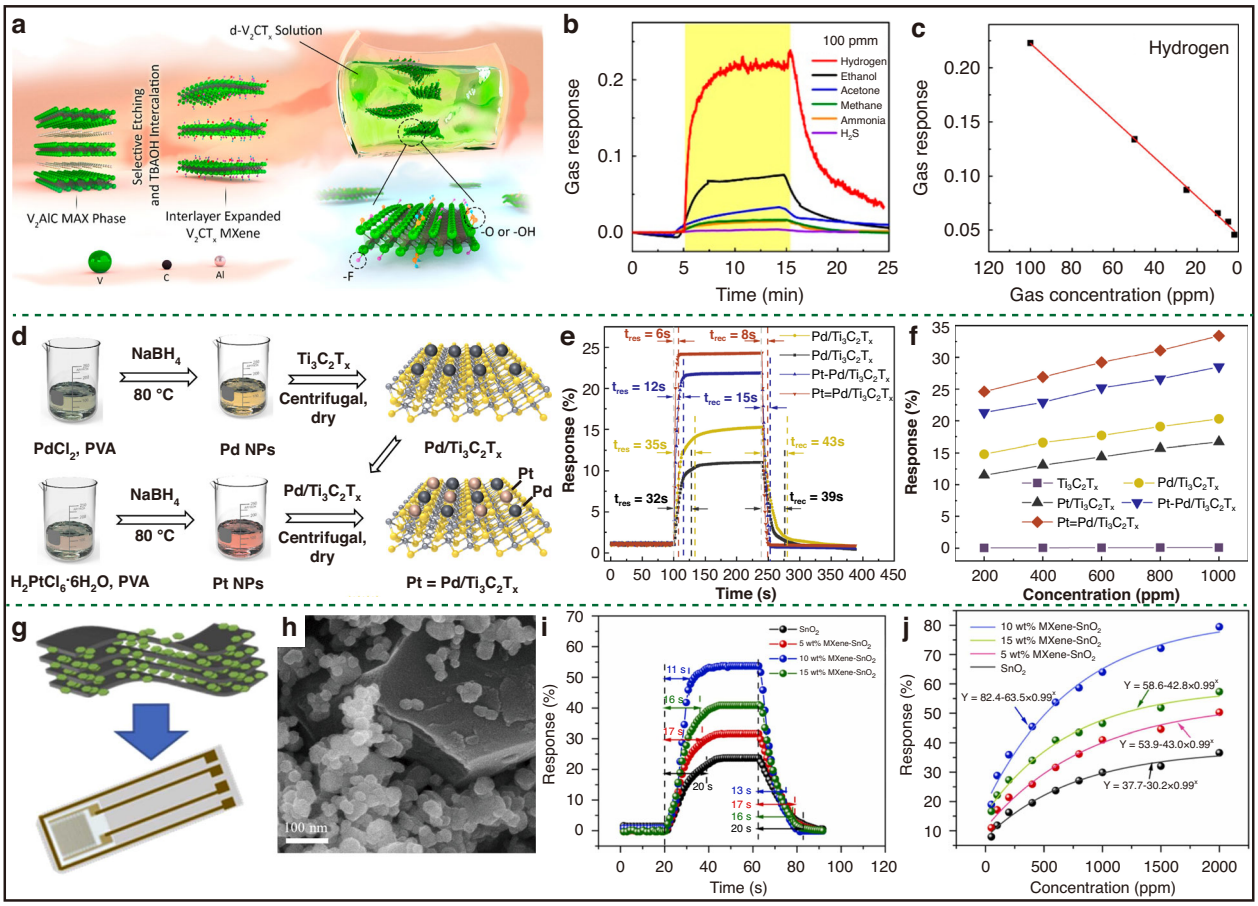

Fig. 23 The strategies to enhance the sensing performance of Mxene based H_2 sensors. a Schematic illustration of the synthesis and delamination of V_2CT_X MXene; **b** Gas response toward 100 ppm H_2 and five other interfering gases at RT; **c** Relationship between response and concentration of H_2 (6–200 ppm)[416]. Copyright 2019, American Chemical Society. **d** Schematic diagram of the synthesis procedure of Pt=Pd/$Ti_3C_2T_X$; Sensing properties of four samples: **e** response/recovery time at 200 ppm H_2 and **f** response versus H_2 concentration (200–1000 ppm)[425]. Copyright 2023, Elsevier. **g** Heterostructural illustration and **h** SEM image of SnO_2-MXene composite nanomaterials; **i** Transient response curves to 600 ppm H_2 and **j** fitting curve of response to 10–2000 ppm H_2 of MXene/SnO_2 composite sensors with various ratios[427]. Copyright 2024, Elsevier

Compared to bimetallic alloys, where the electrochemical potential of the alloy presents a compromise between the two constituent metals, researchers have reported that the spatially separated bimetals NPs exhibit enhanced catalytic activity in the realm of electrocatalysis[423,424]. However, such separated bimetals have been rarely explored for gas sensing applications. Recently, Wang et al.[425] synthesized spatially separated Pt and Pd modified $Ti_3C_2T_x$ (Pt=Pd/$Ti_3C_2T_x$) via a two-step loading process of metal NPs (Fig. 23d). They systematically studied the H_2 sensing performance of Pt=Pd/$Ti_3C_2T_x$ in comparison with monometallic $Ti_3C_2T_x$ (Pd-$Ti_3C_2T_x$ and Pt-$Ti_3C_2T_x$) as well as PdPt alloys modified $Ti_3C_2T_x$. As illustrated in Fig. 23e and f, the sensing performances of Pt=Pd/$Ti_3C_2T_x$ to H_2 are superior to that of other materials, including sensing response and t_{res}/t_{rec}. Researchers assumed that the improved sensing performance is ascribed to the enhanced electron transfer between the Pt and Pd metals via supported $Ti_3C_2T_x$, while the PtPd alloy formation may weaken the electron transfer[426]. Another strategy for enhancement of sensor performances is fabricating MXene-MOS composites by incorporation of the properties of MXenes and MOSs[427]. This approach enables tailoring of MXene/MOS interfacial structures and active sites, optimizing electron transfer dynamics and gas adsorption capabilities[428,429]. Chen et al.[427], reported H_2 sensors based on $Ti_3C_2T_x$-SnO_2 nanocomposite films (Fig. 23g). The SEM image of the composite in Fig. 23h unveiled that lamellar-structured MXenes were closely connected with hexagonal SnO_2 NSs, forming heterojunctions. Some of SnO_2 NSs were inserted between $Ti_3C_2T_x$ layers to expand the interlayer spacing of $Ti_3C_2T_x$, resulting in increasing active sites and enhancing gas adsorption kinetics[430]. From the response curve in Fig. 23i and j, by optimizing the amount of added MXene, t_{res}/t_{rec} were shortened to 11/13 s, and the sensor

Table 5 Summary of sensing properties of 2D material-based H_2 sensors

Material	T (°C)	detection range (ppm)	Tested concentration (ppm)	Response	t_{res} /t_{rec} (s)	Tested LOD (ppm)	Ref.
WS_2 NSs	RT	10–500	500	72.8%[b]	30/71	10	493
V_2CTx	RT	2–100	100	24.35%[a]	120/420	2	416
MoS_2	200	1000–200000	200000	170%[a]	NG/NG	1000	370
Pyramids like MoS_2 flakes	RT	1000–10000	10000	11.3%[a]	125.3/6	1000	365
sericin-MoS_2 NSs	RT	10–500	100	36.5%[a]	10/6	10	494
Pd/MoS_2	80	5–100	100	870%[b]	28/30	5	384
Pt/MoS_2	250	2.5–1000	1000	44000%[b]	NG/NG	2.5	394
Pt/MoS_2	RT	0.5–50	50	23.2%[a]	33/121	0.5	358
MoS_2/Pt	RT	500–40000	40000	12%[a]	2.7/16	500	396
Pd/Ti_3C_2Tx	RT	10–100	100	16.78%[a]	200/376	10	421
Pt=Pd/Ti_3C_2Tx	RT	1–20000	200	24.6%[a]	6/8	1	425
Zn-doped MoO_3-MoS_2	RT	5–1800	100	1682%[b]	31.3/14.8	5	401
CdS/PbS/SnO_2	200	0.05–100	100	1125.2%[a]	10.6/36.6	0.05	402
SnO_2/$SnSe_2$	100	5–100	100	270%[b]	3/19	5	408
In_2O_3/In_2Se_3	100	5–100	100	210%[b]	1240/NG	5	409
Ti_3C_2Tx-SnO_2	400	10–2000	600	53.71%[a]	11/13	10	427
$MoSe_2$-ZnO	RT	1–500	500	60%[b]	19.7/40.4	1	495
Pd-MoS_2/ MoO_3	100	10–1000	1000	3.3×10^7%[b]	379/304	10	387
Pd/SnS_2/SnO_2	300	100–10000	500	9500%[b]	1/9	100	361
Pd-SnO_2-TiO_2/ MXene	200	0.2–500	100	~978%[b]	6/9	0.2	431

[a] Refers $S = \Delta R/R_0$ or $\Delta R/R_g$; [b] refers $S = R_0/R_g$ or R_g/R_0

was able to detect a wide range of H_2 concentrations (10–2000 ppm). Leveraging the synergistic effect of metal NPs and MOSs, Zhang et al.[431] proposed a novel heterostructure composed of SnO_2-TiO_2/MXene decorated with Pd NPs. The gas sensor demonstrated a low LOD (200 ppb) and rapid t_{res}/t_{rec} (6/9 s) with a good linear response to H_2. In addition, machine learning techniques were adopted to further enhance the sensor's selectivity, which can improve the accuracy of gas identification in complex environments.

Table 5 summarized the sensing characteristics of recently reported 2D material-based H_2 sensors. In conclusion, 2D materials such as TMDs and MXenes, exhibit RT sensing performance due to their high surface-to-volume ratio and tunable electrical properties. However, the reliability and stability of pristine monolayer or few-layer 2D materials in practical settings remains constrained by their vulnerability to oxidative and humid conditions. This limitation becomes particularly pronounced within the harsh environment within a battery pack during Stage II of TR, where temperatures soar rapidly above 100 °C[50]. Therefore, more efforts are demanded for enhancing the stability of 2D material-based sensors within battery packs. Alternatively, employing wide-bandgap semiconductors presents another promising route. Compared to other materials, III-V semiconductors exhibit potential for H_2 sensing applications owing to their stable crystal structure and chemical bonding, which contribute to excellent chemical stability and resistance to degradation. This will be discussed in the following section.

Wide band-gap semiconductors-based chemiresistive H_2 sensor

Wide band-gap semiconductors, such as silicon carbide (SiC)[432] or III-nitride materials (GaN, InGaZnO, etc.)[433] have been widely used in silicon-based electronic devices ascribing to their chemical stability, high temperature/high power durability[434], and high electron mobility[435]. Through structure design and surface modification, wide band-gap semiconductors also possess application potential in the field of gas sensing. For instance, to increase specific surface area and adsorption sites, porous GaN honeycomb networks and GaN NW films have been developed for H_2 detection[436–439]. Shafa et al.[436] fabricated H_2 sensor based on porous GaN and investigated the effect

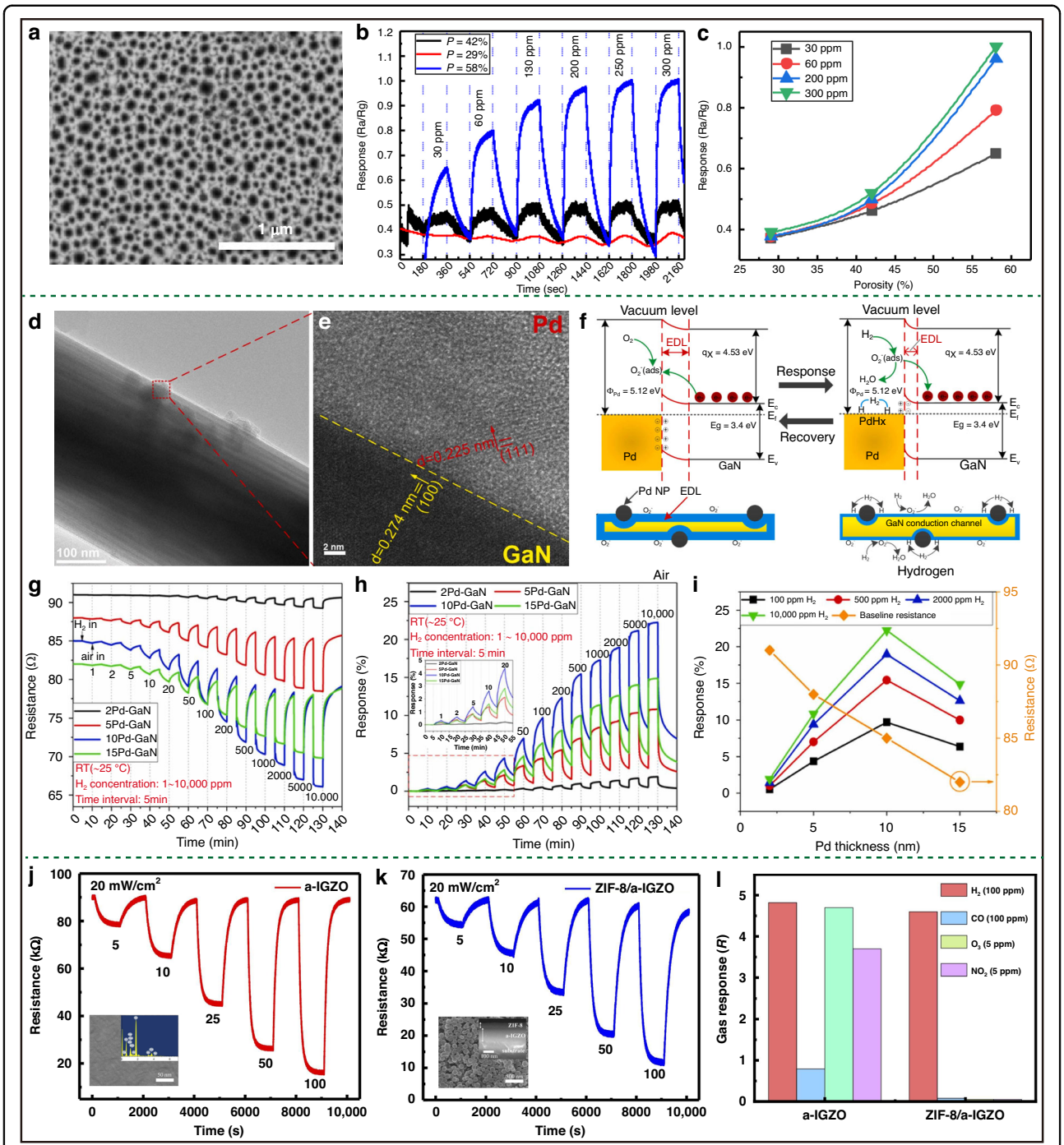

Fig. 24 H_2 sensors based on wide band-gap semiconductors. a SEM image of porous GaN structure; Effect of porosity on H_2 response at RT **b** versus time and **c** versus the porosity[436]. Copyright 2019, American Chemical Society. **d**, **e** HRTEM images and **F** the schematic diagram of H_2 sensing mechanism of Pd-GaN NW; Dynamic resistance **g** and response **h** curves of Pd-GaN to various H_2 concentrations (1–10,000 ppm); **i** Selectivity of Pd-GaN[441]. Copyright 2024, Elsevier. Dynamic response curves of a-IGZO films **j** without and **k** with a ZIF-8 film, and the insets show SEM images of corresponding materials; **l** Comparison between H_2 response of a-IGZO films without and with a ZIF-8 film toward H_2 and interfering gases[446]. Copyright 2024, Elsevier

of pore radius and density on H_2 sensing (Fig. 24a). According to the dynamic response curves in Fig. 24b, c, the higher porosity promoted H_2 diffusion, leading to enhanced sensitivity and improved utilization of inner sensitizer. However, similar to other sensing materials, pure wide band-gap materials also exhibit poor selectivity to H_2. To address this issue, there are two typical strategies: (i) noble metal functionalization; (ii) covering of

the top surface of sensing materials with physical or chemical filters. The method of decoration of noble metals, such as Pd and Pt, has been reported in many works[436,438,440,441]. Li et al.[441] fabricated Pd NPs decorated GaN NWs for enhanced H_2 sensing, as shown in Fig. 24d, e. In air, the decoration of Pd NPs promotes the adsorption of oxygen on the GaN NWs surface and the formation of Schottky barrier at Pd-GaN interface generates EDL with high resistance baseline. In H_2, a large resistance variation is induced via two mechanisms (Fig. 24f): the reaction of H_2 with adsorbed oxygen that releases electrons back to GaN, and electron transfer between PdH_x (formed by H_2 absorption in Pd) and GaN. Thus, the sensing response of Pd-GaN-based sensor to H_2 in a range of (0.1–10,000 ppm) was significantly enhanced via optimizing the thickness of deposited Pd film (Fig. 24g, h). Due to the high selectivity of Pd for H_2, the fabricated Pd/GaN sensor demonstrated a much higher response to H_2 than other interfering gases (Fig. 24i). However, it has been reported that CO, NO_x, and sulfuric compounds can poison noble metal catalysts (e.g., Pd)[46,442,443]. Therefore, filter layers with well-defined microporous structures are designed for selective H_2 detection by effectively blocking the diffusion of interfering gases owing to the different kinetic diameters between H_2 and other molecules[444,445]. To date, microporous polymer[46,324] polymer-derived ceramics[444], and metal-organic framework (MOF) membrane[321,446] have been used as filter materials. Huang et al.[446] fabricated amorphous IGZO (a-IGZO) films covered with a ZIF-8 membrane for H_2 sensing. Insets in the dynamic sensing curves of a-IGZO-based sensors without and with a ZIF-8 membrane are shown in Fig. 24j-l. Compared to a-IGZO based sensor, the sensing response of ZIF-8/a-IGZO shows a slightly decrease. Whereas, the sensor's responses to CO (100 ppm), O_3 (5 ppm), and NO_2 (5 ppm) were significantly suppressed after introducing a ZIF-8 membrane. This molecular sieving effect stems from the inherent properties of the ZIF-8 membrane, whose small pore size (0.34 nm) restricts the diffusion of gas molecules with larger kinetic diameters, such as CO (0.376 nm), O_3 (0.380 nm), and NO_2 (0.364 nm)[447,448]. Also, the sensor with a ZIF-8 membrane experiences a slight decrease of 8% in response after 600 cycles of operation and showed a long-term stability over a month. Moreover, due to their excellent compatibility with MEMS technology, many field-effect-transistor chemiresistive gas sensors based on III-V semiconductors have been reported to enhance their gas-sensing performance via gate modulation[449–451]. In general, though III–V semiconductors-based sensors did not exhibit ultrahigh sensitive toward H_2 compared with other conventional types of sensing material, they are still worthy investigation owing to their high compatibility with MEMS technology processes (Fig. 25a).

Challenges, outlook, and conclusions

The safety concerns associated with LIBs are garnering increasing attention. During TR process, a lot of heat and flammable/explosive gases are released. This can lead to LIB failure and even severe accidents, including fires and explosions. To date, various reports have confirmed that H_2 is the first gas released in comparison to other indicator gases such as CO, CO_2 and CH_4[39,40]. Hence, developing high-performance H_2 sensors for in-time and accurate detecting of the LIB status presents an effective strategy for early safety warning. In addition, with the development of green energy technologies, H_2 sensors play a crucial role in areas including H_2 transportation and storage. For practical applications, US DOE has established objectives for the advancement of H_2 sensor, which include achieving the t_{res}/t_{rec} within 1 s for $H_2 \geq 1\%$, a broad detection concentration range of 0.1–10%, and a lifespan exceeding 10 years[44]. Although some progress has been made in H_2 detection technology, current research still encounters some challenges that require further addressing in chemiresistive H_2 sensor:

(1) The sensing performance of H_2 need to be addressed. Given that H_2 gas can serve as an indicator for the formation of trace Li dendrites, it is essential to expand the detection range of H_2 to ppm levels or even ppb levels in order to accurately assess the conditions of LIB during their early stages[43]. While many H_2 sensors are capable of detecting H_2 at ppm levels, their sensing speed and selectivity often degrade for $H_2 < 0.1\%$. To our knowledge, such ultrafast sensing and recovery speed ($t_{res}/t_{rec} \leq 1$ s) has rarely been accomplished in the field of chemiresistive H_2 sensor. Regarding selectivity, although decorating the sensing materials with Pd is an effective strategy, it may experience catalyst poisoning, which greatly impacts the sensitivity, selectivity and stability of sensors. Furthermore, the sensing behavior of H_2 sensors in various humidity levels (0–95% RH) and temperatures (−40–85 °C) should be studied to ensure reliable operation in ambient conditions. To date, several reports have demonstrated that covering sensing materials with a layer of polymer or MOF, such as PMMA and ZIF-8, can provide protection against interfering gases and humidity due to molecular sieving effect[46,321]. However, the current methods do not consistently yield optimal results because the morphologies and operating temperatures of sensing materials vary significantly. Therefore, there is a pressing need for more reliable and universal strategies for designing sensing materials aimed at enhancing sensor selectivity for commercialization.

(2) The long-term stability of H_2 sensor is one of the most parameters for practical applications. It requires

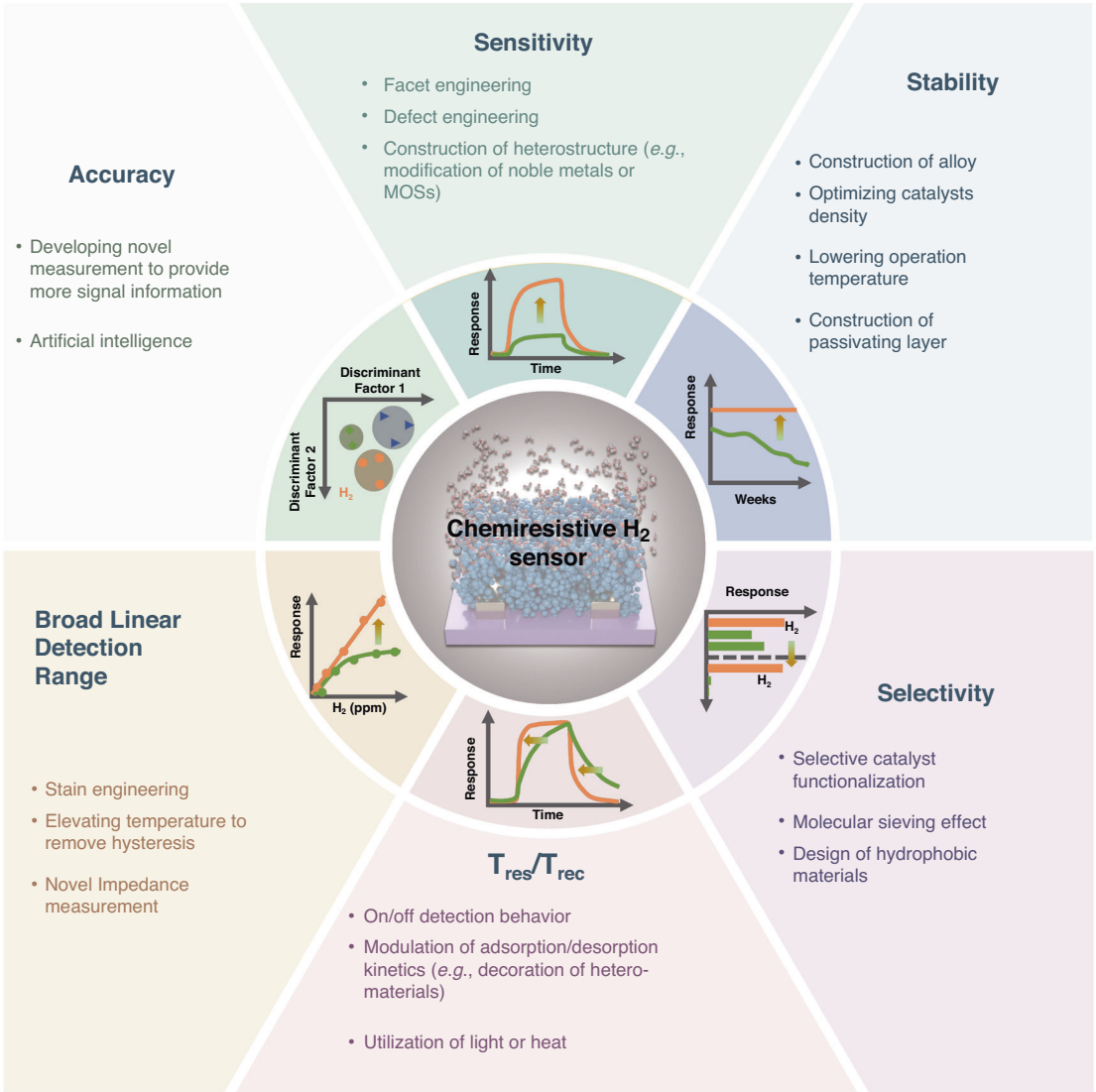

Fig. 25 Key factors and optimization strategies for gas sensing performance: an overview. Schematic graph of several strategies to improve sensor performance, including sensitivity, stability, selectivity, t_{res}/t_{rec}, broad linear detection range, and accuracy

that H_2 sensors operate reliable and stably without significant single drift over time. Currently, researchers primarily focus on enhancing sensitivity, linear detection range, response-recovery speed, and anti-interference ability of H_2 sensors. However, there is a relative lack of research concerning their long-term stability in real-world applications. Although several strategies have been proposed to improve sensor stability-such as use of Pd alloys[114], decrease of catalyst density[248], and passivation of the underlying TMDs via in-situ oxidization[408]—a comprehensive analysis of the failure mechanism remains insufficient. Thus, a deeper understanding of the failure mechanism of gas sensors is essential to provide a guidance for design of highly stable H_2 sensors.

(3) Exploring novel testing and analyzing strategies is also important for optimizing sensor performance. Conventional electronic chemiresistive gas sensors are designed to provide variations in resistance or current as an output in response to changes in gas concentrations. However, the non-linearity exhibited by chemiresistive sensors has been regarded as an intrinsic challenge, attributed to the power law that governs their direct current resistance response[452,453] This non-linear behavior adversely impacts the sensitivity of sensors at elevated gas concentrations and necessitates additional sensor calibration, thereby

increasing costs[454]. To address this problem, Potyrailo et al.[455] first proposed using an impedance measurement based on a dielectric excitation technique to detect signals from MOS-based sensors 2020. By varying frequencies, the impedance of SnO_2-based sensor showed a linear sensing behavior up to 10,000 ppm methane while its resistance response progressively saturated. Additionally, this approach significantly enhanced the stability of sensors against environmental conditions such as ambient humidity and temperature fluctuations. Similarly, using this measurement method can also enhance the performances of TMDs-based gas sensors, including linear detection range, high sensitivity, and stable baseline[456]. Recently, Zhang et al.[457] proposed a chemiresistive-potentiometric multivariate sensor aimed at improving its capability for discrimination gases by providing more signal information. Therefore, alongside designing sensing materials, innovative testing approaches may play an important role in enhancing H_2 sensing performance.

(4) In addition to emphasizing the performance of H_2 sensors themselves, the development of complementary technologies is equally crucial for practical TR monitoring. It is undeniable that the performance of H_2 sensors presents a vital factor in TR monitoring. However, nearly all reported H_2 sensors are currently evaluated under specific experimental conditions, which limits their practicality for accurate prediction and safety warning in real-world TR detection. Thus, the complicate internal conditions within LIB packs further exacerbate this challenge, making it difficult to assess LIB status accurately with data from a single H_2 under simulated conditions. Therefore, there is an urgent need for development of intelligent gas sensor arrays capable of processing data from sensor arrays using Artificial Intelligence technology to enhance predication accuracy[320,440,455,458]. In addition, although gas sensors offer superior response speed and stronger sensing abilities compared to temperature, pressure, and voltage sensors[32], the incorporation of multiple signals remains essential for presenting a comprehensive view of the LIB status, thereby improving safety warning systems.

In this review, the authors stress the importance of developing high-performance H_2 sensors with high sensitivity, fast response and recovery speed, high stability, and good selectivity to address the safety concerns of LIBs. To facilitate a comprehensive discussion on the current status of H_2 sensor development, we classified these sensors based on their sensing materials such as metals (e.g., Pd and Pd alloys), MOSs (single MOSs and MOS-based composites), carbons (CNTs, Gr, and GDY), 2D materials (TMDs and MXenes), and wide band-gap semiconductors. Within each material category, various strategies have been discussed to improve sensor performance. The primary methods for optimizing sensing properties include regulation of morphologies, doping/modification with metals, construction of heterojunctions, and designing of composites. These approaches effectively alter grain size, porosity, specific surface area, and reactivity of the sensing materials. Furthermore, the formed heterojunctions can enhance electron transfer characteristics between gases and materials, and increase the number of active adsorption sites. Moreover, owing to different underlying sensing mechanisms, there are several unique approaches to enhance their sensing properties. For instance, owing to the lattice expansion mechanism observed in Pd-based sensors, construction of nanogaps can greatly enhance their sensitivity and reduce their LOD with optimized width of nanogaps. Additionally, considering that slow oxidation may occur under mild operational conditions for 2D materials such as TMDs and MXenes, in-situ oxidation emerges as an effective method for constructing heterojunctions with MOSs while passivating the surface of 2D materials. This method improves both sensitivity and stability in H_2 sensors. To achieve a broad linear detection range, several strategies have been reported. These include the introduction of a buffer layer between the substrate and Pd to suppress phase transitions, as well as the application of heat to eliminate hysteresis. Furthermore, the development of novel measurement techniques has demonstrated significant potential for facilitating linear detection behavior. Therefore, to advance the development of high-performance H_2 sensors, it is imperative to establish a comprehensive understanding of the intrinsic response mechanisms and failure modes inherent in diverse sensing material systems. This understanding is vital for addressing key challenges in optimizing sensor sensitivity, stability, selectivity, and t_{res}/t_{res} for practical applications. Figure 25 summarizes some commonly used strategies in existing reports for enhancing sensor performance. Beside the inherent sensor performance, multi-signal information and Artificial Intelligence are needed to provide a reliable and accurate prediction of TR in the future.

Acknowledgements

L.L. and C.G. contributed equally to this work and should be considered co-first authors. The authors acknowledge the funding support from the Natural Science Foundation of Jiangsu Province (BK20230234, BK20243004, BK20221065), and the National Natural Science Foundation of China (Grant No. 62301553, 62125112, 62371448, 62204254, 62401563, 52203356), the Strategic Priority Research Program of the Chinese Academy of Science (XDB0520301), and Suzhou Municipal Bureau of Science & Technology (Grant No. ZXL2023339, SJC2023004).

Author details
[1]i-lab, Suzhou Institute of Nano-Tech and Nano-Bionics (SINANO), Chinese Academy of Sciences (CAS), Suzhou, Jiangsu, PR China. [2]School of Nano-Tech and Nano-Bionics, University of Science and Technology of China, Hefei, Anhui, PR China. [3]Department of Health and Environmental Sciences, Xi'an Jiaotong-Liverpool University, Suzhou, Jiangsu, PR China. [4]Key Laboratory of Efficient Low-carbon Energy Conversion and Utilization of Jiangsu Provincial Higher Education Institutions, School of Physical Science and Technology, Suzhou University of Science and Technology, Suzhou, PR China. [5]School of Integrated Circuits, Jiangnan University, Wuxi, Jiangsu, PR China. [6]Key Laboratory of Semiconductor Display Materials and Chips, Nano-X Vacuum Interconnected Workstation, Suzhou, Jiangsu, PR China

Competing interests
The authors declare no competing interests.

Received: 21 September 2025 Revised: 27 November 2025 Accepted: 22 December 2025
Published online: 25 March 2026

References

1. Noh, H.-J., Youn, S., Yoon, C. S. & Sun, Y.-K. Comparison of the structural and electrochemical properties of layered $Li[Ni_xCo_yMn_z]O_2$ (x = 1/3, 0.5, 0.6, 0.7, 0.8 and 0.85) cathode material for lithium-ion batteries. *J. Power Sources* **233**, 121–130 (2013).
2. Sun, Y.-K. et al. High-energy cathode material for long-life and safe lithium batteries. *Nat. Mater.* **8**, 320–324 (2009).
3. Zhao, W., Zhao, C., Wu, H., Li, L. & Zhang, C. Progress, challenge and perspective of graphite-based anode materials for lithium batteries: a review. *J. Energy Storage* **81**, 110409 (2024).
4. Wang, Q. et al. Thermal runaway caused fire and explosion of lithium ion battery. *J. Power Sources* **208**, 210–224 (2012).
5. Chen, S., Gao, Z. & Sun, T. Safety challenges and safety measures of li-ion batteries. *Energy Sci. Eng.* **9**, 1647–1672 (2021).
6. Rowden, B. & Garcia-Araez, N. A review of gas evolution in lithium ion batteries. *Energy Rep.* **6**, 10–18 (2020).
7. Mathieu, O. et al. Experimental investigation of the combustion properties of an average thermal runaway gas mixture from li-ion batteries. *Energ. Fuel.* **36**, 3247–3258 (2022).
8. Laura Sky Brown. Chevy expands bolt EV recall, adds bolt EUV, over battery fire risk. https://www.caranddriver.com/news/a34672772/chevrolet-bolt-ev-recall-battery/ (2021).
9. Yang, Y. et al. Towards a safer lithium-ion batteries: A critical review on cause, characteristics, warning and disposal strategy for thermal runaway. *Adv. Adv. Appl. Energy* **11**, 100146 (2023).
10. Zhang, Y. et al. Pathways to next-generation fire-safe alkali-ion batteries. *Adv. Sci.* **10**, 2301056 (2023).
11. Ren, D. et al. Investigating the relationship between internal short circuit and thermal runaway of lithium-ion batteries under thermal abuse condition. *Energy Storage Mater.* **34**, 563–573 (2021).
12. Feng, X. et al. Thermal runaway mechanism of lithium ion battery for electric vehicles: a review. *Energy Storage Mater.* **10**, 246–267 (2018).
13. Wen, J., Yu, Y. & Chen, C. A review on lithium-ion batteries safety issues: existing problems and possible solutions. *Mater. Express* **2**, 197–212 (2012).
14. Lamb, J., Orendorff, C. J., Steele, L. A. M. & Spangler, S. W. Failure propagation in multi-cell lithium ion batteries. *J. Power Sources* **283**, 517–523 (2015).
15. Lai, Y. et al. Lithium-ion battery safety warning methods review. *Energy Storage Sci. Technol.* **9**, 1926–1932 (2020).
16. Kong, D., Lv, H., Ping, P. & Wang, G. A review of early warning methods of thermal runaway of lithium ion batteries. *J. Energy Storage* **64**, 107073 (2023).
17. Nie, B., Dong, Y. & Chang, L. The evolution of thermal runaway parameters of lithium-ion batteries under different abuse conditions: A review. *J. Energy Storage* **96**, 112624 (2024).
18. Mei, W. et al. Operando monitoring of thermal runaway in commercial lithium-ion cells via advanced lab-on-fiber technologies. *Nat. Commun.* **14**, 5251 (2023).
19. Zhu, S. et al. A novel designed visualized li-ion battery for in-situ measuring the variation of internal temperature. *Extrem. Mech. Lett.* **37**, 100707 (2020).
20. Spinner, N. S. et al. Novel 18650 lithium-ion battery surrogate cell design with anisotropic thermophysical properties for studying failure events. *J. Power Sources* **312**, 1–11 (2016).
21. Drake, S. J. et al. Heat generation rate measurement in a li-ion cell at large C-rates through temperature and heat flux measurements. *J. Power Sources* **285**, 266–273 (2015).
22. Feinauer, M., Hölzle, M. & Waldmann, T. Insights into thermal runaway of cylindrical lithium-ion batteries by internal temperature sensors. *Electrochem. Soc. Interface* **33**, 51–54 (2024).
23. Fleming, J. et al. The design and impact of in-situ and operando thermal sensing for smart energy storage. *J. Energy Storage* **22**, 36–43 (2019).
24. Lee, C.-Y. et al. Integrated microsensor for real-time microscopic monitoring of local temperature, voltage and current inside lithium ion battery. *Sens. Actuators A: Phys.* **253**, 59–68 (2017).
25. Land, H. B. & Gammon, T. Addressing arc flash problems in low voltage switchboards: a case study in arc fault protection. In Proc. *IEEE/IAS 50th Industrial & Commercial Power Systems Technical Conference* 1–12 (IEEE, 2014). https://doi.org/10.1109/ICPS.2014.6839161.
26. Fortier, A., Tsao, M., Williard, N., Xing, Y. & Pecht, M. Preliminary study on integration of fiber optic Bragg grating sensors in li-ion batteries and in situ strain and temperature monitoring of battery cells. *Energies* **10**, 838 (2017).
27. Parekh, M. H. et al. In situ thermal runaway detection in lithium-ion batteries with an integrated internal sensor. *ACS Appl. Energy Mater.* **3**, 7997–8008 (2020).
28. Jia, Z. et al. The preload force effect on the thermal runaway and venting behaviors of large-format prismatic $LiFePO_4$ batteries. *Appl. Energy* **327**, 120100 (2022).
29. Kirchev, A., Guillet, N., Lonardoni, L., Dumenil, S. & Gau, V. Li-ion cell safety monitoring using mechanical parameters: Part II. Battery behavior during thermal abuse tests. *J. Electrochem. Soc.* **170**, 010503 (2023).
30. Huang, W. et al. Early warning of battery failure based on venting signal. *J. Energy Storage* **59**, 106536 (2023).
31. Wenger, M., Waller, R., Lorentz, V. R. H., März, M. & Herold, M. Investigation of gas sensing in large lithium-ion battery systems for early fault detection and safety improvement. In *Proc. IECON 2014-40th Annual Conference of the IEEE Industrial Electronics Society* 5654–5659. https://doi.org/10.1109/IECON.2014.7049366 (IEEE, 2014).
32. Koch, S., Birke, K. & Kuhn, R. Fast thermal runaway detection for lithium-ion cells in large scale traction batteries. *Batteries* **4**, 16 (2018).
33. Hammami, A., Raymond, N. & Armand, M. Runaway risk of forming toxic compounds. *Nature* **424**, 635–636 (2003).
34. Fu, Y. et al. An experimental study on burning behaviors of 18650 lithium ion batteries using a cone calorimeter. *J. Power Sources* **273**, 216–222 (2015).
35. Sun, J. et al. Toxicity, a serious concern of thermal runaway from commercial li-ion battery. *Nano Energy* **27**, 313–319 (2016).
36. Golubkov, A. W. et al. Thermal-runaway experiments on consumer li-ion batteries with metal-oxide and olivin-type cathodes. *RSC Adv.* **4**, 3633–3642 (2014).
37. Wang, Z., Zhu, L., Liu, J., Wang, J. & Yan, W. Gas sensing technology for the detection and early warning of battery thermal runaway: A review. *Energ. Fuel.* **36**, 6038–6057 (2022).
38. Hu, J. et al. Locking oxygen in lattice: A quantifiable comparison of gas generation in polycrystalline and single crystal Ni-rich cathodes. *Energy Storage Mater.* **47**, 195–202 (2022).
39. Yang, M. et al. Comprehensive analysis of gas production for commercial $LiFePO_4$ batteries during overcharge-thermal runaway. *J. Energy Storage* **72**, 108323 (2023).
40. Zhang, H. et al. Tracking gassing behavior in pouch cell by operando on-line electrochemical mass spectrometry. *J. Energy Chem.* **84**, 286–291 (2023).
41. Zhang, Q. et al. In situ raman investigation on gas components and explosion risk of thermal runaway emission from lithium-ion battery. *J. Energy Storage* **56**, 105905 (2022).
42. Wan, F. et al. High-sensitivity lithium-ion battery thermal runaway gas detection based on fiber-enhanced Raman spectroscopy. *IEEE Sens. J.* **23**, 6849–6856 (2023).
43. Jin, Y. et al. Detection of micro-scale Li dendrite via H_2 gas capture for early safety warning. *Joule* **4**, 1714–1729 (2020).

44. Energy Efficiency and Renewable Energy (EERE), Department of Energy. Multi-Year Research, Development, and Demonstration Plan, 576 2011—2020. Section 3.7 Hydrogen Safety, Codes and Standards. (2015).
45. Koo, W.-T. et al. Chemiresistive hydrogen sensors: fundamentals, recent advances, and challenges. *ACS Nano* **14**, 14284–14322 (2020).
46. Nugroho, F. A. A. et al. Metal-polymer hybrid nanomaterials for plasmonic ultrafast hydrogen detection. *Nat. Mater.* **18**, 489–495 (2019).
47. Baranov, A., Ivanov, I. & Karpova, E. Effects of flameless catalytic combustion of hydrogen on the parameters of catalytic sensors with platinum-group catalysts. *Sens. Mater.* **35**, 3585 (2023).
48. Occelli, C., Fiorido, T., Perrin-Pellegrino, C. & Seguin, J.-L. Sensors for anaerobic hydrogen measurement: a comparative study between a resistive PdAu based sensor and a commercial thermal conductivity sensor. *Int. J. Hydrog. Energy* **48**, 17729–17741 (2023).
49. Chiu, S.-W. & Tang, K.-T. Towards a chemiresistive sensor-integrated electronic nose: a review. *Sensors* **13**, 14214–14247 (2013).
50. Wang, X.-X., Li, Q.-T., Zhou, X.-Y., Hu, Y.-M. & Guo, X. Monitoring thermal runaway of lithium-ion batteries by means of gas sensors. *Sens. Actuators B Chem.* **411**, 135703 (2024).
51. Darmadi, I., Nugroho, F. A. A. & Langhammer, C. High-performance nanostructured palladium-based hydrogen sensors—current limitations and strategies for their mitigation. *ACS Sens* **5**, 3306–3327 (2020).
52. Pham, T. K. N. & Brown, J. J. Hydrogen sensors using 2-dimensional materials: a review. *ChemistrySelect* **5**, 7277–7297 (2020).
53. Lee, H., Kim, J., Moon, H. & Lee, W. Hydrogen gas sensors using palladium nanogaps on an elastomeric substrate. *Adv. Mater.* **33**, 2005929 (2021).
54. Standley, R. W., Steinback, M. & Satterthwaite, C. B. Superconductivity in PdHx(dx) from 0.2 K to 4 K. *Solid State Commun.* **31**, 801–804 (1979).
55. Manchester, F. D., San-Martin, A. & Pitre, J. M. The H-pd (hydrogen-palladium) system. *JPE* **15**, 62–83 (1994).
56. Papaconstantopoulos, D. A. & Klein, B. M. Superconductivity in the palladium-hydrogen system. *Phys. Rev. Lett.* **35**, 110–113 (1975).
57. Skoskiewicz, T. Superconductivity in the palladium-hydrogen and palladium-nickel-hydrogen systems. *Phys. Stat. Sol. (A)* **11**, K123–K126 (1972).
58. Radhakrishnan, T. S., Stritzker, B., Van Dongen, J. C. M. & Mydosh, J. A. Pair breaking of manganese in superconducting pd-H alloys. *Phys. Rev. B* **27**, 5800–5803 (1983).
59. Kim, T. et al. Drastic gas sensing selectivity in 2-dimensional MoS_2 nanoflakes by noble metal decoration. *ACS Nano* **17**, 4404–4413 (2023).
60. Viveka, N., Poornimadevi, C., Kala, C. P. & Thiruvadigal, D. J. DFT insights into the gas sensing properties of light platinum group metal (Ru, Rh & Pd) doped $MoSe_2$ monolayers. *Surf. Interfaces* **66**, 106579 (2025).
61. Graham, T. XVIII. On the absorption and dialytic separation of gases by colloid septa. *Philos. Trans. R. Soc.* **156**, 399–439 (1866).
62. Akiba, H. et al. Nanometer-size effect on hydrogen sites in palladium lattice. *J. Am. Chem. Soc.* **138**, 10238–10243 (2016).
63. Maeland, A. J. & Gibb, T. R. P. Jr. X-ray diffraction observations of the pd-H_2 system through the critical region 1. *J. Phys. Chem.* **65**, 1270–1272 (1961).
64. Machida, K. & Enyo, M. In-situ X-ray diffraction study of metal hydride formation in palladium and palladium-based alloy electrodes under cathodic hydrogen charging. *B. Chem. Soc. Jpn.* **62**, 415–418 (1989).
65. Kawasaki, A. et al. Change in the crystalline structure during the phase transition of the palladium-hydrogen system. *Phys. Chem. Chem. Phys.* **17**, 24783–24790 (2015).
66. Owen, E. A. & Williams, E. S. J. X-ray study of the hysteresis effect observed in the palladium-hydrogen system. *Proc. Phys. Soc.* **56**, 52–63 (1944).
67. Owen, E. A. & Jones, J. I. The palladium-hydrogen system. *Proc. Phys. Soc.* **49**, 603–610 (1937).
68. Li, X., Liu, Y., Hemminger, J. C. & Penner, R. M. Catalytically activated palladium@platinum nanowires for accelerated hydrogen gas detection. *ACS Nano* **9**, 3215–3225 (2015).
69. Hughes, R. C. & Schubert, W. K. Thin films of pd/ni alloys for detection of high hydrogen concentrations. *J. Appl. Phys.* **71**, 542–544 (1992).
70. Walter, E. C., Favier, F. & Penner, R. M. Palladium mesowire arrays for fast hydrogen sensors and hydrogen-actuated switches. *Anal. Chem.* **74**, 1546–1553 (2002).
71. Favier, F., Walter, E. C., Zach, M. P., Benter, T. & Penner, R. M. Hydrogen sensors and switches from electrodeposited palladium mesowire arrays. *Science* **293**, 2227–2231 (2001).
72. Shim, Y.-S. et al. Nanogap-controlled pd coating for hydrogen sensitive switches and hydrogen sensors. *Sens. Actuators B Chem.* **255**, 1841–1848 (2018).
73. Pak, Y. et al. Palladium nanoribbon array for fast hydrogen gas sensing with ultrahigh sensitivity. *Adv. Mater.* **27**, 6945–6952 (2015).
74. Yamauchi, M., Ikeda, R., Kitagawa, H. & Takata, M. Nanosize effects on hydrogen storage in palladium. *J. Phys. Chem. C* **112**, 3294–3299 (2008).
75. Yau, A., Harder, R. J., Kanan, M. W. & Ulvestad, A. Imaging the hydrogen absorption dynamics of individual grains in polycrystalline palladium thin films in 3D. *ACS Nano* **11**, 10945–10954 (2017).
76. Delmelle, R. et al. Effect of structural defects on the hydriding kinetics of nanocrystalline Pd thin films. *Int. J. Hydrog. Energy* **40**, 7335–7347 (2015).
77. Iwaoka, H., Arita, M. & Horita, Z. Hydrogen diffusion in ultrafine-grained palladium: Roles of dislocations and grain boundaries. *Acta Mater.* **107**, 168–177 (2016).
78. Langhammer, C., Zhdanov, V. P., Zorić, I. & Kasemo, B. Size-dependent kinetics of hydriding and dehydriding of Pd nanoparticles. *Phys. Rev. Lett.* **104**, 135502 (2010).
79. Li, Y. Hydrogen diffusion and solubility in palladium thin films. *Int. J. Hydrog. Energy* **21**, 281–291 (1996).
80. Baldi, A., Gonzalez-Silveira, M., Palmisano, V., Dam, B. & Griessen, R. Destabilization of the Mg-H system through elastic constraints. *Phys. Rev. Lett.* **102**, 226102 (2009).
81. Sachs, C. et al. Solubility of hydrogen in single-sized palladium clusters. *Phys. Rev. B* **64**, 075408 (2001).
82. Kim, K. R., Noh, J.-S., Lee, J. M., Kim, Y. J. & Lee, W. Suppression of phase transitions in Pd thin films by insertion of a Ti buffer layer. *J. Mater. Sci.* **46**, 1597–1601 (2011).
83. Cho, S.-Y. et al. Ultrasmall grained Pd nanopattern H_2 sensor. *ACS Sens* **3**, 1876–1883 (2018).
84. Kumar, A., Chen, K., Thundat, T. & Swihart, M. T. Paper-based hydrogen sensors using ultrathin palladium nanowires. *ACS Appl. Mater. Interfaces* **15**, 5439–5448 (2023).
85. Sytwu, K. et al. Visualizing facet-dependent hydrogenation dynamics in individual palladium nanoparticles. *Nano Lett.* **18**, 5357–5363 (2018).
86. Li, G. et al. Shape-dependent hydrogen-storage properties in pd nanocrystals: which does hydrogen prefer, octahedron (111) or cube (100)?. *J. Am. Chem. Soc.* **136**, 10222–10225 (2014).
87. Li, X. et al. Characterization and optimization of the H_2 sensing performance of Pd hollow shells. *Sens. Actuators B Chem.* **295**, 101–109 (2019).
88. Lee, J., Shim, W., Lee, E., Noh, J.-S. & Lee, W. Highly mobile palladium thin films on an elastomeric substrate: nanogap-based hydrogen gas sensors. *Angew. Chem. Int. Ed.* **50**, 5301–5305 (2011).
89. Park, S. Sensing performance of pd nanogap supported on an elastomeric substrate in a wide temperature range of −40 to 70 °C. *Sens. Actuators* **348** (2021).
90. Lee, J. et al. Cracked palladium films on an elastomeric substrate for use as hydrogen sensors. *Int. J. Hydrog. Energy* **37**, 7934–7939 (2012).
91. Jung, H., Jang, B., Kim, W., Noh, J.-S. & Lee, W. Ultra-sensitive, one-time use hydrogen sensors based on sub-10 nm nanogaps on an elastomeric substrate. *Sens. Actuators B Chem.* **178**, 689–693 (2013).
92. Jang, B., Kim, W., Song, M.-J. & Lee, W. Thermal stability of the sensing properties in H_2 sensors composed of Pd nanogaps on an Elastomeric Substrate. *Sens. Actuators B Chem.* **240**, 186–192 (2017).
93. Huck, W. T. S. et al. Ordering of spontaneously formed buckles on planar surfaces. *Langmuir* **16**, 3497–3501 (2000).
94. Yoo, P. J. & Lee, H. H. Morphological diagram for metal/polymer bilayer wrinkling: Influence of thermomechanical properties of polymer layer. *Macromolecules* **38**, 2820–2831 (2005).
95. Choi, W. M. et al. Biaxially stretchable "wavy" silicon nanomembranes. *Nano Lett.* **7**, 1655–1663 (2007).
96. Khang, D.-Y., Rogers, J. A. & Lee, H. H. Mechanical buckling: mechanics, metrology, and stretchable electronics. *Adv. Funct. Mater.* **19**, 1526–1536 (2009).
97. Won, C. et al. Ultrasensitive and stretchable conductive fibers using percolated Pd nanoparticle networks for multisensing wearable electronics: Crack-based strain and H_2 sensors. *ACS Appl. Mater. Interfaces* **12**, 45243–45253 (2020).
98. Son, W. et al. PdO-Nanoparticle-Embedded Carbon Nanotube Yarns for Wearable Hydrogen Gas Sensing Platforms with Fast and Sensitive Responses. *ACS Sens* **8**, 94–102 (2023).

99. Hassan, K. et al. Fast response hydrogen gas sensor based on Pd/Cr nanogaps fabricated by a single-step bending deformation. *Anal. Chim. Acta* **1138**, 49–58 (2020).
100. Pak, Y. et al. Highly stable and ultrafast hydrogen gas sensor based on 15 nm nanogaps switching in a palladium-gold nanoribbons array. *Adv. Mater. Interfaces* **6**, 1801442 (2019).
101. Cho, M. et al. Nanogap formation using a chromium oxide film and its application as a palladium hydrogen switch. *Langmuir* **38**, 1072–1078 (2022).
102. Lee, J., Shim, W., Noh, J.-S. & Lee, W. Design rules for nanogap-based hydrogen gas sensors. *ChemPhysChem* **13**, 1395–1403 (2012).
103. Zhao, M., Wong, M. H., Ong, C. W., Ng, N. H. & Man, H. C. Tunability of pd-nanogapped H_2 sensors made on SiO_2-coated Si micropillar arrays. *Sens. Actuators B Chem.* **255**, 944–951 (2018).
104. Kumar, A., Zhao, Y., Abraham, S. R., Thundat, T. & Swihart, M. T. Pd alloy nanosheet inks for inkjet-printable H_2 sensors on paper. *Adv. Mater. Interfaces* **9**, 2200363 (2022).
105. Mamatkulov, M. & Zhdanov, V. P. Partial or complete suppression of hysteresis in hydride formation in binary alloys of Pd with other metals. *J. Alloy. Compd.* **885**, 160956 (2021).
106. Machida, K. & Enyo, M. In situ X-ray diffraction study of hydrogen entry into Pd and Pd-au alloy electrodes during anodic HCHO oxidation. *J. Electrochem. Soc.* **134**, 1472–1474 (1987).
107. Luong, H. M. et al. Sub-second and ppm-level optical sensing of hydrogen using templated control of nano-hydride geometry and composition. *Nat. Commun.* **12**, 2414 (2021).
108. Ma, B., Yang, P., Jiang, C., Pan, Q. & Chen, C. Wafer-scale hysteresis-free plasmonic hydrogen sensors based on pd-au alloy nanoarrays. *Int. J. Hydrog. Energy* **48**, 31392–31399 (2023).
109. Bannenberg, L., Schreuders, H. & Dam, B. Tantalum-palladium: hysteresis-free optical hydrogen sensor over 7 orders of magnitude in pressure with sub-second response. *Adv. Funct. Mater.* **31**, 2010483 (2021).
110. Zhao, Z.-J. et al. 3D layer-by-layer pd-containing nanocomposite platforms for enhancing the performance of hydrogen sensors. *ACS Sens.* **5**, 2367–2377 (2020).
111. Song, L., Ahn, J., Kim, D.-H., Shin, H. & Kim, I.-D. Porous pd-sn alloy nanotube-based chemiresistor for highly stable and sensitive H_2 detection. *ACS Appl. Mater. Interfaces* **14**, 28378–28388 (2022).
112. Eadi, S. B. et al. Improved hydrogen gas sensing performance of pd-ni alloy thin films. *Int. J. Hydrog. Energy* **48**, 12534–12539 (2023).
113. Tian, J. et al. Zero drift suppression for PdNi nano-film hydrogen sensor by vacuum annealing. *Int. J. Hydrog. Energy* **45**, 14594–14601 (2020).
114. Liu, G. et al. High durability for PdNi nano-film hydrogen sensor. *Int. J. Hydrog. Energy* **50**, 1146–1156 (2024).
115. Kim, Y. J. et al. Highly durable chemoresistive micropatterned PdAu hydrogen sensors: performance and mechanism. *ACS Sens.* **9**, 5363–5373 (2024).
116. Jang, J.-S. et al. Hollow Pd-Ag composite nanowires for fast responding and transparent hydrogen sensors. *ACS Appl. Mater. Interfaces* **9**, 39464–39474 (2017).
117. Sharma, B. & Kim, J.-S. Pd/Ag alloy as an application for hydrogen sensing. *Int. J. Hydrog. Energy* **42**, 25446–25452 (2017).
118. Jo, M.-S. et al. Wireless and linear hydrogen detection up to 4% with high sensitivity through phase-transition-inhibited Pd nanowires. *ACS Nano* **16**, 11957–11967 (2022).
119. Jo, M.-S. et al. Ultrafast (∼0.6 s), robust, and highly linear hydrogen detection up to 10% using fully suspended pure Pd nanowire. *ACS Nano* **17**, 23649–23658 (2023).
120. Huang, T. et al. Ultrafast (0.3 s) integrated hydrogen leakage sensor system empowered by concentration prediction algorithm. *Chem. Eng. J.* **520**, 166395 (2025).
121. Yang, R. et al. Ultrafast hydrogen detection system using vertical thermal conduction structure and neural network prediction algorithm based on sensor response process. *ACS Sens* **10**, 2181–2190 (2025).
122. Conner, W. C. Jr. & Falconer, J. L. Spillover in heterogeneous catalysis. *Chem. Rev.* **95**, 759–788 (1995).
123. Li, Z. et al. Hydrogen gas sensor based on mesoporous In_2O_3 with fast response/recovery and ppb level detection limit. *Int. J. Hydrog. Energy* **43**, 22746–22755 (2018).
124. Batzill, M. & Diebold, U. The surface and materials science of tin oxide. *Prog. Surf. Sci.* **79**, 47–154 (2005).
125. Lee, J.-H. Gas sensors using hierarchical and hollow oxide nanostructures: overview. *Sens. Actuators B Chem.* **140**, 319–336 (2009).
126. Liu, L. et al. Heteronanostructural metal oxide-based gas microsensors. *Microsyst. Nanoeng.* **8**, 1–22 (2022).
127. Katoch, A., Choi, S.-W., Kim, H. W. & Kim, S. S. Highly sensitive and selective H_2 sensing by ZnO nanofibers and the underlying sensing mechanism. *J. Hazard. Mater.* **286**, 229–235 (2015).
128. Silva, W. S. et al. Hydrogen-induced metallization on the ZnO (0001) surface. *Phys. Rev. B* **98**, 155416 (2018).
129. Kumar, M. et al. Holey engineered 2D ZnO-nanosheets architecture for supersensitive ppm level H_2 gas detection at room temperature. *Sens. Actuators B Chem.* **326**, 128839 (2021).
130. Lupan, O. et al. Influence of CuO nanostructures morphology on hydrogen gas sensing performances. *Microelectron. Eng.* **164**, 63–70 (2016).
131. Han, X. et al. Synthesis of tin dioxide octahedral nanoparticles with exposed high-energy 221 facets and enhanced gas-sensing properties. *Angew. Chem. Int. Ed.* **48**, 9180–9183 (2009).
132. Qian, H. et al. Gas-phase synthesis of MoO_3 nanoclusters with helium-induced high energy (060) crystal facet: enhancing oxygen adsorption for improved gas-sensing. *Appl. Surf. Sci.* **657**, 159735 (2024).
133. Zhang, M. et al. Quasi-cubic hematite with exposed high-energy facets for ethanol gas detection. *J. Alloy. Compd.* **873**, 159667 (2021).
134. Miao, G.-Y., Chen, S.-S., Wang, Y.-J., Guo, Z. & Huang, X.-J. SnO_2 nanostructures exposed with various crystal facets for temperature-modulated sensing of volatile organic compounds. *ACS Appl. Nano Mater.* **5**, 10636–10644 (2022).
135. Wang, C. et al. Ethanol-sensing performance of tin dioxide octahedral nanocrystals with exposed high-energy {111} and {332} facets. *J. Mater. Chem. A* **2**, 10623 (2014).
136. Priya, M.J., P.P., Subha & Jayaraj, M.K. Facet-dependent gas sensing properties of metal oxide nanostructures. in *Nanomaterials for Sensing and Optoelectronic Applications* 1–25. https://doi.org/10.1016/B978-0-12-824008-3.00015-1. (Elsevier, 2022).
137. Zhao, K. et al. Effect of exposed facet determined the room-temperature ammonia gas sensing of Cu2O nanoparticles. *Appl. Surf. Sci.* **613**, 156008 (2023).
138. Ouyang, J., Pei, J., Kuang, Q., Xie, Z. & Zheng, L. Supersaturation-controlled shape evolution of α-Fe_2O_3 nanocrystals and their facet-dependent catalytic and sensing properties. *ACS Appl. Mater. Interfaces* **6**, 12505–12514 (2014).
139. Xu, J., Xue, Z., Qin, N., Cheng, Z. & Xiang, Q. The crystal facet-dependent gas sensing properties of ZnO nanosheets: Experimental and computational study. *Sens. Actuators B Chem.* **242**, 148–157 (2017).
140. Zhou, X. et al. Synergistic cooperation of rutile TiO_2 {002}, {101}, and {110} facets for hydrogen sensing. *ACS Appl. Mater. Interfaces* **10**, 28199–28209 (2018).
141. Li, X. et al. Comprehensively improved hydrogen sensing performance via constructing the facets homojunction in rutile TiO_2 hierarchical structure. *Sens. Actuators B Chem.* **350**, 130869 (2022).
142. Yan, W.-Y., Zhou, Q., Chen, X., Huang, X.-J. & Wu, Y.-C. C-doped and N-doped reduced graphene oxide/TiO_2 composites with exposed (0 0 1) and (1 0 1) facets controllably synthesized by a hydrothermal route and their gas sensing characteristics. *Sens. Actuators B Chem.* **230**, 761–772 (2016).
143. Zhou, S., Yan, W., Ling, M. & Liang, C. High-response H_2 sensing performances of ZnO nanosheets modulated by oxygen vacancies. *Inorg. Chem. Front.* **10**, 3255–3262 (2023).
144. Zhou, X. et al. Crystal-defect-dependent gas-sensing mechanism of the single ZnO nanowire sensors. *ACS Sens* **3**, 2385–2393 (2018).
145. Li, G. et al. Adjustment of oxygen vacancy states in ZnO and its application in ppb-level NO_2 gas sensor. *Sci. Bull.* **65**, 1650–1658 (2020).
146. Jing, Z. & Zhan, J. Fabrication and gas-sensing properties of porous ZnO nanoplates. *Adv. Mater.* **20**, 4547–4551 (2008).
147. Bai, W. et al. Hollow porous structures for improving the sensitivity of colorimetric array gas sensors. *Adv. Funct. Mater.* **34**, 2401421 (2024).
148. Huang, Y. et al. Atomically dispersed Ru-decorated TiO_2 nanosheets for thermally assisted solar-driven nitrogen oxidation into nitric oxide. *CCS Chem.* **4**, 1208–1216 (2022).
149. Wang, Z., Miao, J., Zhang, H., Wang, D. & Sun, J. Hollow cubic $ZnSnO_3$ with abundant oxygen vacancies for H_2S gas sensing. *J. Hazard. Mater.* **391**, 122226 (2020).
150. Shi, Y. et al. Tunable oxygen vacancies of cobalt oxides for efficient gas sensing application. *Sens. Actuators B Chem.* **350**, 130860 (2022).

151. Nan, H. et al. Strong photoluminescence enhancement of MoS_2 through defect engineering and oxygen bonding. *ACS Nano* **8**, 5738–5745 (2014).
152. Yu, Z. et al. Towards intrinsic charge transport in monolayer molybdenum disulfide by defect and interface engineering. *Nat. Commun.* **5**, 5290 (2014).
153. Luo, N. et al. Ultralow detection limit MEMS hydrogen sensor based on SnO_2 with oxygen vacancies. *Sens. Actuators B Chem.* **354**, 130982 (2022).
154. Marikutsa, A. V., Vorob´eva, N. A., Rumyantseva, M. N. & Gas´kov, A. M. Active sites on the surface of nanocrystalline semiconductor oxides ZnO and SnO_2 and gas sensitivity. *Russ. Chem. Bull.* **66**, 1728–1764 (2017).
155. Wang, X. et al. Oxygen vacancy defects engineering on Ce-doped α-Fe_2O_3 gas sensor for reducing gases. *Sens. Actuators B Chem.* **302**, 127165 (2020).
156. Sadeghzadeh-Attar, A. & Bafandeh, M. R. The effect of annealing temperature on the structure and optical properties of well-aligned 1D SnO_2 nanowires synthesized using template-assisted deposition. *CrystEngComm* **20**, 460–469 (2018).
157. Wang, Z. et al. The correlation between surface defects and the behavior of hydrogen adsorption over ZnO under UV light irradiation. *Catal. Sci. Technol.* **8**, 3260–3277 (2018).
158. Wang, Z. et al. Construction of ultra-fast hydrogen sensor for dissolved gas detection in oil-immersed transformers based on titanium dioxide quantum dots modified tin dioxide nanosheets. *Sens. Actuators B Chem.* **393**, 134141 (2023).
159. Bhati, V. S., Kumar, A., Valappil, M. O., Alwarappan, S. & Kumar, M. Phosphorene oxide quantum dots decorated ZnO nanostructure-based hydrogen gas sensor. *IEEE Sens. J.* **21**, 7283–7290 (2021).
160. Şennik, E., Çolak, Z., Kılınç, N. & Öztürk, Z. Z. Synthesis of highly-ordered TiO_2 nanotubes for a hydrogen sensor. *Int. J. Hydrog. Energy* **35**, 4420–4427 (2010).
161. Chen, K. et al. An excellent room-temperature hydrogen sensor based on titania nanotube-arrays. *Int. J. Hydrog. Energy* **37**, 13602–13609 (2012).
162. Lupan, O. et al. Highly sensitive and selective hydrogen single-nanowire nanosensor. *Sens. Actuators B Chem.* **173**, 772–780 (2012).
163. Li, Z. et al. Ultrathin boundary-less SnO_2 films with surface-activated two-dimensional nanograins enable fast and sensitive hydrogen gas sensing. *ACS Sens* **9**, 2653–2661 (2024).
164. Rahmani, M. B., Yaacob, M. H. & Sabri, Y. M. Hydrogen sensors based on 2D WO_3 nanosheets prepared by anodization. *Sens. Actuators B Chem.* **251**, 57–64 (2017).
165. Cho, I., Kang, K., Yang, D., Yun, J. & Park, I. Localized liquid-phase synthesis of porous SnO_2 nanotubes on MEMS platform for low-power, high performance gas sensors. *ACS Appl. Mater. Interfaces* **9**, 27111–27119 (2017).
166. Sankeshi, S., Bajaj, P., Sivasankaran, V. P., Sunkara, M. V. & Basak, P. Hierarchical self-assembly of SnO_2 nanoparticles into porous microspheres: Exceptionally selective ammonia sensing at ambient. *ACS Appl. Mater. Interfaces* **17**, 3757–3771 (2025).
167. Park, K. et al. Simultaneous electrical and defect engineering of nickel iron metal-organic-framework via co-doping of metalloid and non-metal elements for a highly efficient oxygen evolution reaction. *Chem. Eng. J.* **439**, 135720 (2022).
168. Yan, W. et al. MOF-derived porous hollow CO_3O_4@ZnO cages for high-performance MEMS trimethylamine sensors. *ACS Sens* **6**, 2613–2621 (2021).
169. Zhou, T., Zhang, R., Wang, Y. & Zhang, T. MOF-derived 1 D α-Fe_2O_3/$NiFe_2O_4$ heterojunction as efficient sensing materials of acetone vapors. *Sens. Actuators B Chem.* **281**, 885–892 (2019).
170. Bag, A. et al. A room-temperature operable and stretchable NO_2 gas sensor composed of reduced graphene oxide anchored with MOF-derived $ZnFe_2O_4$ hollow octahedron. *Sens. Actuators B Chem.* **346**, 130463 (2021).
171. Huang, X.-Y. et al. Metal-organic framework-derived trimetallic oxides with dual sensing functions for ethanol. *Nanoscale* **15**, 8181–8188 (2023).
172. Sui, N. et al. MIL-68 (in) and ZIF-8 assisted construction of n-n heterostructure for the effective sensing of trace-level ozone. *Sens. Actuators B Chem.* **380**, 133312 (2023).
173. He, J., Meng, H., Xu, Y. & Feng, L. Hollow mesoporous In_2O_3 derived from MIL-68 (in) for dual gas sensing of NO_2 and H_2. *Sens. Actuators B Chem.* **418**, 136336 (2024).
174. Barsan, N., Simion, C., Heine, T., Pokhrel, S. & Weimar, U. Modeling of sensing and transduction for p-type semiconducting metal oxide based gas sensors. *J. Electroceram.* **25**, 11–19 (2010).
175. Hübner, M. et al. Influence of humidity on CO sensing with p-type CuO thick film gas sensors. *Sens. Actuators B Chem.* **153**, 347–353 (2011).
176. Zhao, M., Nitta, R., Izawa, S., Yamaura, J. & Majima, Y. Nano-patterned CuO nanowire nanogap hydrogen gas sensor with voids. *Adv. Funct. Mater.* **35**, 2415971 (2025).
177. Volanti, D. P. et al. The role of hierarchical morphologies in the superior gas sensing performance of CuO-based chemiresistors. *Adv. Funct. Mater.* **23**, 1759–1766 (2013).
178. Yan, W., Luo, W. & Li, M. NiO nanoparticles-based gas sensors: A novel pulse-driven approach for enhanced and efficient hydrogen detection. *Int. J. Hydrog. Energy* **85**, 481–488 (2024).
179. Zhao, X. et al. MOF-derived pd-loaded CO_3O_4 array structure for efficient H_2 detection. *Int. J. Hydrog. Energy* **168**, 151069 (2025).
180. Zhang, Y. et al. Hydrogen sensor for LIB thermal runaway based on ag-bi-modified CO_3 O_4 nanosheets: experimental and DFT calculation. *IEEE Sens. J.* **25**, 12599–12608 (2025).
181. Shah, S. et al. ppb-level H_2 gas-sensor based on porous ni-MOF derived NiO@CuO nanoflowers for superior sensing performance. *Mater. Res. Bull.* **180**, 113021 (2024).
182. Mei, H. et al. Overcoming selectivity challenges in single gas sensor leveraging temperature modulation and multi-feature fusion. *Chem. Eng. J.* **522**, 167722 (2025).
183. Luo, W., Dai, F., Liu, Y., Wang, X. & Li, M. Pulse-driven MEMS gas sensor combined with machine learning for selective gas identification. *Microsyst. Nanoeng.* **11**, 72 (2025).
184. Mei, H., Zhang, F., Zhou, T. & Zhang, T. Pulse-driven MEMS NO_2 sensors based on hierarchical In_2O_3 nanostructures for sensitive and ultra-low power detection. *Sensors* **24**, 7188 (2024).
185. Li, M., Luo, W. & Yan, W. High performance H_2 sensors based on NiO-SnO_2 nanosheets in temperature-pulsed operation mode. *Smart Mater. Struct.* **33**, 06LT01 (2024).
186. Ai, T. et al. High-performance H_2 gas sensor based on mn-doped α-Fe_2O_3 polyhedrons from N, N-dimethylformamide assisted hydrothermal synthesis. *Int. J. Hydrog. Energy* **47**, 20561–20571 (2022).
187. Li, J. et al. Essential role of lattice oxygen in hydrogen sensing reaction. *Nat. Commun.* **15**, 2998 (2024).
188. Kim, S., Singh, G., oh, M. & Lee, K. An analysis of a highly sensitive and selective hydrogen gas sensor based on a 3D cu-doped SnO_2 sensing material by efficient electronic sensor interface. *ACS Sens* **6**, 4145–4155 (2021).
189. Ferlazzo, A., Espro, C., Iannazzo, D., Moulaee, K. & Neri, G. A novel yttria-doped ZrO_2 based conductometric sensor for hydrogen leak monitoring. *Int. J. Hydrog. Energy* **47**, 9819–9828 (2022).
190. Singh, G., Virpal & Singh, R. C. Highly sensitive gas sensor based on er-doped SnO_2 nanostructures and its temperature dependent selectivity towards hydrogen and ethanol. *Sens. Actuators B Chem.* **282**, 373–383 (2019).
191. Yao, L. et al. Si doped highly crystalline mesoporous In_2O_3 nanowires: synthesis, characterization and ultra-high response to NOx at room temperature. *RSC Adv.* **5**, 15515–15523 (2015).
192. Xu, J. et al. In-situ La doped CO_3O_4 as highly efficient photocatalyst for solar hydrogen generation. *Int. J. Hydrog. Energy* **43**, 8674–8682 (2018).
193. Chrétien, S. & Metiu, H. Hydrogen dissociative adsorption on lanthana: Polaron formation and the role of acid-base interactions. *J. Phys. Chem. C* **119**, 19876–19882 (2015).
194. Li, Z. et al. La3+ doped SnO_2 nanofibers for rapid and selective H_2 sensor with long range linearity. *Int. J. Hydrog. Energy* **44**, 8659–8668 (2019).
195. Zhu, L., Zeng, W. & Li, Y. A non-oxygen adsorption mechanism for hydrogen detection of nanostructured SnO_2 based sensors. *Mater. Res. Bull.* **109**, 108–116 (2019).
196. Li, W. et al. Enhanced NO_2 sensing performance of S-doped biomorphic SnO_2 with increased active sites and charge transfer at room temperature. *Inorg. Chem. Front.* **7**, 2031–2042 (2020).
197. Wang, M.-D. et al. Synthesis of three-dimensionally ordered macro/mesoporous C-doped WO_3 materials: Effect of template sizes on gas sensing properties. *Sens. Actuators B Chem.* **288**, 656–666 (2019).
198. Güntner, A. T., Righettoni, M. & Pratsinis, S. E. Selective sensing of NH_3 by si-doped α-MoO_3 for breath analysis. *Sens. Actuators B Chem.* **223**, 266–273 (2016).
199. Raghu, A. V., Karuppanan, K. K. & Pullithadathil, B. Controlled carbon doping in anatase TiO_2 (101) facets: superior trace-level ethanol gas sensor performance and adsorption kinetics. *Adv. Mater. Interfaces* **6**, 1801714 (2019).

200. Li, H. et al. Waste honeycomb in-situ derived N-doped TiO_2 with hierarchical porous nanostructure for rapid and selective H_2 detection. *J. Alloy. Compd.* **1016**, 179016 (2025).
201. Qin, Y., Zhang, Y., Qiu, P. & Lei, S. SnO_2-CO_3O_4 nanocomposite sensor: achieving ultra-selective hydrogen detection in mixed gas environments. *Sens. Actuators B Chem.* **422**, 136521 (2025).
202. Yin, X.-T. et al. Ultra-high selectivity of H_2 over CO with a p-n nanojunction based gas sensors and its mechanism. *Sens. Actuators B Chem.* **319**, 128330 (2020).
203. Yao, Z. et al. Opposite sensing response of H_2 and CO on In_2O_3—CO_3O_4 nanocomposite-based gas sensors over a wide temperature range. *Sens. Actuators B Chem.* **433**, 137511 (2025).
204. Zhu, S. et al. Highly sensitive and stable H_2 gas sensor based on p-PdO-n-WO_3-heterostructure-homogeneously-dispersing thin film. *Int. J. Hydrog. Energy* **47**, 17821–17834 (2022).
205. Wu, J. et al. Ultrafast response and recovery in advanced H_2 sensing: self-assembled fruit-leaf-like PdO/WO_3 nanostructures. *Sens. Actuators B Chem.* **430**, 137339 (2025).
206. Ding, W., Ansari, N., Yang, Y. & Bachagha, K. Superiorly sensitive and selective H_2 sensor based on p-n heterojunction of WO_3-CoO nanohybrids and its sensing mechanism. *Int. J. Hydrog. Energy* **46**, 28823–28837 (2021).
207. Nie, S. et al. Insights into selective mechanism of NiO-TiO_2 heterojunction to H_2 and CO. *ACS Sens.* **8**, 4121–4131 (2023).
208. Yin, X.-T. et al. Opposite sensing response of heterojunction gas sensors based on SnO_2-Cr2O_3 nanocomposites to H_2 against CO and its selectivity mechanism. *Langmuir* **37**, 13548–13558 (2021).
209. Yin, X.-T. et al. Gas sensing selectivity of SnO_2-xNiO sensors for homogeneous gases and its selectivity mechanism: experimental and theoretical studies. *Sens. Actuators A Phys.* **354**, 114273 (2023).
210. Guo, M. et al. MEMS sensor based on MOF-derived WO_3-C/In_2O_3 heterostructures for hydrogen detection. *Sens. Actuators B Chem.* **398**, 134151 (2024).
211. Song, Z. et al. In-situ synthesis of needle-like PdO-decorated NiO thin films on Al_2O_3 substrates for high-performance H_2 sensors. *Ceram. Int.* **48**, 31746–31754 (2022).
212. Motaung, D. E. et al. Ultra-high sensitive and selective H_2 gas sensor manifested by interface of n-n heterostructure of CeO_2-SnO_2 nanoparticles. *Sens. Actuators B Chem.* **254**, 984–995 (2018).
213. Beatriceveena, T. V. & Gnanasekar, K. I. Highly sensitive and wide range hydrogen sensor based on thin films of $AgInO_2$ by pulsed laser deposition. *Sens. Actuators B Chem.* **383**, 133599 (2023).
214. Azmoodeh, Z., Milani Moghaddam, H. & Nasirian, S. Hydrogen gas sensing feature of polypyrrole nanofibers assisted by spinel $ZnMn2O_4$ microspheres in dynamic conditions. *Int. J. Hydrog. Energy* **47**, 29971–29984 (2022).
215. Li, Q. et al. Controllable fabrication of PdO-PdAu ternary hollow shells: synergistic acceleration of H_2-sensing speed via morphology regulation and electronic structure modulation. *Small* **18**, 2106874 (2022).
216. Kafil, V. et al. Review of noble metal and metal-oxide-semiconductor based chemiresistive hydrogen sensors. *Sens. Actuators A Phys.* **373**, 115440 (2024).
217. Cai, Z., Park, J. & Park, S. Synergistic effect of pd and Fe_2O_3 nanoparticles embedded in porous NiO nanofibers on hydrogen gas detection: fabrication, characterization, and sensing mechanism exploration. *Sens. Actuators B Chem.* **388**, 133836 (2023).
218. Zhang, Z. et al. Wafer-level manufacturing of MEMS H_2 sensing chips based on pd nanoparticles modified SnO_2 film patterns. *Adv. Sci.* **10**, 2302614 (2023).
219. Wei, J. et al. In situ raman monitoring and manipulating of interfacial hydrogen spillover by precise fabrication of au/TiO_2/pt sandwich structures. *Angew. Chem. Int. Ed.* **59**, 10343–10347 (2020).
220. Lee, J. et al. How pt influences H_2 reactions on high surface-area pt/CeO_2 powder catalyst surfaces. *JACS Au* **3**, 2299–2313 (2023).
221. Jenkinson, K. et al. Direct operando visualization of metal support interactions induced by hydrogen spillover during CO_2 hydrogenation. *Adv. Mater.* **35**, 2306447 (2023).
222. Beck, A. et al. The extent of platinum-induced hydrogen spillover on cerium dioxide. *ACS Nano* **17**, 1091–1099 (2023).
223. Li, H. et al. Operando unveiling of hydrogen spillover mechanisms on tungsten oxide surfaces. *J. Am. Chem. Soc.* **147**, 6472–6479 (2025).
224. Gu, F. et al. Atomically dispersed pt (II) on WO_3 for highly selective sensing and catalytic oxidation of triethylamine. *Appl. Catal. B Environ.* **256**, 117809 (2019).
225. Zheng, L. et al. Unveiling the electronic interaction in ZnO/PtO/pt nanoarrays for catalytic detection of triethylamine with ultrahigh sensitivity. *ACS Appl. Mater. Interfaces* **12**, 46267–46276 (2020).
226. Zhu, M. et al. Chemoresistive gas sensors based on noble-metal-decorated metal oxide semiconductors for H_2 detection. *Materials* **18**, 451 (2025).
227. Meng, X., Bi, M., Xiao, Q. & Gao, W. Ultra-fast response and highly selectivity hydrogen gas sensor based on pd/SnO_2 nanoparticles. *Int. J. Hydrog. Energy* **47**, 3157–3169 (2022).
228. Geng, X. et al. Ultrafast metal oxide reduction at Pd/PdO_2 interface enables one-second hydrogen gas detection under ambient conditions. *Nano Res.* **16**, 1149–1157 (2023).
229. Li, Z. et al. Direct methane activation by atomically thin platinum nanolayers on two-dimensional metal carbides. *Nat. Catal.* **4**, 882–891 (2021).
230. Xi, J. et al. Synthesis strategies, catalytic applications, and performance regulation of single-atom catalysts. *Adv. Funct. Mater.* **31**, 2008318 (2021).
231. Koga, K. Electronic and catalytic effects of single-atom pd additives on the hydrogen sensing properties of CO_3O_4 nanoparticle films. *ACS Appl. Mater. Interfaces* **12**, 20806–20823 (2020).
232. Wan, J. et al. Defect effects on TiO_2 nanosheets: Stabilizing single atomic site Au and promoting catalytic properties. *Adv. Mater.* **30**, 1705369 (2018).
233. Jung, G. et al. Reconfigurable manipulation of oxygen content on metal oxide surfaces and applications to gas sensing. *ACS Nano* **17**, 17790–17798 (2023).
234. Qiao, B. et al. Single-atom catalysis of CO oxidation using Pt_1/FeO_x. *Nat. Chem.* **3**, 634–641 (2011).
235. Zhang, S., Chang, X., Zhou, L., Liu, X. & Zhang, J. Stabilizing single-atom Pt on Fe_2O_3 nanosheets by constructing oxygen vacancies for ultrafast H_2 sensing. *ACS Sens* **9**, 2101–2109 (2024).
236. Guo, Y. et al. Mechanistic modeling and experimental demonstration of pd-catalyzed dual-gate TeSeO FET hydrogen sensors. *Sens. Actuators B Chem.* **447**, 138779 (2026).
237. Ma, R.-J. et al. Bimetallic pt-au nanocatalysts decorated In_2O_3 nests composed of ultrathin nanosheets for type 1 diabetes diagnosis. *Sens. Actuators B Chem.* **270**, 247–255 (2018).
238. Li, G. et al. PdPt bimetal-functionalized SnO_2 nanosheets: controllable synthesis and its dual selectivity for detection of carbon monoxide and methane. *ACS Appl. Mater. Interfaces* **11**, 26116–26126 (2019).
239. Badie, C. et al. Selective detection of H_2 gas in gas mixtures using NiO-shelled pd-decorated ZnO nanowires. *Adv. Mater. Technol.* **9**, 2302081 (2024).
240. Yuan, Z., Jin, J., Zhu, H., Zhang, H. & Meng, F. Ag-modified CO_3O_4-In_2O_3 nanohollow microspheres for H_2 detection. *IEEE Sens. J.* **24**, 25299–25307 (2024).
241. Meng, X., Bi, M. & Gao, W. Rapid response hydrogen sensor based on pd@pt/SnO_2 hybrids at near-ambient temperature. *Sens. Actuators B Chem.* **370**, 132406 (2022).
242. Li, Y. et al. Inhibiting emulative oxygen adsorption via introducing pt-segregated sites into the pd surface for enhanced H_2 sensing in air. *ACS Sens.* **9**, 5405–5413 (2024).
243. Zhou, L. et al. PdRh-sensitized iron oxide ultrathin film sensors and mechanistic investigation by operando TEM and DFT calculation. *Small* **19**, 2301485 (2023).
244. Kozhukhova, A. E., Du Preez, S. P. & Bessarabov, D. G. Development of Pt-Co/Al_2O_3 bimetallic catalyst and its evaluation in catalytic hydrogen combustion reaction. *Int. J. Hydrog. Energy* **51**, 1079–1096 (2024).
245. Cai, H. et al. Multishell SnO_2 hollow microspheres loaded with bimetal PdPt nanoparticles for ultrasensitive and rapid formaldehyde MEMS sensors. *ACS Sens* **7**, 1484–1494 (2022).
246. Meng, X., Bi, M., Xiao, Q. & Gao, W. Rapid detection of low concentration H_2 using au@pd/SnO_2 nanocomposites. *Sens. Actuators B Chem.* **366**, 131971 (2022).
247. Zhao, X. et al. Decorating pd-au nanodots around porous In_2O_3 nanocubes for tolerant H_2 sensing against switching response and H_2S poisoning. *Small* **20**, 2311840 (2024).
248. Wang, X. et al. In situ TEM technique revealing the deactivation mechanism of bimetallic Pd-Ag nanoparticles in hydrogen sensors. *Nano Lett.* **22**, 3157–3164 (2022).
249. Nair, K. G., Vishnuraj, R. & Pullithadathil, B. Highly sensitive, flexible H_2 gas sensors based on less platinum bimetallic Ni-Pt nanocatalyst-functionalized carbon nanofibers. *ACS Appl. Electron. Mater.* **3**, 1621–1633 (2021).

250. Jia, P. et al. High-efficient and selective hydrogen gas sensor based on bimetallic Ag/Cu nanoparticles decorated on In_2O_3: experimental and DFT calculation. *Int. J. Hydrog. Energy* **101**, 15–25 (2025).
251. Li, A. et al. The role of AuSn alloys in optimizing SnO_2 nanospheres for chemoresistive hydrogen sensing. *Sens. Actuators B: Chem.* **427**, 137214 (2025).
252. Meng, J. et al. Triboelectric nanogenerator enhanced schottky nanowire sensor for highly sensitive ethanol detection. *Nano Lett.* **20**, 4968–4974 (2020).
253. Meng, X., Bi, M. & Gao, W. Shape and composition effects of PdPt bimetallic nanocrystals on hydrogen sensing properties of SnO_2-based sensors. *Sens. Actuators B Chem.* **390**, 133976 (2023).
254. Cai, H. et al. Kinetics-driven dual hydrogen spillover effects for ultrasensitive hydrogen sensing. *Small* **19**, 2302652 (2023).
255. Hu, K., Wang, F., Shen, Z., Liu, H. & Xiong, J. Ternary heterojunctions synthesis and sensing mechanism of pd/ZnO-SnO_2 hollow nanofibers with enhanced H_2 gas sensing properties. *J. Alloy. Compd.* **850**, 156663 (2021).
256. Xing, Q., Cai, Y. & Zhang, M. A sub-second response/recovery hydrogen sensor based on multifunctional palladium oxide modified heterojunctions. *Sens. Actuators B: Chem.* **401**, 134956 (2024).
257. Goudah, G., Suliman, S. M. A. & Elfaki, E. A. Carbon nanotubes: Challenges and opportunities. In *Proc. International Conference on Computing, Electrical and Electronic Engineering (ICCEEE)* 74–81. https://doi.org/10.1109/ICCEEE.2013.6633910 (IEEE, 2013).
258. Huang, X. et al. Flexible Gas Sensors Based on Carbon Nanotube Hybrid Films: A Review. *Adv. Mater. Technol.* 2300616. https://doi.org/10.1002/admt.202300616. (2023).
259. Llobet, E. Gas sensors using carbon nanomaterials: a review. *Sens. Actuators B: Chem.* **179**, 32–45 (2013).
260. Armano, A. & Agnello, S. Two-Dimensional Carbon: A Review Of Synthesis Methods, And Electronic, Optical, And Vibrational Properties Of Single-layer Graphene. *C* **5**, 67 (2019).
261. Zhang, T., Mubeen, S., Myung, N. V. & Deshusses, M. A. Recent progress in carbon nanotube-based gas sensors. *Nanotechnol* **19**, 332001 (2008).
262. Wu, W. et al. Wafer-scale synthesis of graphene by chemical vapor deposition and its application in hydrogen sensing. *Sens. Actuators B Chem.* **150**, 296–300 (2010).
263. Sundaram, R. S., Gómez-Navarro, C., Balasubramanian, K., Burghard, M. & Kern, K. Electrochemical modification of graphene. *Adv. Mater.* **20**, 3050–3053 (2008).
264. Saravanan, A., Huang, B.-R. & Kathiravan, D. Surface and interface properties of monolayer graphene on hydrophobic and hydrophilic ultrananocrystalline diamond structures for hydrogen sensing applications. *Int. J. Hydrog. Energy* **47**, 4959–4969 (2022).
265. Liu, B. et al. Development of an ALD-Pt@SWCNT/graphene 3D nanohybrid architecture for hydrogen sensing. *ACS Appl. Mater. Interfaces* **12**, 53115–53124 (2020).
266. Li, G. et al. Mechanism of sensitivity enhancement of a ZnO nanofilm gas sensor by UV light illumination. *ACS Sens.* **4**, 1577–1585 (2019).
267. Ansón, A. et al. Porosity, surface area, surface energy, and hydrogen adsorption in nanostructured carbons. *J. Phys. Chem. B* **108**, 15820–15826 (2004).
268. Guo, S.-Y. et al. Transparent and flexible hydrogen sensor based on semiconducting single-wall carbon nanotube networks. *Carbon* **151**, 156–159 (2019).
269. Zhang, Y., Rhee, K. Y., Hui, D. & Park, S.-J. A critical review of nanodiamond based nanocomposites: synthesis, properties and applications. *Compos. Part B Eng.* **143**, 19–27 (2018).
270. Huang, B.-R., Kathiravan, D., Saravanan, A. & Mai, P.-H. Crystalline nanodiamond-induced formation of carbon nanotubes for stable hydrogen sensing. *ACS Appl. Nano Mater.* **4**, 2840–2848 (2021).
271. Saravanan, A., Huang, B.-R. & Kathiravan, D. Hierarchical morphology and hydrogen sensing properties of N_2-based nanodiamond materials produced through CH4/H_2/Ar plasma treatment. *Appl. Surf. Sci.* **457**, 367–375 (2018).
272. Wu, Y. et al. Highly sensitive and selective gas sensor using heteroatom doping graphdiyne: a DFT study. *Adv. Elect. Mater.* **7**, 2001244 (2021).
273. Tran, K. M. et al. Ultrasensitive carbon monoxide gas sensor at room temperature using fluorine-graphdiyne. *ACS Appl. Mater. Interfaces* **15**, 56084–56094 (2023).
274. Chen, X. et al. High-efficient physical adsorption and detection of formaldehyde using Sc- and Ti-decorated graphdiyne. *Phys. Lett. A* **381**, 879–885 (2017).
275. Wang, R., Cheng, B. & Ou, W. Intrinsic and Ag-doped graphdiyne as a two-dimensional material gas sensing detector for the detection of SF6 decomposition products. *Appl. Surf. Sci.* **608**, 155276 (2023).
276. Zhu, Z. et al. Antibacterial activity of graphdiyne and graphdiyne oxide. *Small* **16**, 2001440 (2020).
277. Dang, X. & Zhao, H. Graphdiyne: a promising 2D all-carbon nanomaterial for sensing and biosensing. *TrAC Trends Anal. Chem.* **137**, 116194 (2021).
278. Nam, Y. T. et al. Rapid and reversible sensing performance of hydrogen-substituted graphdiyne. *ACS Sens* **8**, 1151–1160 (2023).
279. Huang, Y. et al. SnS_2 Quantum dot-based optoelectronic flexible sensors for ultrasensitive detection of NO 2 down to 1 ppb. *ACS Appl. Mater. Interfaces* **12**, 25178–25188 (2020).
280. Eom, T. H. et al. Substantially improved room temperature NO 2 sensing in 2-dimensional SnS_2 nanoflowers enabled by visible light illumination. *J. Mater. Chem. A* **9**, 11168–11178 (2021).
281. Pham, T., Li, G., Bekyarova, E., Itkis, M. E. & Mulchandani, A. MoS_2-based optoelectronic gas sensor with sub-parts-per-billion limit of NO_2 gas detection. *ACS Nano* **13**, 3196–3205 (2019).
282. Guo, J., Zhang, D., Li, T., Zhang, J. & Yu, L. Green light-driven acetone gas sensor based on electrospinned CdS nanospheres/Co_3O_4 nanofibers hybrid for the detection of exhaled diabetes biomarker. *J. Colloid Interf. Sci.* **606**, 261–271 (2022).
283. Kumar, R. R. et al. Sulfur monovacancies in liquid-exfoliated MoS_2 nanosheets for NO_2 gas sensing. *ACS Appl. Nano Mater.* **4**, 9459–9470 (2021).
284. Waclawik, E. R. et al. Functionalised zinc oxide nanowire gas sensors: Enhanced NO_2 gas sensor response by chemical modification of nanowire surfaces. *Beilstein J. Nanotechnol.* **3**, 368–377 (2012).
285. Joshi, N. et al. A review on chemiresistive room temperature gas sensors based on metal oxide nanostructures, graphene and 2D transition metal dichalcogenides. *Microchim. Acta* **185**, 213 (2018).
286. Tian, H., Fan, H., Dong, G., Ma, L. & Ma, J. NiO/ZnO p-n heterostructures and their gas sensing properties for reduced operating temperature. *RSC Adv.* **6**, 109091–109098 (2016).
287. Tsuruta, A. et al. Gas Sensing Properties of High-purity semiconducting single-walled carbon nanotubes for NH_3, H_2, and NO. *ECS J. Solid State Sci. Technol.* **10**, 121004 (2021).
288. Park, J., Jang, I. & Kim, H. J. Crumpled carbon nanotube thin film heaters for high sensitivity hydrogen sensing. In *Proc. IEEE SENSORS* 1-4. https://doi.org/10.1109/SENSORS43011.2019.8956523 (IEEE, 2019).
289. Galstyan, V., Comini, E., Baratto, C., Faglia, G. & Sberveglieri, G. Nanostructured ZnO chemical gas sensors. *Ceram. Int.* **41**, 14239–14244 (2015).
290. Girija, K. G., Somasundaram, K., Debnath, A. K., Topkar, A. & Vatsa, R. K. Enhanced H_2S sensing properties of gallium doped ZnO nanocrystalline films as investigated by DC conductivity and impedance spectroscopy. *Mater. Chem. Phys.* **214**, 297–305 (2018).
291. Wang, Y., Wu, X., Li, Y. & Zhou, Z. Mesostructured SnO_2 as sensing material for gas sensors. *Solid State Electron.* **48**, 627–632 (2004).
292. Kumar, R., Liu, X., Zhang, J. & Kumar, M. Room-temperature gas sensors under photoactivation: from metal oxides to 2D materials. *Nano-Micro Lett.* **12**, 164 (2020).
293. Tang, C. et al. Graphene-based chemiresistive hydrogen sensor for room temperature operation. *Sens. Actuators B Chem.* **424**, 136889 (2025).
294. Drewniak, S., Drewniak, Ł. & Pustelny, T. Mechanisms of NO_2 detection in hybrid structures containing reduced graphene oxide: a review. *Sensors* **22**, 5316 (2022).
295. Sur, U. K. Graphene: a rising star on the horizon of materials science. *Int. J. Electrochem.* **2012**, 1–12 (2012).
296. Dhall, S., Jaggi, N. & Nathawat, R. Functionalized multiwalled carbon nanotubes based hydrogen gas sensor. *Sens. Actuators A Phys.* **201**, 321–327 (2013).
297. Al-Diabat, A. M. et al. Improved hydrogen gas sensing performance of carbon nanotube synthesized using microwave oven. *IEEE Sens. J.* **23**, 1033–1041 (2023).
298. Tabares, G. et al. A route to detect H_2 in ambient conditions using a sensor based on reduced graphene oxide. *Sens. Actuators A Phys.* **304**, 111884 (2020).

299. Wang, C., Du, L., Xing, X., Feng, D. & Yang, D. Lightweight porous polyurethane foam integrated with graphene oxide for flexible and high-concentration hydrogen sensing. *ACS Sens.* **7**, 2420–2428 (2022).
300. Schipani, F., Puig, J., Morales, G. M. & Romeo, H. E. Noble-metal-free reduced graphene oxide platforms for room-temperature h2 sensing in high-humidity conditions. *ACS Appl. Electron. Mater.* **5**, 1824–1823 (2023).
301. Watts, P. C. P. et al. The importance of oxygen-containing defects on carbon nanotubes for the detection of polar and non-polar vapours through hydrogen bond formation. *Nanotechnology* **18**, 175701 (2007).
302. Dong, K.-Y. et al. Detection of a CO and NH_3 gas mixture using carboxylic acid-functionalized single-walled carbon nanotubes. *Nanoscale Res. Lett.* **8**, 12 (2013).
303. Gupta Chatterjee, S., Chatterjee, S., Ray, A. K. & Chakraborty, A. K. Graphene-metal oxide nanohybrids for toxic gas sensor: a review. *Sens. Actuators B: Chem.* **221**, 1170–1181 (2015).
304. Pei, S. & Cheng, H.-M. The reduction of graphene oxide. *Carbon* **50**, 3210–3228 (2012).
305. Shi, S. et al. Hydrogen gas diffusion behavior and detector installation optimization of lithium ion battery energy-storage cabin. *J. Energy Storage* **67**, 107510 (2023).
306. Zhou, Y. et al. Study on gas sensing of reduced graphene oxide/ZnO thin film at room temperature. *Sens. Actuators B Chem.* **240**, 870–880 (2017).
307. Rao, S., Upadhyay, J., Polychronopoulou, K., Umer, R. & Das, R. Reduced graphene oxide: Effect of reduction on electrical conductivity. *J. Compos. Sci.* **2**, 25 (2018).
308. Kim, J. H. et al. 3D printing of reduced graphene oxide nanowires. *Adv. Mater.* **27**, 157–161 (2015).
309. Wang, J., Kwak, Y., Lee, I., Maeng, S. & Kim, G.-H. Highly responsive hydrogen gas sensing by partially reduced graphite oxide thin films at room temperature. *Carbon* **50**, 4061–4067 (2012).
310. Zhou, Y. et al. Impact of further thermal reduction on few-layer reduced graphene oxide film and its n-p transition for gas sensing. *Sens. Actuators B Chem.* **235**, 241–250 (2016).
311. Kavinkumar, T., Sastikumar, D. & Manivannan, S. Effect of functional groups on dielectric, optical gas sensing properties of graphene oxide and reduced graphene oxide at room temperature. *RSC Adv.* **5**, 10816–10825 (2015).
312. Haidry, A. A. et al. Thermally reduced graphene oxide showing n- to p-type electrical response inversion with water adsorption. *Appl. Surf. Sci.* **531**, 147285 (2020).
313. Tu, N. D. K., Choi, J., Park, C. R. & Kim, H. Remarkable conversion between n- and p-type reduced graphene oxide on varying the thermal annealing temperature. *Chem. Mater.* **27**, 7362–7369 (2015).
314. Guo, L. et al. Two-beam-laser interference mediated reduction, patterning and nanostructuring of graphene oxide for the production of a flexible humidity sensing device. *Carbon* **50**, 1667–1673 (2012).
315. Fatima, Q. et al. The critical role of hydroxyl groups in water vapor sensing of graphene oxide. *Nanoscale Adv.* **1**, 1319–1330 (2019).
316. Some, S. et al. Highly sensitive and selective gas sensor using hydrophilic and hydrophobic graphenes. *Sci. Rep.* **3**, 1868 (2013).
317. Zhu, Z. et al. Facile design of flexible Pd nanoclusters sensitized reduced graphene oxide paper film towards hydrogen sensing. *Ceram. Int.* **49**, 12840–12845 (2023).
318. Hashtroudi, H. et al. Hydrogen gas sensing properties of microwave-assisted 2D Hybrid Pd/rGO: effect of temperature, humidity and UV illumination. *Int. J. Hydrog. Energy* **46**, 7653–7665 (2021).
319. Mohammadi, M. M. et al. Hydrogen sensing at room temperature using flame-synthesized palladium-decorated crumpled reduced graphene oxide nanocomposites. *ACS Sens.* **5**, 2344–2350 (2020).
320. Zhao, X. et al. Cyanogel-transformed porous palladium and iron framework intermixed with rGO for wearable hydrogen sensing. *Small* **21**, 2408117 (2025).
321. Kumar, A. et al. Reduced graphene oxide-wrapped palladium nanowires coated with a layer of zeolitic imidazolate Framework-8 for hydrogen sensing. *ACS Appl. Nano Mater.* **4**, 8081–8093 (2021).
322. Xing, X. et al. Three-dimensional porous carbon/nitrogen framework-decorated palladium nanoparticles for stable and wide-concentration-range hydrogen sensing. *ACS Appl. Mater. Interfaces* **14**, 17911–17919 (2022).
323. Xiao, M. et al. Batch Fabrication of ultrasensitive carbon nanotube hydrogen sensors with sub-ppm detection limit. *ACS Sens.* **3**, 749–756 (2018).
324. Girma, H. G. et al. Room-temperature hydrogen sensor with high sensitivity and selectivity using chemically immobilized monolayer single-walled carbon nanotubes. *Adv. Funct. Mater.* **33**, 2213381 (2023).
325. Alamri, M., Liu, B., Berrie, C. L., Walsh, M. & Wu, J. Z. Probing the role of CNTs in Pt nanoparticle/CNT/graphene nanohybrids H_2 sensors. *Nano Ex.* **3**, 035004 (2022).
326. Liu, B. et al. Atomic-layer deposition of the single-atom pt catalyst on vertical graphene for H_2 sensing. *ACS Appl. Nano Mater.* **7**, 22605–22616 (2024).
327. Kim, Y. et al. Au decoration of a graphene microchannel for self-activated chemoresistive flexible gas sensors with substantially enhanced response to hydrogen. *Nanoscale* **11**, 2966–2973 (2019).
328. Zhang, Z., Xue, Q., Du, Y., Ling, C. & Xing, W. Highly enhanced sensitivity of hydrogen sensors using novel palladium-decorated graphene nanoribbon film/SiO_2/Si structures. *J. Mater. Chem. A* **2**, 15931–15937 (2014).
329. Tang, S. et al. The functionalized single-walled carbon nanotubes gas sensor with Pd nanoparticles for hydrogen detection in the high-voltage transformers. *Front. Chem.* **8**, 174 (2020).
330. Rumiche, F., Wang, H. H. & Indacochea, J. E. Development of a fast-response/high-sensitivity double wall carbon nanotube nanostructured hydrogen sensor. *Sens. Actuators B Chem.* **163**, 97–106 (2012).
331. Sun, Y., Wang, H. H. & Xia, M. Single-walled carbon nanotubes modified with Pd nanoparticles: unique building blocks for high-performance, flexible hydrogen sensors. *J. Phys. Chem. C.* **112**, 1250–1259 (2008).
332. Ndaya, C. C., Javahiraly, N. & Brioude, A. Recent advances in palladium nanoparticles-based hydrogen sensors for leak detection. *Sensors* **19**, 4478 (2019).
333. Chung, M. G. et al. Flexible hydrogen sensors using graphene with palladium nanoparticle decoration. *Sens. Actuators B Chem.* **169**, 387–392 (2012).
334. Phan, D.-T. & Chung, G.-S. Reliability of hydrogen sensing based on bimetallic Ni-Pd/graphene composites. *Int. J. Hydrog. Energy* **39**, 20294–20304 (2014).
335. Phan, D.-T., Uddin, A. S. M. I. & Chung, G.-S. A large detectable-range, high-response and fast-response resistivity hydrogen sensor based on Pt/Pd core-shell hybrid with graphene. *Sens. Actuators B Chem.* **220**, 962–967 (2015).
336. Ma, L. et al. Pt catalyzed formation of a ni@pt/reduced graphene oxide nanocomposite: Preparation and electrochemical sensing application for glucose detection. *Anal. Methods* **10**, 3845–3850 (2018).
337. Nair, K. G., Ramakrishnan, V., Unnathpadi, R., Karuppanan, K. K. & Pullithadathil, B. Unraveling hydrogen adsorption kinetics of bimetallic au-pt nanoisland-functionalized carbon nanofibers for room-temperature gas sensor applications. *J. Phys. Chem. C.* **124**, 7144–7155 (2020).
338. Ahemad, M. J., Le, T. D., Kim, D.-S. & Yu, Y.-T. Bimetallic $AgAu_{alloy}$@ZnO core-shell nanoparticles for ultra-high detection of ethanol: Potential impact of alloy composition on sensing performance. *Sens. Actuators B Chem.* **359**, 131595 (2022).
339. Aleksanyan, M. S. et al. Flexible sensor based on multi-walled carbon nanotube-SnO_2 nanocomposite material for hydrogen detection. *Adv. Nat. Sci Nanosci. Nanotechnol.* **13**, 035003 (2022).
340. Ramanathan, R., Nagarajan, S., Jamdhar, S., Barshilia, H. C. & Mallik, R. C. Interface surface effect of SnO_2-GO thin-film heterostructure on H_2 gas sensor performance. *ACS Appl. Electron. Mater.* **6**, 7832–7846 (2024).
341. Kathiravan, D., Huang, B.-R. & Saravanan, A. Self-assembled hierarchical interfaces of ZnO nanotubes/graphene heterostructures for efficient room temperature hydrogen sensors. *ACS Appl. Mater. Interfaces* **9**, 12064–12072 (2017).
342. Majumdar, S., Nag, P. & Devi, P. S. Enhanced performance of CNT/SnO_2 thick film gas sensors towards hydrogen. *Mater. Chem. Phys.* **147**, 79–85 (2014).
343. Li, G. et al. Construction of rGO-SnO_2 heterojunction for enhanced hydrogen detection. *Appl. Surf. Sci.* **585**, 152623 (2022).
344. Punetha, D., Kar, M. & Pandey, S. K. A new type low-cost, flexible and wearable tertiary nanocomposite sensor for room temperature hydrogen gas sensing. *Sci. Rep.* **10**, 2151 (2020).
345. Rattan, S., Leal, A., Singh, S., Kumar, S. & Goswamy, J. K. Efficient detection of H_2 gas on ZnO-/SnO_2-graphene nanohybrids: experimental and DFT study. *J. Mater. Sci. Mater. Electron* **36**, 8 (2025).
346. Li, G. et al. Detection of ppm-level H_2 via rGO-SnO_2-ZnO nanocomposites: considering compositional matching in designing heterostructured gas-sensing materials. *Sens. Actuators B Chem.* **396**, 134560 (2023).
347. Drmosh, Q. A. et al. UV-activated gold decorated rGO/ZnO heterostructured nanocomposite sensor for efficient room temperature H_2 detection. *Sens. Actuators B Chem.* **290**, 666–675 (2019).

348. Duan, P. et al. Synthesis of self-assembled hollow spherical Au/SnO_2@rGO and its enhanced hydrogen sensing properties to ppb-level. *Sens. Actuators B Chem.* **375**, 132872 (2023).
349. Li, G. et al. Novel sensitizer AuxSn modify rGO-SnO_2 nanocomposites for enhancing detection of sub-ppm H_2. *Sens. Actuators B Chem.* **373**, 132656 (2022).
350. Hashtroudi, H., Yu, A., Juodkazis, S. & Shafiei, M. Ultra-sensitive photo-induced hydrogen gas sensor based on two-dimensional CeO_2-Pd-PDA/rGO heterojunction nanocomposite. *Nanomaterials* **12**, 1628 (2022).
351. Duan, P., Duan, Q., Peng, Q., Jin, K. & Sun, J. Design of ultrasensitive gas sensor based on self-assembled Pd-SnO_2/rGO porous ternary nanocomposites for ppb-level hydrogen. *Sens. Actuators B Chem.* **369**, 132280 (2022).
352. Zhang, X. et al. Ultralow detection limit and ultrafast response/recovery of the H_2 gas sensor based on Pd-doped rGO/ZnO-SnO_2 from hydrothermal synthesis. *Microsyst. Nanoeng.* **8**, 67 (2022).
353. Qiu, T. et al. High performance H_2 sensor based on rGO-wrapped SnO_2-Pd porous hollow spheres. *Ceram. Int.* **48**, 15056–15063 (2022).
354. Bai, S. et al. rGO decorated NiO-$BiVO_4$ heterojunction for detection of NO_2 at low temperature. *Sens. Actuators B Chem.* **329**, 128912 (2021).
355. Late, D. J. et al. Sensing behavior of atomically thin-layered MoS_2 transistors. *ACS Nano* **7**, 4879–4891 (2013).
356. Perrozzi, F. et al. Thermal stability of WS_2 flakes and gas sensing properties of WS_2/WO_3 composite to H_2, NH_3 and NO_2. *Sens. Actuators B Chem.* **243**, 812–822 (2017).
357. Li, T. et al. WS_2 monolayer decorated with single-atom Pt for outstanding H_2 adsorption and sensing: a DFT study. *Int. J. Hydrog. Energy* **141**, 1078–1087 (2025).
358. Wadhwa, R. et al. Pt nanoparticles on vertically aligned large-area MoS_2 flakes for selective H_2 sensing at room temperature. *ACS Appl. Nano Mater.* **6**, 2527–2537 (2023).
359. Jaiswal, J., Tiwari, P., Singh, P. & Chandra, R. Fabrication of highly responsive room temperature H_2 sensor based on vertically aligned edge-oriented MoS_2 nanostructured thin film functionalized by Pd nanoparticles. *Sens. Actuators B Chem.* **325**, 128800 (2020).
360. Jha, R. K., D'Costa, J. V., Sakhuja, N. & Bhat, N. $MoSe_2$ nanoflakes based chemiresistive sensors for ppb-level hydrogen sulfide gas detection. *Sens. Actuators B Chem.* **297**, 126687 (2019).
361. Meng, X., Bi, M., Xiao, Q. & Gao, W. Ultrasensitive gas sensor based on pd/SnS_2/SnO_2 nanocomposites for rapid detection of H_2. *Sens. Actuators B Chem.* **359**, 131612 (2022).
362. Verma, G. et al. Hierarchical MoS_2 nanostructured tubes on biodegradable and flexible chitosan-based platform for low temperature hydrogen detection. *IEEE Sens. J.* **25**, 11868–11875 (2025).
363. Zhang, Y., Zeng, W. & Li, Y. The hydrothermal synthesis of 3D hierarchical porous MoS_2 microspheres assembled by nanosheets with excellent gas sensing properties. *J. Alloy Compd.* **749**, 355–362 (2018).
364. Yan, W. et al. Conductometric gas sensing behavior of WS_2 aerogel. *FlatChem* **5**, 1–8 (2017).
365. Agrawal, A. V. et al. Enhanced adsorption sites in monolayer MoS_2 pyramid structures for highly sensitive and fast hydrogen sensor. *Int. J. Hydrog. Energy* **45**, 9268–9277 (2020).
366. Agrawal, A. V. et al. Fast detection and low power hydrogen sensor using edge-oriented vertically aligned 3-D network of MoS_2 flakes at room temperature. *Appl. Phys. Lett.* **111**, 093102 (2017).
367. Hao, L. et al. High hydrogen sensitivity of vertically standing layered MoS_2/Si heterojunctions. *J. Alloy. Compd.* **682**, 29–34 (2016).
368. Kumar, M., Bhati, V. S. & Kumar, M. Effect of Schottky barrier height on hydrogen gas sensitivity of metal/TiO_2 nanoplates. *Int. J. Hydrog. Energy* **42**, 22082–22089 (2017).
369. Yue, Q., Shao, Z., Chang, S. & Li, J. Adsorption of gas molecules on monolayer MoS_2 and effect of applied electric field. *Nanoscale Res. Lett.* **8**, 425 (2013).
370. Rezende, N. P. et al. Probing the electronic properties of monolayer MoS_2 via interaction with molecular hydrogen. *Adv. Elect. Mater.* **5**, 1800591 (2019).
371. Tabares, G., Magro, R., Vázquez, L., Fernandez, A. & Gordillo, N. $MoSe_2$xTe2-2x alloy for hydrogen gas detection. *Sens. Actuators A Phys.* **382**, 116126 (2025).
372. Long, H. et al. High surface area MoS_2/graphene hybrid aerogel for ultrasensitive NO_2 detection. *Adv. Funct. Mater.* **26**, 5158–5165 (2016).
373. Azcatl, A. et al. MoS_2 functionalization for ultra-thin atomic layer deposited dielectrics. *Appl. Phys. Lett.* **104**, 111601 (2014).
374. Qin, Z. et al. Enhanced room-temperature NH_3 gas sensing by 2D SnS_2 with sulfur vacancies synthesized by chemical exfoliation. *Sens. Actuators B Chem.* **262**, 771–779 (2018).
375. Guo, X. et al. Indium-doping-induced selenium vacancy engineering of layered tin diselenide for improving room-temperature sulfur dioxide gas sensing. *J. Mater. Chem. A* **10**, 22629–22637 (2022).
376. Tian, X. et al. Ultrasensitive room-temperature flexible ammonia gas sensor based on au-functionalized polypyrrole wrapped enriched edge sulfur vacancies MoS_2 nanosheets. *Sens. Actuators B: Chem.* **395**, 134449 (2023).
377. Han, S. W., Cha, G.-B., Park, Y. & Hong, S. C. Hydrogen physisorption based on the dissociative hydrogen chemisorption at the sulphur vacancy of MoS_2 surface. *Sci. Rep.* **7**, 7152 (2017).
378. Ye, G. et al. Defects engineered monolayer MoS_2 for improved hydrogen evolution reaction. *Nano Lett.* **16**, 1097–1103 (2016).
379. Li, H. et al. Correction: Corrigendum: activating and optimizing MoS_2 basal planes for hydrogen evolution through the formation of strained sulphur vacancies. *Nat. Mater.* **15**, 364–364 (2016).
380. Cheng, R. et al. Electroluminescence and photocurrent generation from atomically sharp WSe_2/MoS_2 heterojunction p-n diodes. *Nano Lett.* **14**, 5590–5597 (2014).
381. Dhara, S., Jawa, H., Ghosh, S., Varghese, A. & Lodha, S. All-electrical high sensitivity-low power dual mode gas sensing and recovery with a WSe_2/MoS_2 pn heterodiode. *ACS Appl. Mater. Interfaces* **13**, 30785–30796 (2021).
382. Kalita, P. & Mondal, B. Humidity tolerant enhanced hydrogen gas sensing using $MoSe_2$ -WSe_2 heterostructures: An experimental and computational insights. *Sens. Actuators B: Chem.* **424**, 136787 (2025).
383. Meng, Z., Stolz, R. M., Mendecki, L. & Mirica, K. A. Electrically-transduced chemical sensors based on two-dimensional nanomaterials. *Chem. Rev.* **119**, 478–598 (2019).
384. Wu, H. et al. Enhanced H_2 sensing performance of pd decorated MoS_2: experimental and DFT insights. *J. Alloy. Compd.* **1010**, 178139 (2025).
385. Cho, U. J. et al. A palladium-deposited molybdenum disulfide-based hydrogen sensor at room temperature. *Appl. Sci.* **13**, 10594 (2023).
386. Hao, L. et al. Highly Enhanced H_2 Sensing Performance of Few-Layer MoS_2/SiO_2/Si heterojunctions by surface decoration of Pd nanoparticles. *Nanoscale Res. Lett.* **12**, 567 (2017).
387. Mobtakeri, S., Habashyani, S. & Gür, E. Highly responsive Pd-decorated MoO_3 nanowall H_2 gas sensors obtained from in-situ-controlled thermal oxidation of sputtered MoS_2 films. *ACS Appl. Mater. Interfaces* **14**, 25741–25752 (2022).
388. Baek, D.-H. & Kim, J. MoS_2 gas sensor functionalized by Pd for the detection of hydrogen. *Sens. Actuators B: Chem.* **250**, 686–691 (2017).
389. Kuru, C. et al. MoS_2 Nanosheet-Pd nanoparticle composite for highly sensitive room temperature detection of hydrogen. *Adv. Sci.* **2**, 1500004 (2015).
390. Mai, H. D. et al. Pd nanocluster/monolayer MoS_2 heterojunctions for light-induced room-temperature hydrogen sensing. *ACS Appl. Mater. Interfaces* **13**, 14644–14652 (2021).
391. Suh, J. M. et al. Pd- and Au-decorated MoS_2 gas sensors for enhanced selectivity. *Electron. Mater. Lett.* **15**, 368–376 (2019).
392. Malik, S. B., Annanouch, F. E. & Llobet, E. Pd-nanoparticle-decorated multi-layered MoS_2 sheets for highly sensitive hydrogen sensing. *Chemosensors* **11**, 550 (2023).
393. Kabitakis, V. et al. A low-power CuSCN hydrogen sensor operating reversibly at room temperature. *Adv. Funct. Mater.* **32**, 2102635 (2022).
394. Lee, S. et al. Atomic layer deposited Pt nanoparticles on functionalized MoS_2 as highly sensitive H_2 sensor. *Appl. Surf. Sci.* **571**, 151256 (2022).
395. Gottam, S. R. et al. Highly sensitive hydrogen gas sensor based on a MoS_2-Pt nanoparticle composite. *Appl. Surf. Sci.* **506**, 144981 (2020).
396. Park, C. H. et al. Hydrogen sensors based on MoS_2 hollow architectures assembled by pickering emulsion. *ACS Nano* **14**, 9652–9661 (2020).
397. Gottam, S. R., Wang, L.-W., Wu, T.-Y., Liu, Y.-H. & Chu, S.-Y. WS_2-Pt nanostructure-based composite for hydrogen gas sensing with ultra-fast response and recovery rates. *ECS J. Solid State Sci. Technol.* **12**, 057001 (2023).
398. Hou, W. et al. Hydrogen sensors of ce-doped MoS_2 with anti-humidity for early warning thermal runaway in lithium-ion batteries. *Sens. Actuators B Chem.* **425**, 136988 (2025).
399. Mondal, B. et al. A resistance-driven H_2 gas sensor: high-entropy alloy nanoparticles decorated 2D MoS_2. *Nanoscale* **15**, 17097–17104 (2023).
400. Urs, K. M. B. et al. Multi-component (Ag-Au-Cu-Pd-Pt) alloy nanoparticle-decorated p-type 2D-molybdenum disulfide (MoS_2) for enhanced hydrogen sensing. *Nanoscale* **12**, 11830–11841 (2020).

401. Yang, S. et al. In situ synthesis of MoS_2-decorated Zn-doped MoO_3 for outstanding hydrogen sensing at room temperature. *Sens. Actuators B Chem.* **367**, 132026 (2022).
402. Bai, H. et al. Facile synthesis of mesoporous CdS/PbS/SnO_2 composites for high-selectivity H_2 gas sensor. *Sens. Actuators B: Chem.* **340**, 129924 (2021).
403. Hao, J. et al. Hierarchical SnS_2/SnO_2 nanoheterojunctions with increased active-sites and charge transfer for ultrasensitive NO_2 detection. *Nanoscale* **10**, 7210–7217 (2018).
404. Gao, J. et al. Aging of transition metal dichalcogenide monolayers. *ACS Nano* **10**, 2628–2635 (2016).
405. Xie, H. et al. Temperature and thickness dependence of the sensitivity of nitrogen dioxide graphene gas sensors modified by atomic layer deposited zinc oxide films. *RSC Adv.* **5**, 28030–28037 (2015).
406. Du, X. & George, S. M. Thickness dependence of sensor response for CO gas sensing by tin oxide films grown using atomic layer deposition. *Sens. Actuators B Chem.* **135**, 152–160 (2008).
407. Paolucci, V., Emamjomeh, S. M., Nardone, M., Ottaviano, L. & Cantalini, C. Two-step exfoliation of WS_2 for NO_2, H_2 and humidity sensing applications. *Nanomaterials* **9**, 1363 (2019).
408. Paolucci, V., De Santis, J., Lozzi, L., Giorgi, G. & Cantalini, C. Layered amorphous a-SnO_2 gas sensors by controlled oxidation of 2D-$SnSe_2$. *Sens. Actuators B: Chem.* **350**, 130890 (2022).
409. Paolucci, V., De Santis, J., Ricci, V., Lozzi, L. & Cantalini, C. 2D amorphous/crystalline a-In_2O_3/In_2Se_3 nanosheet heterostructures with improved capability for H_2 and NO_2 Sensing. *ACS Appl. Nano Mater.* **6**, 6011–6023 (2023).
410. Lipatov, A. & Sinitskii, A. Electronic and mechanical properties of MXenes derived from single-flake measurements. In *2D Metal Carbides and Nitrides (MXenes)* (eds Anasori, B. & Gogotsi, Y.) 301–325 (Springer International Publishing, 2019). https://doi.org/10.1007/978-3-030-19026-2_16.
411. Mazumder, J. T. & Jha, R. K. Theoretical insights into gas sensing properties of MXene. *Sens. Actuator Rep.* **6**, 100174 (2023).
412. Guo, Z. et al. High electrical conductivity 2D MXene serves as additive of perovskite for efficient solar cells. *Small* **14**, 1802738 (2018).
413. Naguib, M., Mochalin, V. N., Barsoum, M. W. & Gogotsi, Y. 25th anniversary article: MXenes: a new family of two-dimensional materials. *Adv. Mater.* **26**, 992–1005 (2014).
414. Anasori, B., Lukatskaya, M. R. & Gogotsi, Y. 2D metal carbides and nitrides (MXenes) for energy storage. *Nat. Rev. Mater.* **2**, 16098 (2017).
415. Shen, J. et al. 2D MXene nanofilms with tunable gas transport channels. *Adv. Funct. Mater.* **28**, 1801511 (2018).
416. Lee, E., VahidMohammadi, A., Yoon, Y. S., Beidaghi, M. & Kim, D.-J. Two-dimensional vanadium carbide MXene for gas sensors with ultrahigh sensitivity toward nonpolar gases. *ACS Sens* **4**, 1603–1611 (2019).
417. Phuong Doan, T. H., Hong, W. G. & Noh, J.-S. Palladium nanoparticle-decorated multi-layer $Ti_3C_2T_x$ dual-functioning as a highly sensitive hydrogen gas sensor and hydrogen storage. *RSC Adv.* **11**, 7492–7501 (2021).
418. Xu, X. et al. Vanadium-doped tin oxide porous nanofibers: enhanced responsivity for hydrogen detection. *Talanta* **167**, 638–644 (2017).
419. Simo, A., Mwakikunga, B. & Maaza, M. One-dimensional vanadium dioxide nanostructures for room temperature hydrogen sensors. *S T* **189**, 143–149 (2015).
420. Zhu, Z. et al. Flexible and lightweight $Ti_3C_2T_x$ MXene@Pd colloidal nanoclusters paper film as novel H_2 sensor. *J. Hazard. Mater.* **399**, 123054 (2020).
421. Nam, M. S., Kim, J.-Y., Mirzaei, A., Kim, H. W. & Kim, S. S. Pd-functionalized $Ti_3C_2T_x$ MXenes for realization of flexible, selective, self-heated H_2 sensing. *Sens. Actuators B: Chem.* **404**, 135189 (2024).
422. Yang, Z. et al. A comparative study of H_2 sensing performance of stoichiometric polymorphs of titanium carbide MXenes loaded with Pd nanodots. *Phys. Chem. Chem. Phys.* **25**, 16438–16445 (2023).
423. Huang, X. et al. Au-Pd separation enhances bimetallic catalysis of alcohol oxidation. *Nature* **603**, 271–275 (2022).
424. Li, X. et al. Solvent-free benzyl alcohol oxidation using spatially separated carbon-supported Au and Pd nanoparticles. *ACS Catal.* **14**, 16551–16561 (2024).
425. Wang, L. et al. Pt=Pd separation modified $Ti_3C_2T_x$ MXene for hydrogen detection at room temperature. *Int. J. Hydrog. Energy* **48**, 30205–30217 (2023).
426. She, P., Qin, J., Rao, H., Guan, B. & Yu, J. Spatially separated bimetallic cocatalysts on hollow-structured TiO_2 for photocatalytic hydrogen generation. *Mater. Chem. Front.* **4**, 1671–1678 (2020).
427. Chen, Q., Zhang, Y., Tang, M., Wang, Z. & Zhang, D. A fast response hydrogen sensor based on the heterojunction of MXene and SnO_2 nanosheets for lithium-ion battery failure detection. *Sens. Actuators B Chem.* **405**, 135229 (2024).
428. Kuang, D. et al. Facile hydrothermal synthesis of $Ti_3C_2T_x$-TiO_2 nanocomposites for gaseous volatile organic compounds detection at room temperature. *J. Hazard. Mater.* **416**, 126171 (2021).
429. Zhou, M. et al. Fabrication of $Ti_3C_2T_x$/In_2O_3 nanocomposites for enhanced ammonia sensing at room temperature. *Ceram. Int.* **48**, 6600–6607 (2022).
430. Yu, S., Li, P., Ding, H., Liang, C. & Wang, X. 2D MXenes-based gas sensors: progress, applications, and challenges. *Small Methods* n/a, 2402179.
431. Zhang, A. et al. Dual-gas sensing via SnO_2-TiO_2 heterojunction on MXene: Machine learning-enhanced selectivity and sensitivity for hydrogen and ammonia detection. *Sens. Actuators B Chem.* **429**, 137340 (2025).
432. Paul, S. et al. Opto-chemical sensor system for the detection of H_2 and hydrocarbons based on InGaN/GaN nanowires. *Sens. Actuators B Chem.* **173**, 120–126 (2012).
433. Schalwig, J., Müller, G., Ambacher, O. & Stutzmann, M. Group-III-nitride based gas sensing devices. *Phys. Status Solidi A.* **185**, 39–45 (2001).
434. Neuberger, R., Müller, G., Ambacher, O. & Stutzmann, M. High-electron-mobility AlGaN/GaN transistors (HEMTs) for fluid monitoring applications. *Phys. Status Solidi A* **185**, 85–89 (2001).
435. Fujita, S. Wide-bandgap semiconductor materials: for their full bloom. *Jpn. J. Appl. Phys.* **54**, 030101 (2015).
436. Shafa, M. et al. Twofold porosity and surface functionalization effect on Pt-Porous GaN for high-performance H_2-gas sensors at room temperature. *ACS Omega* **4**, 1678–1684 (2019).
437. Zhong, A. et al. Ultrafast H_2 gas nanosensor for ppb-level H_2 gas detection based on GaN honeycomb nanonetwork. *Sens. Actuators B Chem.* **329**, 129079 (2021).
438. Abdullah, Q. N., Yam, F. K., Hassan, Z. & Bououdina, M. Pt-decorated GaN nanowires with significant improvement in H_2 gas-sensing performance at room temperature. *J. Colloid Interf. Sci.* **460**, 135–145 (2015).
439. Yu, H. Capacitive sensor based on GaN honeycomb nanonetwork for ultrafast and low temperature hydrogen gas detection. *Sens. Actuators* **346**, 130488 (2021).
440. Niu, J.-S. et al. Hydrogen detecting characteristics and an improved algorithm for data transmission of a palladium nanoparticle/amorphous InGaZnO thin film based sensor. *Sens. Actuators B Chem.* **377**, 133091 (2023).
441. Li, Z. et al. Room temperature hydrogen gas sensor based on Pd-decorated bridging GaN nanowires. *Sens. Actuators B Chem.* **417**, 136172 (2024).
442. Kim, H., Kim, W., Cho, S., Park, J. & Jung, G. Y. Molecular sieve based on a PMMA/ZIF-8 bilayer for a CO-tolerable H_2 sensor with superior sensing performance. *ACS Appl. Mater. Interfaces* **12**, 28616–28623 (2020).
443. Darmadi, I., Nugroho, F. A. A., Kadkhodazadeh, S., Wagner, J. B. & Langhammer, C. Rationally designed PdAuCu ternary alloy nanoparticles for intrinsically deactivation-resistant ultrafast plasmonic hydrogen sensing. *ACS Sens.* **4**, 1424–1432 (2019).
444. Kumar, B. & Prasad, R. M. Polymer-derived microporous SiOC ceramic coated gallium nitride sensor for selective H_2/CO detection. *Sens. Actuators B Chem.* **379**, 133226 (2023).
445. Koo, W.-T. et al. Accelerating palladium nanowire H_2 sensors using engineered nanofiltration. *ACS Nano* **11**, 9276–9285 (2017).
446. Huang, W.-C. et al. Highly stable and selective H_2 gas sensors based on light-activated a-IGZO thin films with ZIF-8 selective membranes. *Sens. Actuators B Chem.* **417**, 136175 (2024).
447. Van Den Broek, J., Weber, I. C., Güntner, A. T. & Pratsinis, S. E. Highly selective gas sensing enabled by filters. *Mater. Horiz.* **8**, 661–684 (2021).
448. Wu, X., Xiong, S., Mao, Z., Hu, S. & Long, X. A designed ZnO@ZIF-8 core-shell nanorod film as a gas sensor with excellent selectivity for H_2 over CO. *Chem. Eur. J.* **23**, 7969–7975 (2017).
449. Sun, A. et al. Pd gated AlGaN/GaN high electron mobility transistor for ppb level hydrogen gas detection. *Int. J. Hydrog. Energy* **47**, 17494–17503 (2022).
450. Zhong, A. et al. Tailoring the H_2 gas detection range of the AlGaN/GaN high electron mobility transistor by tuning the Pt gate thickness. *Int. J. Hydrog. Energy* **47**, 2050–2058 (2022).
451. Kim, S. E., Jang, S. Y., Park, K.-H. & Lee, S. W. A route for an improved hydrogen sensing window using ZnO decorated Pt/AlGaN/GaN HEMT sensors. *Ceram. Int.* **48**, 23590–23597 (2022).
452. Yamazoe, N. & Shimanoe, K. Theory of power laws for semiconductor gas sensors. *Sens. Actuators B: Chem.* **128**, 566–573 (2008).

453. Hua, Z., Li, Y., Zeng, Y. & Wu, Y. A theoretical investigation of the power-law response of metal oxide semiconductor gas sensors I: Schottky barrier control. *Sens. Actuators B Chem.* **255**, 1911–1919 (2018).
454. Tao, N. Challenges and promises of metal oxide nanosensors. *ACS Sens.* **4**, 780–780 (2019).
455. Potyrailo, R. A. et al. Extraordinary performance of semiconducting metal oxide gas sensors using dielectric excitation. *Nat. Electron.* **3**, 280–289 (2020).
456. Prakasha, B. S. et al. Impedance-assisted multivariate analysis technique for enhanced gas sensing with 2D dichalcogenides. *ACS Sens.* **10**, 2712–2720 (2025).
457. Zhang, H. et al. A chemiresistive-potentiometric multivariate sensor for discriminative gas detection. *Nat. Commun.* **14**, 3495 (2023).
458. Lee, B. K. et al. A principal odor map unifies diverse tasks in olfactory perception. *Science* **381**, 999–1006 (2023).
459. Buttner, W. J., Post, M. B., Burgess, R. & Rivkin, C. An overview of hydrogen safety sensors and requirements. *Int. J. Hydrog. Energy* **36**, 2462–2470 (2011).
460. Ahmad Fauzi, A. S. et al. Carbon-based potentiometric hydrogen sensor using a proton-conducting graphene oxide membrane coupled with a WO_3 sensing electrode. *Sens. Actuators B Chem.* **323**, 128678 (2020).
461. Rîmbu, G. A. et al. Electrochemical sensor for hydrogen leakage detection at room temperature. *Sensors* **25**, 264 (2025).
462. Zhi, Z. et al. Amperometric hydrogen gas sensor based on Pt/C/nafion electrode and ionic electrolyte. *Sens. Actuators B Chem.* **367**, 132137 (2022).
463. Berndt, D. et al. MEMS-based thermal conductivity sensor for hydrogen gas detection in automotive applications. *Sens. Actuators A Phys.* **305**, 111670 (2020).
464. Akasaka, S., Terumoto, K. & Kanno, I. Temperature dependence of accuracy of thermal conductivity hydrogen sensor. In *Proc. IEEE SENSORS* 1-4. https://doi.org/10.1109/SENSORS60989.2024.10784458 (IEEE, 2024).
465. Wang, J. et al. Thermal conductivity gas sensor with enhanced flow-rate independence. *Sensors* **22**, 1308 (2022).
466. Ivanov, I., Baranov, A., Mironov, S. & Akbari, S. Selective low-temperature hydrogen catalytic sensor. *IEEE Sens. Lett.* **6**, 1–4 (2022).
467. Kumar, A. et al. Palladium nanosheet-based dual gas sensors for sensitive room-temperature hydrogen and carbon monoxide detection. *ACS Sens* **7**, 225–234 (2022).
468. Cho, M., Zhu, J., Kim, H., Kang, K. & Park, I. Half-pipe palladium nanotube-based hydrogen sensor using a suspended nanofiber scaffold. *ACS Appl. Mater. Interfaces* **11**, 13343–13349 (2019).
469. Cao, F. et al. An ultrasensitive and ultraselective hydrogen sensor based on defect-dominated electron scattering in Pt nanowire arrays. *Adv. Mater. Interfaces* **6**, 1801304 (2019).
470. Lee, J.-S. et al. Stress-engineered palladium nanowires for wide range (0.1%-3.9%) of H_2 detection with high durability. *Nanoscale* **11**, 16317–16326 (2019).
471. Zhao, Z.-J. et al. Wafer-scale, highly uniform, and well-arrayed suspended nanostructures for enhancing the performance of electronic devices. *Nanoscale* **14**, 1136–1143 (2022).
472. Kim, D.-H. et al. High-resolution, fast, and shape-conformable hydrogen sensor platform: polymer nanofiber yarn coupled with nanograined pd@pt. *ACS Nano* **13**, 6071–6082 (2019).
473. Yang, H. et al. Fabrication of wide-detection-range H_2 sensors with controllable saturation behavior using Au@Pd nanoparticle arrays. *Chem. Commun.* **56**, 12636–12639 (2020).
474. Zhang, L., Xie, G., Liu, F. & Ji, H. High hydrogen selectivity Pd-Ni alloy film hydrogen sensor with hybrid organosilica membranes. *J. Alloy. Compd.* **941**, 168898 (2023).
475. Anna Anasthasiya, A. N., Prabhu, E., Jayaraman, V. & Gnanasekar, K. I. Wide range H_2 sensors for process streams, based on multilayered Pd thin films dispersed with ag nanoparticles and chromium as buffer layer. *Int. J. Hydrog. Energy* **45**, 22195–22203 (2020).
476. Liu, Q., Yao, J., Wang, Y., Sun, Y. & Ding, G. Temperature dependent response/recovery characteristics of Pd/Ni thin film based hydrogen sensor. *Sens. Actuators B Chem.* **290**, 544–550 (2019).
477. Du, L. et al. Palladium/cobalt nanowires with improved hydrogen sensing stability at ultra-low temperatures. *Nanoscale* **11**, 21074–21080 (2019).
478. Hung, P.-S. et al. A vertically integrated ZnO-based hydrogen sensor with hierarchical bi-layered inverse opals. *Sens. Actuators B Chem.* **325**, 128779 (2020).
479. Kohlmann, N. et al. Fabrication of ZnO nanobrushes by H_2-C_2 H_2 plasma etching for H_2 sensing applications. *ACS Appl. Mater. Interfaces* **13**, 61758–61769 (2021).
480. Kumar, M., Bhatt, V., Abhyankar, A. C., Yun, J.-H. & Jeong, H.-J. Multifunctional dumbbell-shaped ZnO-based temperature-dependent UV photodetection and selective H_2 gas detection. *Int. J. Hydrog. Energy* **45**, 15011–15025 (2020).
481. Wilken, M. et al. CVD-grown tungsten oxide for low temperature hydrogen sensing: Tuning surface characteristics via materials processing for sensing applications. *Small* **19**, 2204636 (2023).
482. Qin, C., Wei, Z., Zhao, X., Cao, J. & Wang, Y. High-temperature hydrogen sensor based on MOFs-derived Mn-doped In_2O_3 hollow nanotubes. *Int. J. Hydrog. Energy* **78**, 1024–1033 (2024).
483. Hu, Q. et al. Direct confirmation of confinement effects by NiO confined in helical SnO_2 nanocoils and its application in sensors. *J. Mater. Chem. A* **10**, 2786–2794 (2022).
484. Li, H. et al. Mesoporous WO_3-TiO_2 heterojunction for a hydrogen gas sensor. *Sens. Actuators B Chem.* **341**, 130035 (2021).
485. Jeong, J. et al. Highly stable and reversible hydrogen sensors using Pd-coated SnO_2 nanorods and an electrode-substrate interface as a parallel conduction channel. *Sens. Actuators B: Chem.* **394**, 134350 (2023).
486. Uddin, M. M., Rahaman, M. H. & Kim, H. C. Highly stable hydrogen sensing properties of pt-ZnO nanoparticle layers deposited on an alumina substrate for high-temperature industrial applications. *Sens. Actuators B Chem.* **368**, 132088 (2022).
487. Wang, X., Meng, X. & Gao, W. Ultrahigh-response sensor based on hierarchical Pd-WO_3 nanoflowers for rapid hydrogen detection. *Sens. Actuators B Chem.* **387**, 133790 (2023).
488. Le, H.-J., Van Dao, D. & Yu, Y.-T. Superfast and efficient hydrogen gas sensor using $PdAu_{alloy}$ @ZnO core-shell nanoparticles. *J. Mater. Chem. A* **8**, 12968–12974 (2020).
489. Zhang, Z. et al. Polymerization-induced aggregation approach toward uniform pd nanoparticle-decorated mesoporous SiO_2/WO_3 microspheres for hydrogen sensing. *ACS Appl. Mater. Interfaces* **15**, 15721–15731 (2023).
490. Dhall, S. & Mehta, B. R. Room temperature hydrogen gas sensor using candle carbon soot. *Int. J. Hydrog. Energy* **45**, 14997–15002 (2020).
491. Lee, B. et al. Highly responsive hydrogen sensor based on Pd nanoparticle-decorated transfer-free 3D graphene. *Sens. Actuators B: Chem.* **401**, 134913 (2024).
492. Yadav, S., Nair, A., Urs Mb, K. & Kamble, V. B. Protonic titanate nanotube-reduced graphene oxide composites for hydrogen sensing. *ACS Appl. Nano Mater.* **3**, 10082–10093 (2020).
493. Kathiravan, D., Huang, B.-R., Saravanan, A. & Tzeng, Y. Role of nanodiamond grains in the exfoliation of WS_2 nanosheets and their enhanced hydrogen-sensing properties. *ACS Appl. Mater. Interfaces* **13**, 48260–48269 (2021).
494. Kathiravan, D., Huang, B.-R., Saravanan, A., Prasannan, A. & Hong, P.-D. Highly enhanced hydrogen sensing properties of sericin-induced exfoliated MoS_2 nanosheets at room temperature. *Sens. Actuators B Chem.* **279**, 138–147 (2019).
495. Abun, A., Huang, B.-R., Saravanan, A., Kathiravan, D. & Hong, P.-D. Exfoliated $MoSe_2$ nanosheets doped on the surface of ZnO nanorods for hydrogen sensing applications. *ACS Appl. Nano Mater.* **3**, 12139–12147 (2020).
496. Liu, K., Liu, Y., Lin, D., Pei, A. & Cui, Y. Materials for lithium-ion battery safety. *Sci. Adv.* **4**, eaas9820S (2018).